1-1-2013

Volcanic and Tectonic Processes Along Anomalous Mid-Ocean Ridges

Julia Kathryn Howell
University of South Carolina

VOLCANIC AND TECTONIC PROCESSES ALONG ANOMALOUS MID-OCEAN RIDGES

by

Julia Kathryn Howell

Bachelor of Science
North Carolina State University, 2008

Submitted in Partial Fulfillment of the Requirements

For the Degree of Doctor of Philosophy in

Geological Sciences

College of Arts and Sciences

University of South Carolina

2013

Accepted by:

Scott M. White, Major Professor

Michael Bizimis, Committee Member

David Barbeau, Committee Member

DelWayne Bohnenstiehl, Committee Member

Lacy Ford, Vice Provost and Dean of Graduate Studies

DEDICATION

To my family, who always believed I could do anything; to my mother, because I am just like her; and to my father, who made me wait and see.

ACKNOWLEDGEMENTS

This dissertation would not have been possible without guidance and advice from Dr. Scott M. White, Dr. DelWayne R. Bohnenstiehl, Dr. Michael Bizimis, Dr. Mark Behn, and Dr. David Barbeau.

ABSTRACT

The morphological and structural characteristics of the global spreading ridge system are systematically related to spreading rate and magma supply (e.g. Macdonald, 1982). Because intermediate spreading-rate ridges (ISRs) spreading between 60 and 80 mm/yr have characteristics of both fast and slow spreading ridges, they are ideal environments to study the differences controlling upper crustal accretion. We examine the distribution of seamounts along spreading ridges to understand the relationship between seamount volcanism and axial morphology along four ISRs: the Juan de Fuca Ridge (JdFR), the Galápagos Spreading Centers (GSC), the Southeast Indian Ridge (SEIR), and the Eastern Lau Spreading Centers (ELSC). Before determining the distribution of volcanoes on the seafloor, the Modified Basal Outlining Algorithm (MBOA) developed by Bohnenstiehl et al. (2012) is assessed for its accuracy in picking volcanic edifices relative to a traditional field-based geologic mapping approach at the Springerville Volcanic Field, Arizona. There, MBOA is able to closely match the geologic map, under-predicting height and area by 4% and over-predicting volume by 13%. Applying MBOA to determine the seamount abundance, volume and spatial distribution along the ISRs indicate that (1) seamounts do not form at the ends of segments along the JdFR, GSC or ELSC, but do form at the ends of segments along the SEIR, (2) a systematic relationship exists between axial morphology and ridge migration in the hotspot reference frame along the SEIR, and (3) segments offset in the direction of ridge migration have axial highs along the leading segment end and axial valleys along

the trailing segment end. Given that ridge migration oblique to spreading direction causes enhanced melting beneath the leading segment end (Katz et al., 2004), we attempt to understand the formation of faults when the near-field spreading direction is oblique to the far-field stretching direction (i.e., the direction plates are pulled apart). Three dimensional finite-element modeling of an idealized MOR indicates that faults slip in a direction halfway between the spreading and stretching directions outside of the axial graben. Inside the axial graben, faults slip in a direction approaching the stretching direction. This indicates simply pulling the lithosphere causes the orientation of volcanic and tectonic structures to change without changing the underlying structure of the upwelling asthenosphere.

TABLE OF CONTENTS

LIST OF TABLES

LIST OF FIGURES

CHAPTER 1: INTRODUCTION

The mid-ocean ridge (MOR) system is the largest single volcanic feature on Earth, encircling the globe like the seams of a baseball (Figure 1.1; Macdonald et al., 1991). As the MOR is pulled apart by plate tectonics, new oceanic crust is created through a combination of magmatic, tectonic and hydrothermal processes (Smith and Cann, 1993). The surface expression of this complex system is distinctive seafloor topography, the characteristics of which vary systematically with spreading rate and magma supply (e.g., Macdonald, 1982; Small and Sandwell, 1989; Phipps Morgan and Chen, 1993; Smith and Cann, 1993).

At spreading rates of 90-170 mm/yr, such as those along the East Pacific Rise (EPR, Figure 1.2), rift topography is distinguished by an axial high 1-2 km wide (Figure 1.3). Fault scarps with 10 m of throw, low relief lava flows and seamounts < 25 m tall dominate the constructional volcanism (Smith and Cann, 1993; White et al., 1998, 2000, 2002a, 2002b). The ridge crest is offset at many levels; regionally by first-order transform offsets, and locally by second-order overlapping spreading centers, third-order offsets in volcanic ridges, and fourth order deviations in axial linearity (Macdonald et al., 1991) (Figure 1.4). Offsets in segmentation along the EPR are expected to coincide with discontinuities in the axial magma lens (Figure 1.4); whether the magma lens or tectonic stresses control second-order segmentation is still debated (e.g., Tomey et al., 2007). What is clear, however, is that low effusion rate eruptions occur at the ends of second-

order segments (White et al., 2002b; Bohnenstiehl et al., 2008) where the magma lens disappears.

In contrast, ridges spreading between 5 and 50 mm/yr such as the Mid-Atlantic Ridge (MAR, Figure 1.5) are dominated by an axial rift valley 30-45 km wide and 1-2 km deep (Figure 1.6). The median valley is composed of an inner valley floor 5-12 km wide, bordered by valley walls in which numerous normal faults, some of which are hundreds of meters tall, displace the crust upwards to form crustal mountains (Smith and Cann, 1993). Eruptions on the valley floor commonly build prominent axial volcanic ridges composed of coalesced individual small volcanoes (Smith and Cann, 1993). Segmentation of a slow spreading axis is regionally offset by transform boundaries and locally by non-transform discontinuities of volcanic activity. Second-order segments along slow spreading ridges have hourglass shapes, with a narrower and elevated median valley near the center of the segment. Because a continuous magma lens has not been imaged beneath the MAR, magma is expected to rise in small bodies near the centers of second-order segments, creating the hourglass shape (Figure 1.7).

The morphology and style of volcanism at fast and slow spreading ridges represent two distinct modes of ridge axis structure; understanding how and under what circumstances one mode passes into the other is critical in understanding ridge axis processes (e.g., Baran et al., 2005). Many studies have attempted to explain and pinpoint the transition from slow to fast spreading axial morphology (e.g. Chen and Phipps Morgan, 1987; Small and Sandwell, 1989). The Chen and Phipps Morgan (1987) model describes a relatively cool and brittle crust behaving plastically beneath slow spreading ridges. The crust is strongly coupled to the mantle, so a rift valley develops. As

spreading rate is increased, a weak ductile zone develops just above the Moho. If the width of the ductile zone exceeds the width of the plastically deforming zone, the crust is decoupled from the mantle and the ridge axis can rebound to local isostatic equilibrium resulting in a central high (Chen and Phipps Morgan, 1987; Small and Sandwell, 1989). The Chen and Phipps Morgan (1987) model predicts the transition from axial valley to axial high will occur at ~76 mm/yr.

From vertical deflection (gravity) profiles along multiple MORs, Small and Sandwell (1989) observe a distinct change in axial topography and compensation mechanism at 65 mm/yr. Their observations of gravity signatures indicate that below 65 mm/yr the vertical deflection profile is variable and has high amplitude. Above 65 mm/yr, the vertical deflection profiles are uniform and have low amplitudes. They attribute this change in gravity signature to isostatic compensation; the gravity signature associated with slow spreading ridges results from a complicated interaction between hydrothermal cooling, brittle fracturing and ductile necking of a highly non-uniform material. Magma delivery to slow spreading ridges is believed to be episodic and non-uniform, potentially contributing to the axial topography (e.g. Macdonald, 1982). According to Small and Sandwell (1989), the uniform and low amplitude gravity signature from fast spreading ridges indicates that topography is well compensated due to uniform spreading or a more continuous supply of magma to the ridge.

More recent models (Behn and Ito, 2008; Ito and Behn, 2008) suggest axial morphology is a function of the "rise-sink ratio" of the crust, where the rise is defined as the time fraction in the magmatic period (versus the tectonic period), and the sink is defined as the rate at which the ridge axis rises during magmatic phases and sinks during

tectonic phases. In other words, ridges with extended magmatic phases like the EPR have axial high topography, ridges with equal magmatic and tectonic phases have "flat" topography like the Southeast Indian Ridge, and ridges with extended tectonic phases like the MAR have axial valleys. The length of each phase is a function of fault spacing, which is controlled by the net force required to keep an active fault slipping as it moves off-axis and the force needed to create a new fault by breaking the lithosphere near the axis (Ito and Behn, 2008).

Intermediate spreading-rate ridges (50-90 mm/yr) encompass the spreading-rate window where one mode of crustal accretion passes into the other. Intermediate spreading-rate ridges (ISRs) have nearly constant spreading rates but variable axial morphology, making them ideal study areas to understand separate modes of crustal accretion. ISRs are unique in their spreading rates and axial morphology, but also because nearly all ISRs are influenced by a near-axis hotspot. Anomalous magma supplied to the MOR is accommodated differently at each ISR, but typically through elevated crustal thicknesses (Detrick et al., 2002; Sinton et al., 2003), axial high morphology (Sinton et al., 2003), steady-state crustal magma lens (Phipps Morgan and Chen, 1993; Detrick et al., 2002; Carbotte et al., 2008), and a change in the style of volcanism from small, point source volcanoes to large lava shields (White et al., 2008). Using the characteristics indicative of fast or slow spreading ridges, researchers have attempted to isolate the role of magma supply on crustal generation. They find seamount abundance, crustal thickness, depth to melt lens, continuity of melt lens and style of volcanism are inherently related to magma supply at a constant spreading rate.

Although ISRs encompass the window in which one style of crustal accretion passes into the other, prior to this work there has been no systematic study examining global relationships between volcanism and axial morphology at ISRs. Here, we examine the distribution of seamounts forming at four ISRs and their correlation with axial morphology, used as a proxy for magma supply: the Juan de Fuca Ridge, Galápagos Spreading Center, Southeast Indian Ridge and the Eastern Lau Spreading Centers (Figure 1.1). These ISRs exhibit variation in axial morphology and magma supply from nearby magmatic hotspots, subduction zones or melt anomalies, allowing us to examine the influence of locally increased magma budget independent of spreading rate. We test the relationship between volcano distribution and magma supply based on the expectation that volcano abundance and volume will be greater near the ends of axial high segments (White et al., 1998, 2002a, 2002b, 2008; Bohnenstiehl et al., 2008) and sporadically distributed along axial valley segments (Smith and Cann, 1990, 1992, 1993; Smith et al., 1995).

Existing methods of identifying volcanoes from gridded elevation datasets involved manually digitizing the volcano outline or using an automated closed-contouring method (e.g., Behn et al., 2004; Bohnenstiehl et al., 2008). Closed-contouring methods have many advantages over manually digitizing volcano outlines; chiefly, they operate directly on the digital elevation model and do not rely on derived products such as slope, curvature or flood maps (Bohnenstiehl et al., 2012). Closed-contouring methods also are scale independent, meaning they can be applied without modification to analyze variable resolution datasets in both submarine and subaerial environments (Bohnenstiehl et al., 2012). The most important advantage of the closed-contouring method is that it is

objective and efficient at identifying and isolating multiple volcanoes from a gridded elevation dataset. The principal limitation of the closed-contouring method is that the base of the selected volcano is constrained to lie at a constant elevation, excluding the volume or area of volcanoes with irregular elevation bases (Bohnenstiehl et al., 2012; Howell et al., 2012). To mitigate the limitations of closed-contour algorithms, Bohnenstiehl et al. (2012) developed a procedure to migrate the base of a closed-contour down slope until a set of geometric conditions are met, called the Modified Basal Outlining Algorithm (MBOA). The result from the MBOA is a set of volcanic edifices defined by variable-elevation basal polygons. In Chapter 2 of this study the results from the MBOA are compared to the closed-contouring method and a digital geologic map of a continental cinder cone field. We find the MBOA to be an effective method of identifying volcanoes from a field, under-predicting height and area by 4% and over-predicting volume by 13%. By comparison, the closed-contour method under-predicts height, area and volume by 10%, 50% and 45%, respectively. In Chapters 3 and 4 we use the MBOA to identify seamounts from multi-beam bathymetry to study the relationship between seamount formation and axial morphology along ISRs.

In the above introduction, additional or anomalous magma supply influences an ISR by the presence of on- or near-axis hotspots or subduction zones. Magma supply also is considered anomalous when the axial morphology is not consistent along segment or between segment offsets. Global observations of the bathymetry along MORs at fast, intermediate and slow rates (Carbotte et al., 2004; Supak et al., 2007) demonstrate that differences in axial depth across ridge offsets are correlated with the direction of ridge migration in the fixed hotspot reference frame. Carbotte et al. (2004) show that the

shallower segment across an offset is usually the segment leading with respect to the direction of ridge migration (Carbotte et al., 2004; Katz et al., 2004; Supak et al., 2007) (Figure 1.8). To generate a shallower segment across an offset, Katz et al. (2004) had to couple their asymmetric flow patterns produced by ridge migration with a focusing of melt. This indicates that as the ridge migrates over the asthenosphere oblique to the spreading direction, melt must be focused beneath the leading segment end. Unlike the influence of a hotspot, the effects of enhanced melting due to ridge migration are constrained to a single segment.

If melting is enhanced when the ridge migrates at a direction oblique to the spreading direction, what happens to the volcanic and tectonic features when the spreading direction is oblique to the stretching direction (i.e., the direction the plates are being pulled apart)? Such is the case at the Southwest Indian Ridge in the Indian Ocean, the Sheba Ridge in the Gulf of Aden, and the Reykjanes, Mohns, Knipovich ridges in the North Atlantic Ocean (Fournier and Petit, 2007). Earthquake focal mechanisms along these ridges reveal the spreading direction trends halfway between the stretching direction and the perpendicular to the deformation zone (i.e., perpendicular to the ridge-axis) (Fournier and Petit, 2007). Although, studies by Dauteuil and Brun (1993) on the Mohns ridge reveal fault strikes slipping parallel to the stretching direction within the deformation zone, but trending halfway between the stretching direction and perpendicular to the ridge axis outside of the deformation zone. The controls on the formation and evolution of faulting patterns at obliquely spreading MORs are a function of lithospheric strength and geometry (Van Wijk and Blackman, 2007), spreading rate (Tuckwell et al., 1996), and the amount of obliquity between the stretching direction and

a perpendicular to the deformation zone (Dauteuil and Brun; Fournier and Petit, 2007). In Chapter 5, we attempt to model in 3-D the relationship between fault orientation and oblique spreading in response to differently sized deformation zones and the amount of obliquity.

This study attempts to understand the response of the MOR when influenced by anomalous magma supply through hotspots, melt anomalies and ridge migration, or anomalous spreading conditions when the stretching direction is oblique to spreading. We try to answer three main questions surrounding the generation of oceanic crust at mid-ocean ridges: 1) what is the most efficient and accurate way to identify volcanic edifices from gridded elevation data sets, 2) how does magma supply influence the formation and distribution of seamounts along mid-ocean ridges, and 3) how does the shape of the lithosphere and the amount of obliquity between the spreading and stretching directions along mid-ocean ridges influence the creation of faults within the deformation zone? The answers to these questions are included in Chapter 6.

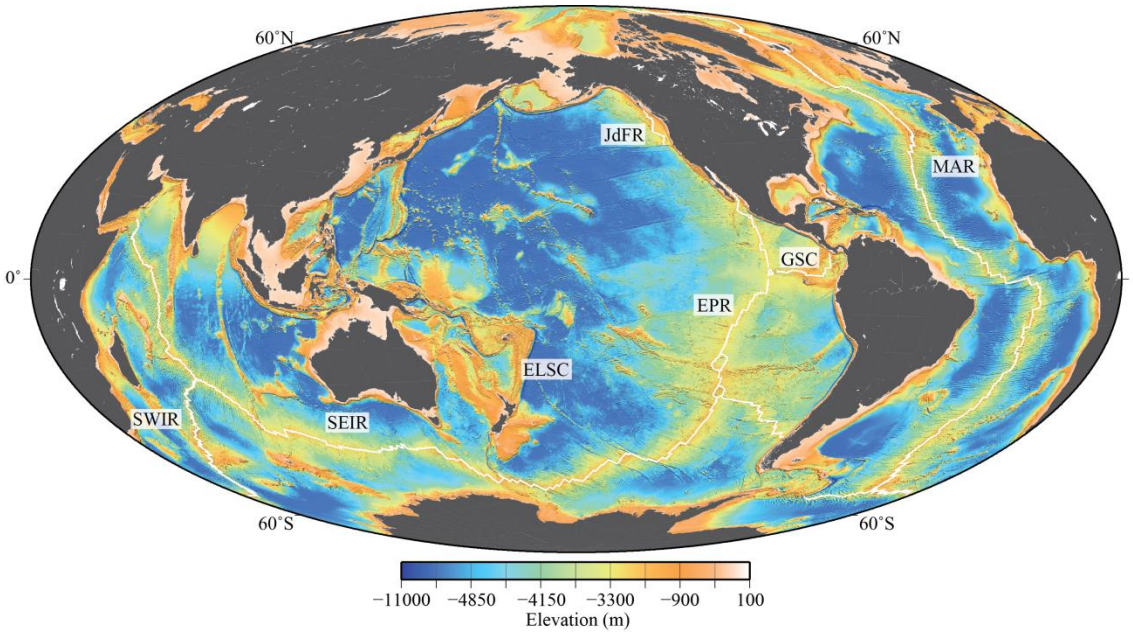

Figure 1.1. Global map of the mid-ocean ridge system (white line). Warmer colors indicate areas of higher elevation. SWIR, Southwest Indian Ridge; SEIR, Southeast Indian Ridge; ELSC, Eastern Lau Spreading Centers; JdFR, Juan de Fuca Ridge; EPR, East Pacific Rise; GSC, Galápagos Spreading Centers; MAR, Mid-Atlantic Ridge.

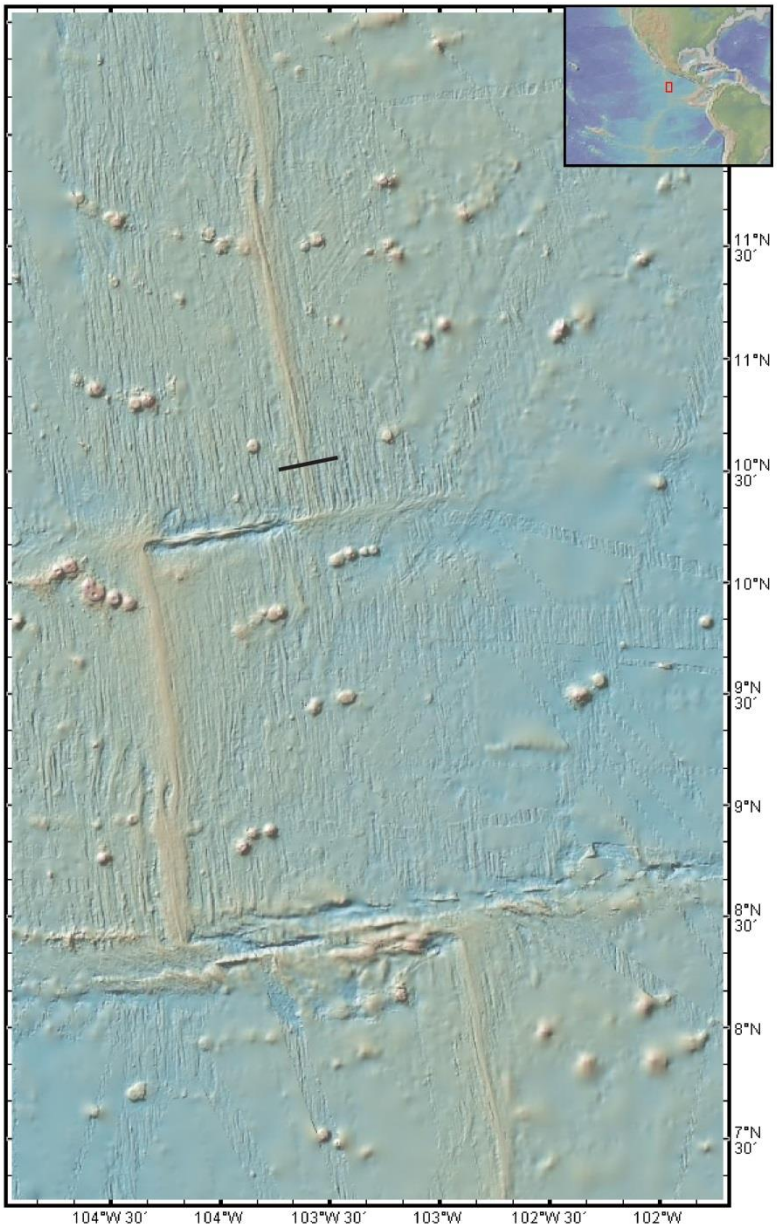

Figure 1.2. Axial morphology along the East Pacific Rise. Black line indicates profile in Figure 1.3. Map from GeoMapApp.

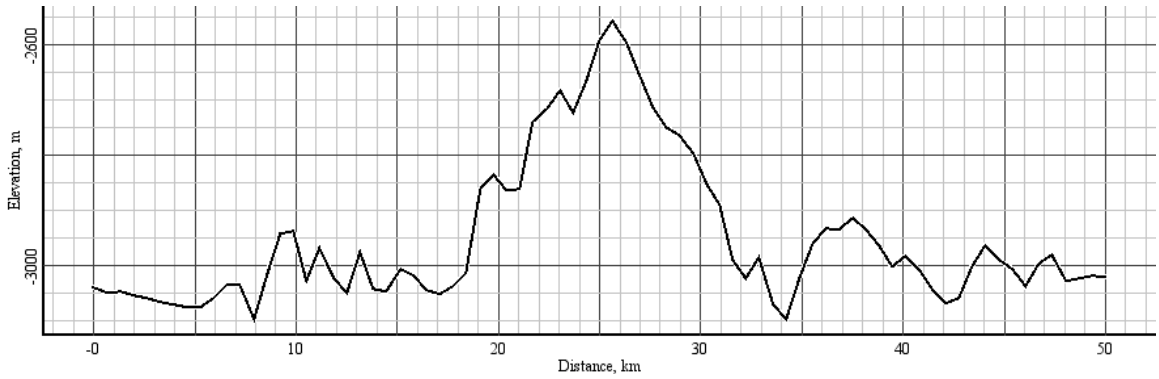

Figure 1.3. Profile from Figure 1.4. Note the broad axial high extends for 15 km, with a narrow peak 1-2 km wide. Vertical elevation is less than 400 m.

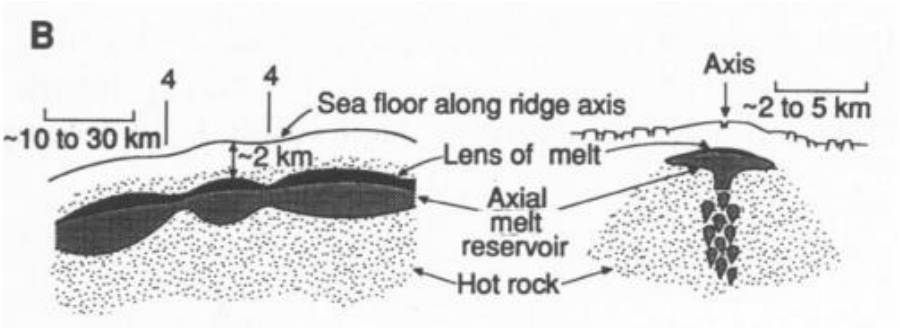

Figure 1.4. Distribution of melt lens along and across fast spreading mid-ocean ridge. Image from Macdonald et al. (1991).

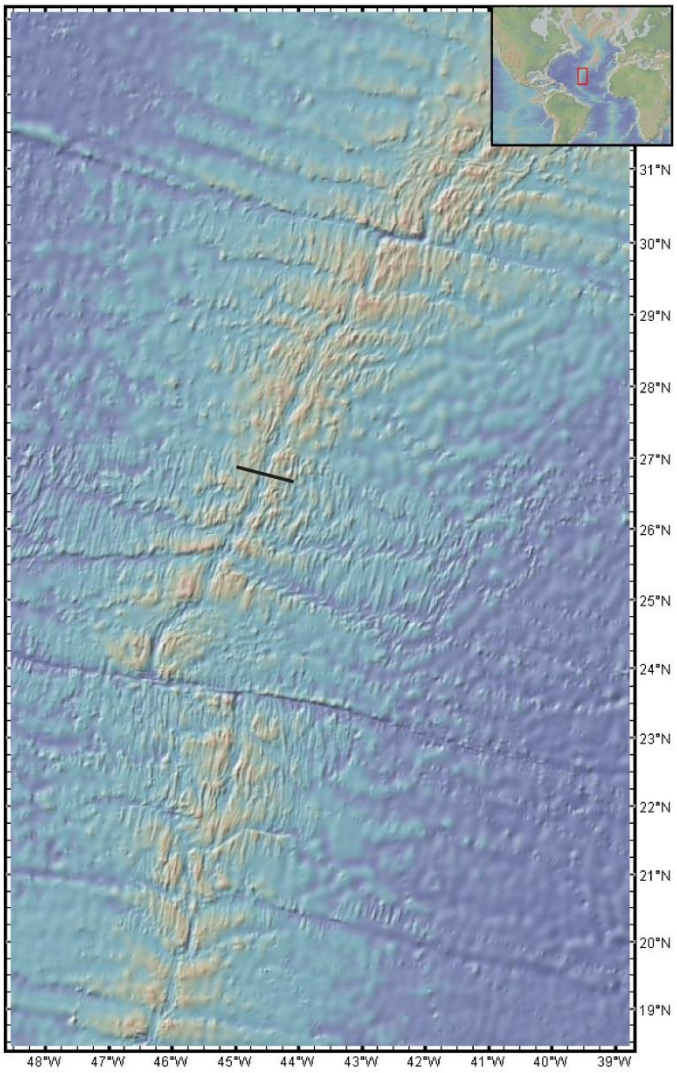

Figure 1.5. Axial morphology along the Mid-Atlanitc Ridge. Black line indicates the profile shown in Figure 1.5.

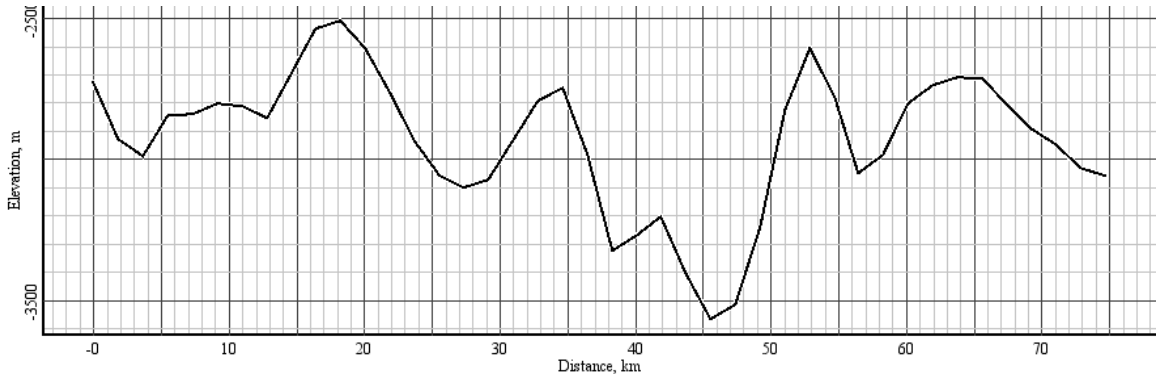

Figure 1.6. Profile from Figure 1.4. Note the axial rift valley is 40 km wide, with a 10-15 km wide median axial valley. Also, note the 1 km vertical offset.

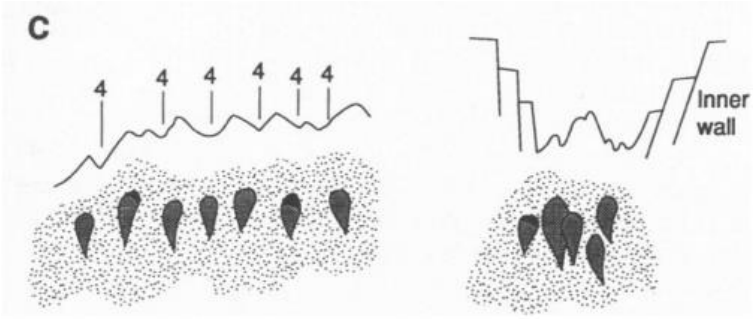

Figure 1.7. Distribution of magma along and across a slow spreading mid-ocean ridge. Image from Macdonald et al. (1991).

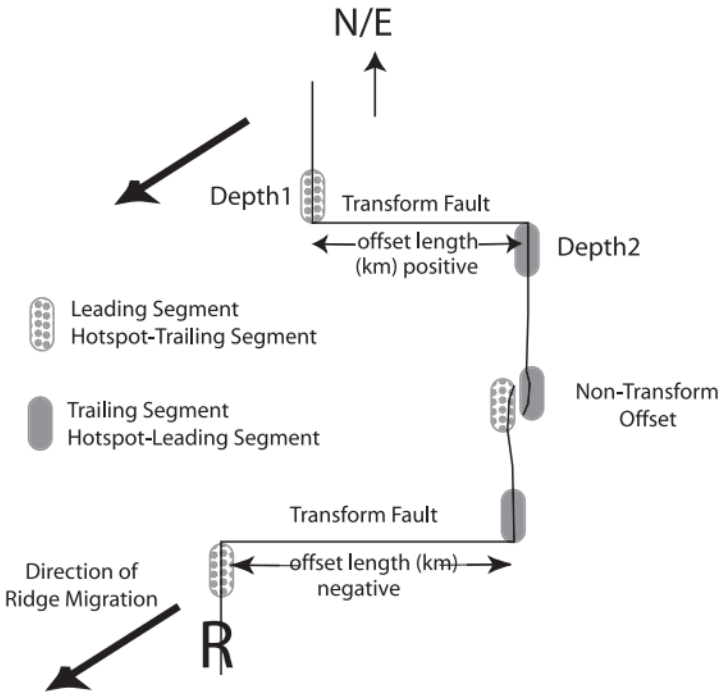

Figure 1.8. MOR segments offset in the direction of ridge migration at ridge axis discontinuities are termed leading segments, and those segments with an opposite sense of offset are termed trailing segments. Image from Supak et al. (2007).

CHAPTER 2: THE MODIFIED BASAL OUTLINING ALGORITHM

Volcanic edifices represent the principle visible end product of the magmatic processes responsible for accreting crust, altering the landscape, and posing a geohazard risk. While studies of individual volcanoes provide important insights into their geological behavior, volcanoes commonly appear in clusters, chains, fields or arcs. Representing relationships within and among these groups can be quite challenging, since hundreds of individual edifices can be involved, raising the need for automated methods to efficiently cope with such large numbers. Characterizing size, shape, and spatial distribution of volcanic edifices provides insight into the growth, erosion, disruption to the surrounding landscape, and assessment of geohazards posed by volcanic processes (e.g., Thouret, 1999). The accurate description of volcanic landforms, however, relies on the ability to accurately outline the basal boundary of the feature, which is often difficult to identify consistently and objectively.

Until recently, the limited horizontal and vertical resolution of most topographic maps necessitated the use of field studies to accurately delineate volcanic edifices from the surrounding landscape. Recent advances in technology have significantly improved the accuracy and spatial coverage of digital elevation models (DEMs), spawning new interest in automating studies of volcano geomorphology (e.g., Bemis et al., 2011; Favalli et al., 2009; Fornaciai et al., 2012; Grosse et al., 2012; Rodriguez-Gonzalez et al., 2012). In the submarine and extraterrestrial environments, DEMs have long been the most practical way to identify and characterize volcanic edifices. There are a variety of

automated methods devised for isolating and identifying volcanic features from elevation data (e.g., Behn et al., 2004; Bohnenstiehl et al., 2008; Cochran, 2008; Favalli et al., 2009; Hillier, 2008; Kim and Wessel, 2008; Wessel, 1998).

In a companion paper, Bohnenstiehl et al. (2012) introduce the Modified Basal Outlining Algorithm (MBOA), a new method of identifying topographic highs from DEMs. The MBOA uses a closed-contour algorithm similar to Bohnenstiehl et al. (2008) and modifies it by including aspects of Hillier's (2008) routine to isolate variable elevation bases of seamounts from trackline bathymetric data. Here, we evaluate how the MBOA performs when compared to a standard closed-contour algorithm (Bohnenstiehl et al., 2008; Bohnenstiehl et al., 2012) and manually mapped volcanic edifices in the Springerville Volcanic Field (SVF) in southeastern Arizona (Condit, 2010). The SVF is well suited for this study because it contains hundreds of similar-age cones within a geographically restricted area that is covered by both a high-resolution DEM and a digital geologic map that delineates individual cinder cone boundaries defined by field observations.

2.1 Geologic Setting

The SVF is one of many continental cinder cone fields overlying the lithospheric transition zone between the Colorado Plateau and the Basin and Range (Condit et al., 1989). Much data has been acquired for the SVF, assessing its relationship to the Colorado Plateau and the Basin and Range, age relationships, patterns of volcanism, clustering and alignment of vents, and prediction of volcanic hazards (Condit, 1984, 1991, 2010; Condit and Connor, 1996; Condit et al., 1989; Condit et al., 1999; Condit and Shafiqullah, 1985; Connor et al., 1992; Cooper et al., 1990; Crumpler et al., 1989,

1994). Condit (2010) combined this work into a Dynamic Digital Map, which provides an interactive program of viewing and understanding complex relationships in the SVF (http://ddm.geo.umass.edu/).

One of the most distinctive characteristics of the SVF is the great abundance of cinder cones within the field (Figure 1). Condit et al. (1989) identified 409 vents; of which 368 vents were mapped in detail covering approximately 3000km2 of the SVF. Volcanic edifices were identified based on changes in the topographic slope and the petrology (C. Condit, pers. comm.), the details of which are described in Section 3.4. Most (~93%) of the lavas in the SVF are alkalic basalt and no coeval silicic centers or large composite volcanoes, and no high silica flows (Condit et al., 1989; Connor et al., 1992). The majority of identified vents are cinder cones; however, there are two lava shields, four fissure vents, five maar craters, and isolated spatter mounds on some of the older units (Condit and Connor, 1996; Connor et al., 1992). Of the 3000 km2, 2166km2 is volcanic outcrop. Condit et al. (1989) estimate ~300 km3 of volume was erupted in this area during the past 2 m.y.

Connor et al. (1992) suggest the low rates of magma production in the SVF facilitate the development of a monogenetic cinder cone field, rather than the growth of one or more polygenetic volcanoes. In areas of low magma supply rates, conduits are not maintained in the crust, forcing magma to find different pathways to the surface (Connor et al., 1992; cf. Fedotov, 1981). Indeed, Condit et al. (1989) estimate an average volcanic output rate of 1.5x10-4 km3/yr, which is two orders of magnitude smaller than the global mean eruption rate for continental volcanic fields (White et al., 2006).

2.2 Methods

2.2.1 Digital Elevation Data

The National Elevation Dataset is a compilation of elevation data derived from LIDAR, digital photogrammetry, cartographic contours, mapped hydrography, or, less commonly, Interferometric Synthetic Aperture Radar (Gesch, 2007; Gesch et al., 2002). For the SVF, DEMs at 1 and 1/3 arc-second (~30 m and 10 m, respectively) resolution are freely available through the Seamless Data Warehouse (http://seamless.usgs.gov). The absolute vertical accuracy measured against 13,305 geodetic control points spread throughout the United States has a root mean square error of 2.5 m for the National Elevation Dataset (Gesch, 2007). A regional image showing data from 1/3 arc-second DEM for the SVF is shown in Figure 1, along with the MBOA cinder cones within the SVF.

2.2.2 Closed-Contour Algorithm

Closed-contour algorithms operate by selecting the lowest elevation contours that encompass regions of significant positive relief. The choice of contour interval is a function of the vertical accuracy of the DEM and the available computing power, which in this study is set to 5 m unless otherwise noted. The closed-contour algorithm requires that a basal contour encircle at least two concentric closed contours at higher elevation, and the lowest concentric contour (the basal contour) must have a long-to-short ellipse axis ratio of less than 4. The appropriate choice for long-to-short elliptical axis ratio may vary depending on the geologic setting and what the user intends to identify; for example, if the goal is to identify volcanic ridges, a larger elliptical axis ratio (>4) will provide better results. Conversely, if one is attempting to avoid volcanic ridges and identify more conical volcanic edifices, a smaller (~2) elliptical axis ratio is more suitable. The long-to-

short ellipse axis ratio used in this study was determined from the axis ratio of cinder cones on the geologic map. Furthermore, the closed-contour algorithm, as implemented here, requires that the normalized misfit of the basal contour to its best-fitting ellipse does not exceed a threshold value of 0.5 (Bohnenstiehl et al., 2008; Bohnenstiehl et al., 2012). The maximum dimension of the basal contour also is constrained to be <2 km, which inhibits the grouping of spatially clustered or parasitic cones into a single edifice (Bohnenstiehl et al., submitted). Closed-contour algorithms can be effective methods for identifying volcanic edifices; however, they also can systematically underestimate the size of a volcanic edifice due to the assumption that all volcanic edifices have constant elevation bases (Bohnenstiehl et al., submitted). The product of the closed-contour algorithm is a set of quasi-circular constant elevation closed polygons, each defining an individual volcanic edifice.

2.2.3 The Modified Basal Outlining Algorithm

The Modified Basal Outlining Algorithm (MBOA) starts with the constant elevation edifice base returned by the closed-contour algorithm, and then modifies (moves down slope) the position of the base along a series of azimuthally distributed topographic profiles that pass through the peak of the edifice (Bohnenstiehl et al., submitted). The modification routine begins stepping out in the forward and reverse directions from the point where the topographic profile intersects the basal contour, and continues until one or more geometric criteria are met as described in detail by Bohnenstiehl et al. (submitted). The primary geometric criterion used to stop the modification of the base is applied when the area to perimeter ratio decreases relative to the initial ratio of the topographic profile. A secondary geometric criterion stops the

modification when the slope of the outer portion of the profile falls below some portion (25% in this study) of the initial mean slope of the edifice (Bohnenstiehl et al., submitted). The product of the MBOA is a set of quasi-circular closed polygons, similar to the closed-contour algorithm, but with the critical difference that the MBOA outlines may cross elevation contours, and thereby mimic the downhill flow of volcanic products more accurately.

2.2.4 Geologic Field Mapping

Cinder cone boundaries (C. Condit, pers. comm. Jan. 2010) were converted to closed polygons and georeferenced to the DEM using Geographical Information System (GIS) software. Using this method, we were able to identify 321 cinder cones from the geologic map, which were restricted to only cinder cones with greater than 10 m in vertical elevation, limiting the database to 283 geologically mapped cinder cones. Condit (2010) distinguished cone boundaries, when associated with a lava flow, by using the break in slope at the base and the contact between cinders and lava, where it was exposed. The SVF is one of few volcanic fields where cinder cone boundaries were delineated separately from associated lava flows, which are often not topographically distinct [C. Condit, pers. comm. Jan. 2010]. This distinction between cinder cone and lava flow is important for our study; the closed-contour algorithm and the MBOA use only topography to identify volcanic edifices, so it is necessary to compare features that are topographically similar in order to compare the performance of the different methods applied to a natural dataset. Modification of the topography due to erosion or anthropogenic activity is assumed to be negligible during the decade between initial mapping and the creation of the DEM.

2.2.5 Size and Shape Quantification

Cinder cone size and shape estimates were compared for the outlines determined using the closed-contour algorithm, the MBOA, and the geological map from Condit (2010). For this study, the size of a cinder cone is represented by its maximum height, area and volume, and its shape is quantified by the maximum height-to-basal radius ratio (h/r). The height-frequency distribution of cones in the SVF also is reported for each of the methods, as this is a common method of comparison among volcanic fields. The sensitivity of the closed-contour algorithm and the MBOA results to the resolution of the DEM and contour interval are discussed.

The height, area and volume estimates of each cinder cone for each method were calculated by importing the basal outlines into the statistics portion of the MBOA. For a constant elevation base returned by the closed-contour algorithm, the height is calculated as the difference in elevation between the peak and basal contour. However, for variable elevation bases returned by the MBOA and the geologic map, a three-dimensional surface must be fit passing through the closed polygonal base, and the height is determined relative to the elevation of this surface beneath the peak, similar to Favalli et al. (2009). The planimetric area of the base and the volume of the cinder cone are determined by integrating over the closed polygon base and from the base to the three-dimensional surface of the edifice, respectively.

The steepness of a volcanic cone is an important measure of shape (e.g. Bemis et al., 2011; Favalli et al. 2012; Hooper and Sheridan, 1998; Wood, 1980a, b). As Bemis (1995) noted, however, the angle of its slope is not as sensitive to variance in cone shape as the h/r ratio. Therefore, only h/r values are examined here. As the basal shape of an

edifice is typically irregular, the reported radius is that of an equivalent-area circle. For each dataset, the mean h/r value and uncertainty in the mean are estimated using a bootstrap resampling (n=5000), with 95% confidence limits estimated using normal-theory intervals.

Scaling laws for the height-frequency distribution of monogenetic and polygenetic cones have been applied to many cone fields, in both subaerial (e.g., Pérez-López et al., 2011) and submarine (e.g., Jordan and Menard, 1983; Scheirer and Macdonald, 1995; Smith and Cann, 1990, 1992; Smith and Jordan, 1987, 1988; White et al., 1998) environments. Jordan and Menard (1983) developed this measurement to relate the distribution of apparent seamount heights in single-beam bathymetry per unit length of ship track to the predicted distribution of actual seamount heights per unit area of seafloor. Other researchers have since investigated the size-frequency scaling of seamount populations identified in two-dimensional gridded elevation datasets, typically reporting either a self-similar power law (e.g., Wessel, 2001; Wessel and Lyons, 1997) or exponential (e.g., Smith and Cann, 1992; Smith and Jordan, 1987, 1988) model. Here, we estimate the characteristic height (β-1) and cinder cone density (ν) of the SVF cinder cone population, following the exponential model described in Jordan and Menard (1983): $N(h)=\nu e^{-h\beta}$, where N(h) is the predicted cumulative number of cinder cones of height greater than or equal to h. The model parameters are determined using a robust (L1-norm) linear regression of log(N) versus h binned at 5 m intervals. For the regression, the parameter estimates obtained from a bootstrap resampling do not exhibit a normal distribution; consequently, the 95% confidence intervals are determined empirically from the {2.5%, 97.5%} quantile intervals.

2.3 Results

Visually inspecting the basal outline produced by each method reveals some interesting and notable differences. Primarily, the choice of contour interval is a more important factor affecting the number of cinder cones identified by the automated methods than the resolution of the DEM. Consider the spatial subset of the data shown in Figure 2; using a 5 m contour interval the MBOA identified 6 cinder cones on the 1/3 arc-second DEM (Figure 2a), but only 5 cinder cones on the 1 arc-second DEM (Figure 2b). However, for a 20 m contour interval, the MBOA identifies three cinder cones on the 1/3 arc-second DEM, but only identifies two cinder cones on the 1 arc-second DEM. Small differences in the shape of the outlines for the consistently identified cinder cones are a result of the loss of detail from the 1/3 to the 1 arc-second DEM.

When the morphometric characteristics derived using each method are compared, the closed-contour algorithm systematically underestimates maximum height, area and volume when compared to either the MBOA or the geologic field map. For the MBOA results, the percent change in height, area and volume using a 5 m contour interval on a 1/3 arc-second DEM show a 10%, 80% and 100% increase in maximum height, area and volume compared to the closed-contour algorithm (Figure 3a). Results from the closed-contour algorithm show 5%, 50% and 45% decrease in maximum height, area and volume when compared to the geologic map (Figure 3b). However, the MBOA results differ from the geologic map by only -4%, -4% and +13%, respectively (Figure 3c).

The difference between the ground reference and the MBOA results increases when using a 5 m contour interval on a 1 arc-second DEM (Figure 4). Importantly, 78 fewer cinder cones are identified in the MBOA results from the 1 arc-second DEM than

the 1/3 arc-second DEM. Increasing the contour interval to 10 m with the 1/3 arc-second DEM causes the MBOA to detect 106 fewer cinder cones than when the procedure is run for a 5 m contour interval. However, for those edifices that are detected, the size parameters show little change relative to the 5 m case (Figures 3c and 5a). Furthermore, a 20 m contour interval (1/3 arc-second DEM) identifies 184 fewer cones than the 5 m contour interval, and the height, area and volume of the cones that are detected under-represent the ground reference observations by 27%, 28% and 5%, respectively (Figure 5b).

The h/r of the results for the SVF shows mean ratios of 0.163±0.007, 0.144±0.006, and 0.136±0.006 for the closed-contour algorithm, the MBOA and the geologic map results, respectively. The mean h/r values of the cones mapped using the closed-contour algorithm, the MBOA, and the geologic map are distinct at the 95% confidence level. As the closed-contour algorithm typically delineates the upper portion of the cone, with boundaries that exclude the lower flanks, somewhat higher h/r values are expected. However, these differences are small relative to the range (0.11-0.35) of h/r values reported across various cone fields (e.g., Bemis et al., 2011; Fornaciai et al. 2012; Hooper and Sheridan, 1998). This suggests that h/r values are relatively insensitive to the methodology used to define the outlines of cones.

The height-frequency distributions are well described by the negative model for all three methods, but there are some significant differences among methods in the resulting parameters of the model. For the MBOA data, the bootstrap estimate of characteristic height (β-1=44.07 {40.7, 46.9}) lies above the empirically defined 95% confidence limits for the characteristic height estimates using the closed-contour (β-

1=39.98 {38.3, 41.9}) and geologic mapping (β-1=39.01 {34.4, 42.0}) measurements, which are not statistically different from each other (Figure 7). The expected cinder cone density estimates obtained from the MBOA (ν=512.48 {466.9, 619.5}) and geologic map data (ν=539.70 {437.1, 703.9}) are significantly larger than the cone density estimated using the closed-contour algorithm results (ν=409.37 {371.9, 446.8}). The closed-contour algorithm systematically underestimates the size of cones relative to the other two methods, effectively shifting the height-frequency curve toward smaller heights and yielding a smaller cone density. At small heights there is a roll-off in the cumulative height-frequency data, particularly for those defined by field mapping (Figure 7). Such departures in scaling are commonly interpreted to indicate that the dataset is incomplete for cinder cones smaller than this threshold value (e.g., Bohnenstiehl et al., 2008).

2.4 Discussion

Improved understanding of the complex relationships between volcanism, tectonics, and erosion depends on developing methods to perform quantitative geomorphic measurements of volcanoes that are objective, consistent, efficient and accurate. Advances in the accuracy and precision of DEMs have opened the door to a new generation of automated methods for identifying volcanic products, with volcanic edifices being the most obvious target. For characterizing individual volcanoes, geological field mapping is the traditional method and remains a viable option. However, the broad view afforded by the DEM-based analysis offers several advantages for automated methods over the traditional method, including speed and objectivity. These factors are most critical for defining the overall characteristics of larger numbers of related volcanoes in a particular setting, such as those that commonly occur at subduction

arcs, spreading ridges, seamount chains or volcanic fields. Two ways of comparing the results of automated to manual identification of volcanic edifices are to (1) assess the ability of each to identify individual volcanoes and (2) compare their results for a volcanic field as a whole.

The selection of a constant elevation base generated by a closed-contour algorithm is sensitive to the choice of contour interval (Bohnenstiehl et al., submitted) and forces a constant-elevation basal outline. Consequently, the maximum height, area and volume of the SVF cinder cones are systematically underestimated using this procedure, compared to geologic mapping and MBOA results (Figure 3). Decreasing the contour interval reduces these differences; however, it also increases the number of closed-contours to be evaluated, thus reducing the efficiency of this approach. Moreover, this method cannot allow for variable elevation basal outlines, which further contributes to the underestimation of cone size by ignoring the role of pre-existing topography. For these reasons, we suggest that results derived from simple closed-contour algorithms be treated with caution.

By adjusting the closed-contour bases downslope using simple geometric rules, the MBOA attempts to overcome the limitations inherent to the closed-contour algorithm. However, because the MBOA uses closed-contours to establish the number of cones, their abundance and spatial distribution remain dependent on the choice of contour interval. In light of these results, we recommend using the smallest contour interval that the DEM can support within the capability of the user's available computer processing hardware.

With the 1/3 arc-second DEM contoured at 5 m, the MBOA identifies similar features as those mapped by Condit (2010) (e.g. Figure 2a); however, in some cases, the MBOA groups two or more of Condit's (2010) cones into a single edifice, or conversely, the routine may split the mapped cones into multiple edifices. Even where the cones are matched one-for-one, the details of the boundaries can differ slightly (Figure 2). Yet, the MBOA and geologic map results return similar estimates for total area and volume of the cones (Figure 3), and the populations exhibit similar morphometry (Figures 6 and 7). Increasing the contour interval from 5 m to 20 m results in a decrease in the maximum height (27%), area (28%) and volume estimates (5%) relative to the geologic map data. Furthermore, using a contour interval of 20 m identifies 184 fewer cinder cones in both the closed-contour algorithm and the MBOA databases.

The statistics derived for a population of cones can be influenced by the method used to delineate the cone boundaries (Figures 6 and 7). With respect to mean h/r values, however, our results indicate that this parameter is largely insensitive to the method applied. As h/r values are among the most commonly reported statistics for cone fields (e.g. Bemis et al., 2011; Fornaciai et al., 2012; Hooper and Sheridan, 1998), they are a potentially good indicator of the aggregate eruptive and erosive processes at work in a particular volcanic field. This assessment, however, cannot account for the differences in criteria used by researchers to select cones for morphometric analysis. While automatic procedures such as the MBOA attempt to map all cones exceeding a certain size threshold, other studies may show a bias in the percentage of younger, steeper-sided cones, which are typically more identifiable in the landscape.

Although a negative exponential height-frequency model fits all three datasets generated for the SVF, our study demonstrates that the estimated scaling parameters are sensitive to the method used to delineate the edifices. Moreover, for small cones, there is a notable roll-off in the cumulative height data obtained from the geologic map; whereas, for the both automated methods of analysis, the populations more closely follow the predicted model (Figure 7). This reflects the inclusion of a larger number of small cone-shaped highs (potential volcanoes) that where not defined by Condit (2010). However, cinder cones in the SVF also may have a natural minimum height threshold, below which another style of volcanism appears. For example, very small and short-lived magma conduits are likely to produce only limited quantities of tephra, have significantly lower tephra-lava ratios, or fail to focus from fissures to point-source vents. Similarly, in a low magma supply region like the SVF (Connor et al., 1992), the small size and short-lived nature of conduits may restrict the maximum height of the cone. This could provide an explanation for the departure of the data from the exponential model at heights > ~180 m noted for all three methods (Figure 7).

2.5 Conclusions

The Modified Basal Outlining Algorithm provides a new method of identifying topographic highs from gridded elevation datasets. When compared to cinder cones mapped by Condit (2010), the MBOA reproduces aggregate data for cinder cones within the SVF to within -4% in maximum height, -4% in area and +13% in volume; whereas the closed-contour algorithm underestimates the geologic map data by 10%, 50% and 45%, respectively. Because the MBOA depends on a closed-contour algorithm, the number of volcanoes identified by the MBOA retains some sensitivity to the contour

interval used. The MBOA, however, uses more of the topographic information within the DEM and therefore is able to better delineate the margins of a volcanic edifice, which often do not lie along a line of constant elevation.

The method used to define the cone boundaries can influence both the estimated scaling parameters and h/r values. For the mean h/r values, however, the resulting differences are small relative to the ranges reported between various cinder cone fields (e.g., Bemis et al., 2011; Fornaciai et al., 2012; Hooper and Sheridan, 1998). This indicates that h/r values may be robust indicators of cone steepness, and therefore reflect the integrated history of eruptive and erosional processes shaping volcanic edifices. The MBOA provides a new tool in physical volcanology, which can be applied in various environments. The objective nature of this analysis provided by the MBOA is ideal for characterizing the aggregate statistics of entire volcanic fields in any area for which a gridded elevation dataset exists. Here, the analysis of the MBOA shows that it is a significant improvement over the more basic closed-contour algorithm, while being able to obtain results directly comparable to those from field geologic mapping in far less time. The lack of one-to-one correspondence between field-mapped cones and the MBOA picks highlights the subjectivity involved in defining a "volcano" but the MBOA is very useful for regional studies, particularly comparing the characteristics of different volcanic fields, and comparative studies, in which consistency and objectivity are critical. This includes volcanic terrains in the submarine and extraterrestrial environments, where topographic data may be the primary source of information available for the assessment of landforms.

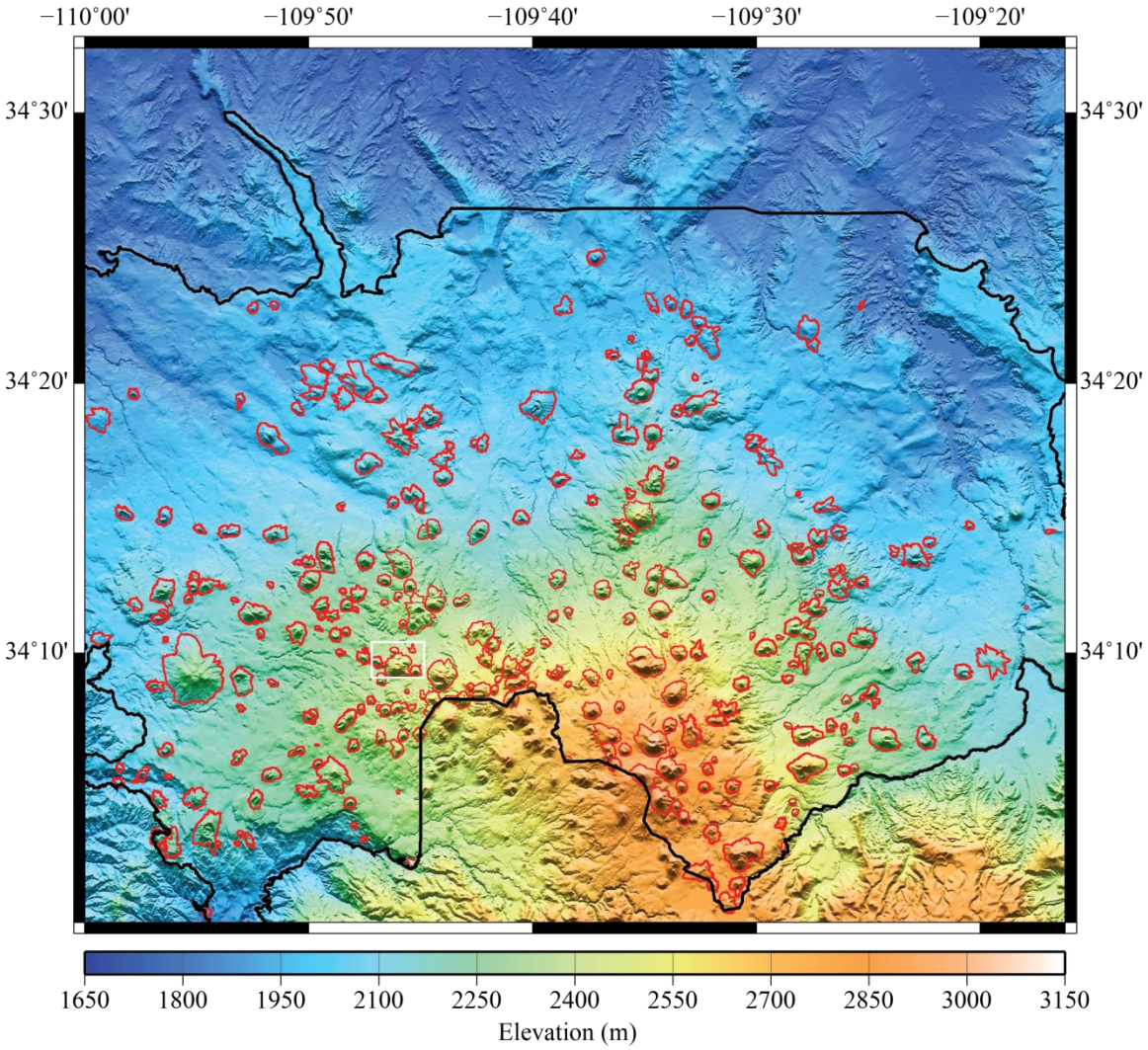

Figure 2.1 Modified Basal Outlining Algorithm (red lines) perimeters for cinder cones in the Springerville Volcanic Field, located in southeastern Arizona. Black outline shows the limits of the volcanic field mapped by Condit et al. [2010]. 1/3 arc-second digital elevation model was obtained through the U.S. Geological Survey's Seamless Data Warehouse (http://seamless.usgs.gov). White box indicates area in Figure 2.2. Map produced using the Generic Mapping Toolbox by Paul Wessel (http://gmt.soest.hawaii.edu).

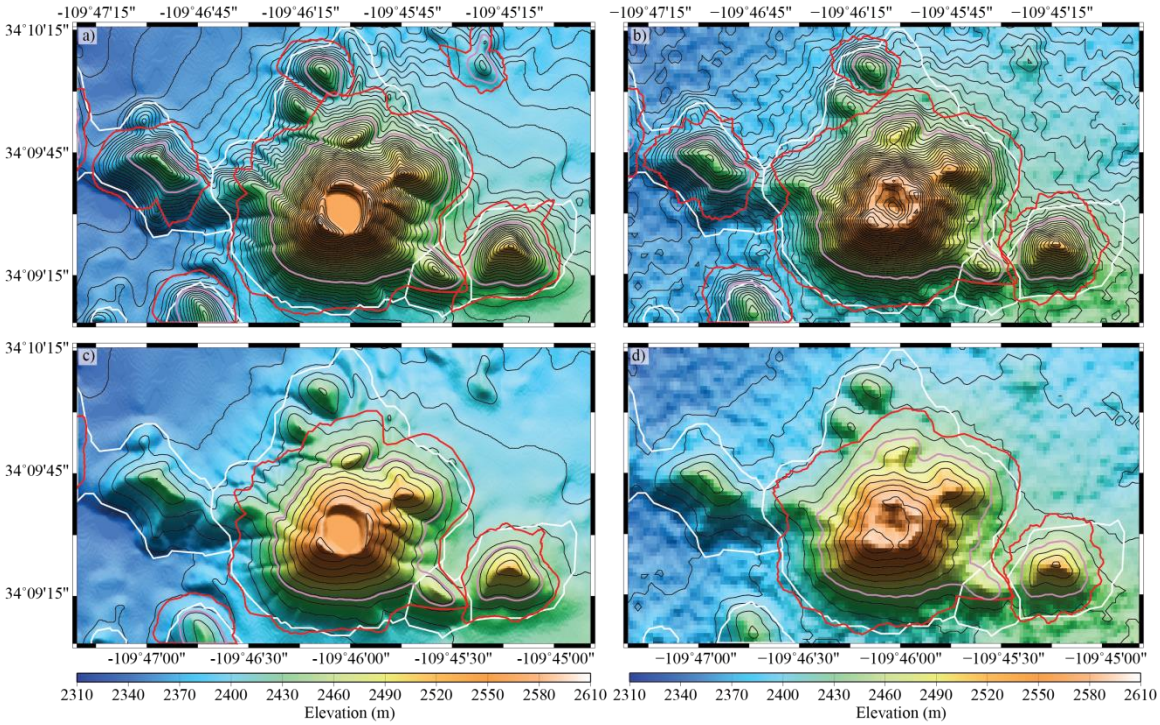

Figure 2.2 Zoomed in view of cinder cones in the SVF. Images in the left column are from a 1/3 arc-second DEM, images in the right column are from a 1 arc-second DEM. White lines represent the basal outlines derived from the geologic map (Condit, 2010), results from the MBOA (red) and closed-contour algorithm (violet) using 5 m (black lines, top row) and 20 m (black lines, bottom row) contour intervals.

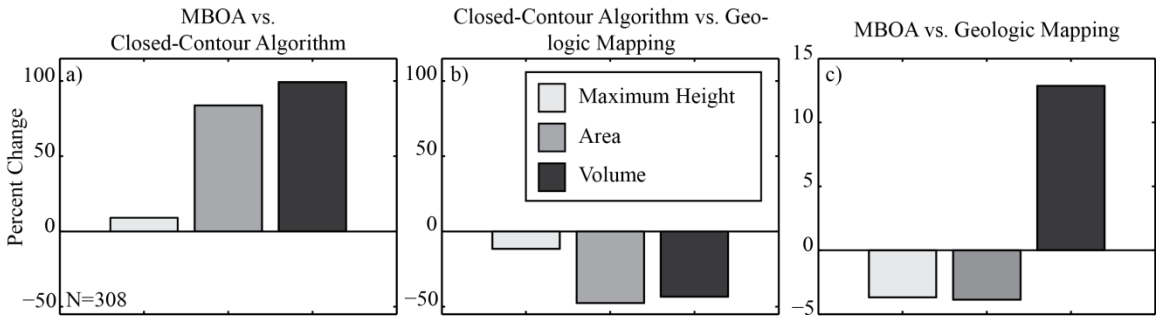

Figure 2.3 Percent change in maximum height (off-white), area (grey) and volume (dark grey) for a) the MBOA versus the closed-contour algorithm; b) the closed-contour algorithm versus the geologic map; and c) the MBOA versus the geologic map. These results are for a 1/3 arc-second DEM with a 5 m contour interval. The number of cinder cones identified using the closed-contour algorithm and the MBOA are noted. Also note the change in the vertical axis for c).

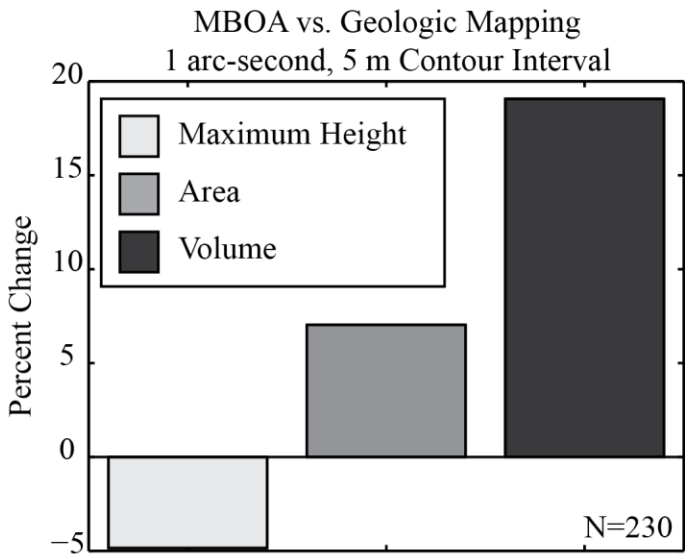

Figure 2.4 Percent change from MBOA to the geologic map sizes for a 1 arc-second DEM and 5 m contour interval. Colors and symbols are the same as Figure 2.3.

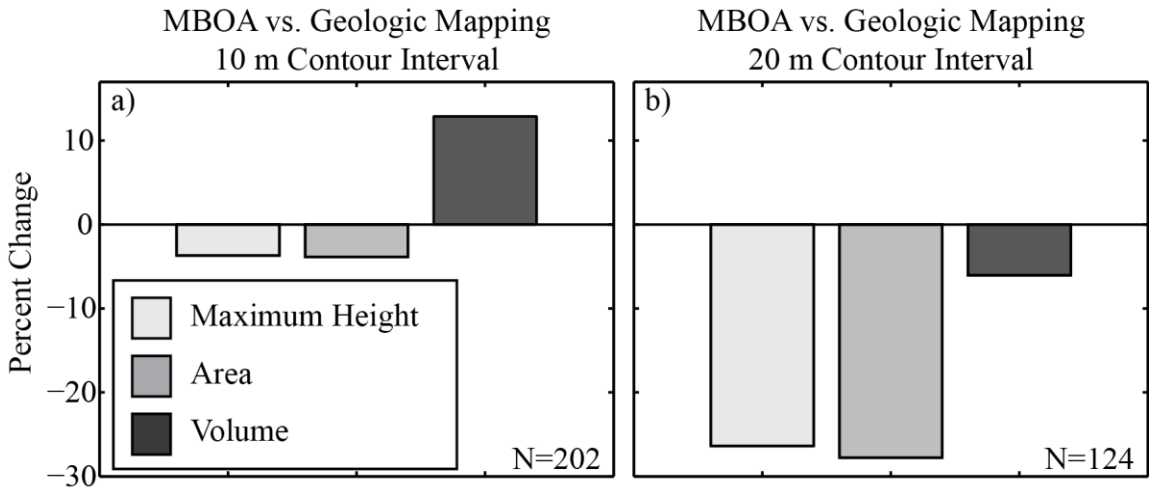

Figure 2.5 Percent change in the MBOA versus the geologic map on a 1/3 arc-second DEM and a) 10 m contour interval and b) 20 m contour interval. Note the decrease in number of cinder cones with increase in contour interval. Color and symbols are the same as Figure 2.3.

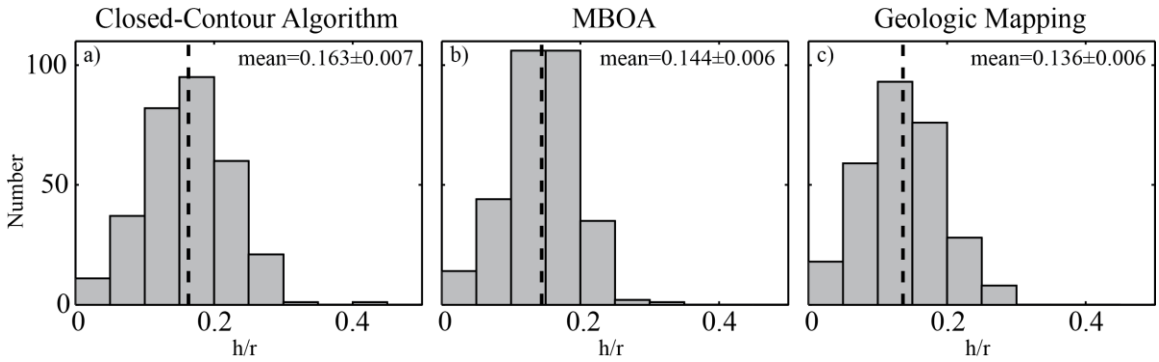

Figure 2.6 Height-to-basal radius ratios (h/r) for a) closed-contour algorithm, b) the MBOA and c) geologic map. Dashed line shows the mean h/r value. Uncertainty in the mean is estimated from a set of 5000 bootstrap resamplings, as described in the text.

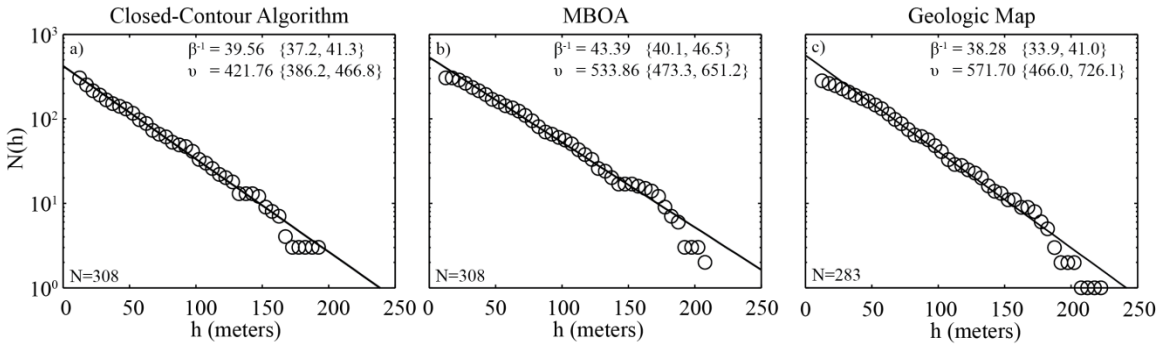

Figure 2.7 Height-frequency distribution for a) closed-contour algorithm, b) the MBOA and c) geologic map. Circles show the cumulative number of cinder cones at a particular height (in 5 meter bins). Solid line represents the best fit of the data to a negative exponential height-frequency model, determined using an L1-norm linear regression. The mean parameter values and 95% confidence interval are determined empirically from a set of 5000 bootstrap resamplings.

CHAPTER 3: SEAMOUNT ABUNDANCE, VOLUME AND SPATIAL DISTRIBUTION ALONG THREE HOTSPOT-INFLUENCED INTERMEDIATE SPREADING RATE RIDGES

The global mid-ocean ridge (MOR) system shows morphological and structural characteristics systematically related to spreading rate (Macdonald, 1982; Small and Sandwell, 1989; Perfit and Chadwick, 1998). MORs are typically categorized into fast, intermediate and slow spreading ridges with breaks between categories based on large-scale changes in these characteristics (e.g., Macdonald, 1982; Small and Sandwell, 1989; Perfit and Chadwick, 1998). Fast-spreading ridges (>90 mm/yr) exhibit ridge crest morphology of broad axial topographic highs that are segmented by regional transform faults (offsets of 10's-100's km) and overlapping spreading centers (offsets 1's-10's km) (e.g., Macdonald et al., 1991). Volcanism is dominated by fissure fed eruptions at the centers of these segments, with some central-vent volcanoes forming near the segment ends (White et al., 1998, 2002a, b; Bohnenstiehl et al., 2008). Slow spreading ridges (<40 mm/yr) exhibit a morphology characterized by broad axial valleys, segmented by transform faults (offsets 10's-100's km) and non-transform offsets (offsets <10 km) (e.g., Macdonald et al., 1991; Smith and Cann, 1993). The centers of slow-spreading ridge segments are typically shallower than segment ends, with volcanism dominated by axial volcanic ridges and isolated point-source seamounts (Smith and Cann, 1990, 1992, 1993, 1999; Smith et al., 1995; Searle et al., 2010). The style volcanism at fast and slow spreading ridges therefore represents two distinct modes of axial accretion. What controls

these two modes, and the implications for the construction of ocean crust, remains enigmatic. Many studies have used the abundance and size distribution of seamounts to probe the nature of changes in the magma plumbing system along the MOR (e.g. Smith and Cann, 1990, 1992; Smith et al., 1995; White et al., 1998, 2002a, b, 2008; Behn et al., 2004; Bohnenstiehl et al., 2008; Cochran, 2008), recognizing that these volcanoes are the surface manifestation of the magma plumbing system (Bishop, 2007).

At the transition between fast and slow spreading, intermediate spreading-rate ridges (ISRs) exhibit a wide range of axial morphology over a narrow range of spreading rates; yet, there has been no systematic study examining the global relationships between volcanism and other fundamental characteristics at ISRs. Here, we examine the distribution of seamounts forming at three hotspot-influenced ISRs and their correlation with axial morphology: the Juan de Fuca Ridge (JdFR), the Galápagos Spreading Center (GSC) and the Southeast Indian Ridge (SEIR) (Figure 3.1). These ISRs exhibit variation in axial morphology and magma supply from nearby magmatic hotspots or melt anomalies, allowing us to examine the influence of locally increased magma budget independent of spreading rate. We test the relationship between volcano distribution and axial morphology based on the expectation that volcano abundance and volume will be greater near the ends of axial high segments (White et al., 1998, 2002a, 2002b, 2008; Bohnenstiehl et al., 2008) and sporadically distributed along axial valley segments (Smith and Cann, 1990, 1992, 1993; Smith et al., 1995).

3.1 Intermediate Spreading-Rate Ridges

We analyze contiguous sections of the Juan de Fuca Ridge (JdFR, including the Explorer and Gorda segments), the Galápagos Spreading Center (GSC) and the Southeast

Indian Ridge (SEIR) where high-quality shipboard multi-beam bathymetry is available (Figure 3.1). These ridges spread at rates from <40 to 76 mm/yr (spanning the full range of intermediate rates). Geochemical data is used to indicate the extent of influence by hotspots or melt anomalies to the along-axis gradient in magma supply at each ridge. Portions of each ridge have been imaged with active source seismic methods, providing constraints on crustal thickness and the distribution of melt lenses in the crust.

Axial morphology at ISRs falls into four categories on the basis of topographic expression and shallow crustal structure: axial high, rifted axial high, shallow axial valley and transitional segments (Baran et al. 2005). The axial high morphology refers to a ridge segment with 250-400 m of increased elevation over a 15-20 km region across the spreading axis, similar in dimension and shape to the fast spreading (>90-150 mm/yr) East Pacific Rise (EPR). Axial high segments along the SEIR and EPR typically have magma lenses shallower than 1700 m below seafloor and on-axis seismic layer 2A thicknesses less than 350 m (Hooft et al., 1997; Baran et al., 2005). Rifted axial high segments are distinguished from axial highs by the presence of near-axis (<1 km) normal faults with 50-100 m high scarps, and also may have deeper magma lenses (2100-2500 mbsf) (Detrick et al., 2002; Baran et al., 2005) and a thicker on-axis seismic layer 2A (~460 m) (Baran et al., 2005). Shallow axial valley segments are characterized by an 8-15 km wide and 500-800 m deep valley that does not have the same magnitude of faulting observed along the Mid-Atlantic Ridge (MAR). Although, similar to their slow spreading (20-45 mm/yr) counterparts on the MAR, a magma lens has not been imaged beneath axial valley segments and the on-axis seismic layer 2A thickness (~800 m) is greater than axial high (<350 m) or rifted axial high segments (~460 m) (Detrick et al.,

2002; Baran et al., 2005). Transitional segments contain at least two types of axial morphology within the same segment that coincide with changes in the depth of the melt lens and thickness of seismic layer 2A (Cochran et al., 1997; Baran et al., 2005).

3.1.1 Juan de Fuca Ridge (JdFR)

The JdFR is approximately 950 km long including segments of the Explorer Ridge in the north and Gorda Ridge in the south. The Explorer ridge is 110 km in length, terminating in the north at the Revere-Dellwood-Wilson transform (Deschamps et al., 2007) and in the south by the Sovanco Fracture Zone. Spreading rate along the Explorer Ridge is ~44-60 mm/yr (Riddihough, 1984; Botros and Johnson, 1988; Deschamps et al., 2007), with a transitional axial morphology along the Southern Explorer Ridge (Figure 3.2). Michael et al. (1989) found enriched lavas suggesting an enriched mantle source has been present beneath the Southern Explorer Ridge for an extended amount of time.

Across the Sovanco Fracture Zone to the JdFR, spreading rate remains at 56 mm/yr (Wilson, 1993) and axial morphology is dominated by rifted axial highs, with the exception of the axial valley along the West Valley segment (Figure 3.2). Two melt anomalies are located along the JdFR, one near the center of Endeavour segment where the Heckle Seamount Chain projects to the axis, and another at the Cobb Hotspot beneath Axial Seamount (Figure 3.2). Lava samples suggest the influence from these two hotspots is limited to the Endeavour (Chadwick et al., 2005) and Axial (Embley et al, 2000; Chadwick et al., 2005) segments (Figure 3.2); however, Carbotte et al. (2008) argue based on south-to-north gradients in seafloor relief, presence and depth of the crustal magma lens and crustal thickness on- and off-axis that the Cobb hotspot influences crustal production along CoAxial to Cleft segments. Ridge segment boundaries are

overlapping spreading centers north of Axial segment and non-transform offsets to the south (Figure 3.2).

On the North Gorda ridge, spreading rate remains near 56 mm/yr (Wilson, 1993; Carbotte et al., 2008); yet, axial morphology is distinctly different from the Cleft Segment with a 6.5 km wide, 400 m deep axial valley that widens and deepens to the south (Hooft and Detrick, 1995). Gorda Ridge is segmented by non-transform offsets into 5 segments (Figure 3.2) (Rona et al., 1992; Chadwick et al., 1998). Spreading rates decrease to ~22 mm/yr near the Mendocino Transform (Atwater and Mudie, 1973).

3.1.2 Galápagos Spreading Center (GSC)

The Galápagos Spreading Center (GSC) separates the Cocos and Nazca plates, extending from the Galápagos Triple Junction with the East Pacific Rise at 102°W to the Panamá Fracture Zone at 83°W (Figure 3.3). Within our study area from 98°W to 84.5°W, ridge axis morphology is variable, and spreading rate increases from 52 mm/yr near 98°W to 60 mm/yr near 85.5°W (DeMets, 1990). The eastern portion of the GSC from 84.5°W to 91°W is offset by several large transform faults, although between the Galápagos Transform (91°W) and the Galápagos Triple Junction (102°W), the GSC is offset by many westward propagating rifts (Canales et al., 1997). Except for the Galápagos and Inca Transforms (91°W and 85°20'W), segments are bounded by overlapping spreading centers closer to the hotspot and non-transform offsets farther away (Figure 3.3). Geochemical analyses of lavas show the Galápagos Hotspot is influencing the GSC from 95°30'W to 85°30'W, with a peak signature located near 91°W (Schilling et al., 2003; Sinton et al., 2003; Cushman et al., 2004; Christie et al., 2005). A series of volcanic chains, the Wolf-Darwin Lineaments, extend toward the GSC

(Figure 3.3). Mittelstaedt and Ito (2005) suggest that the Wolf-Darwin Lineaments are a result of volcanism aligning parallel to the lithospheric trajectories of least tensile stress induced by an expanding mantle plume. Ridge axis morphology transitions from an axial high near the Galápagos Transform to a deepening rifted axial high approaching the limit of the Galápagos plume influence. Outside of the Galápagos plume influence, GSC is an axial valley. Previous volcano distribution studies (Behn et al., 2004; White et al., 2008) along the GSC from 98°W to 89.5°W show an increase in seamount abundance with distance from the Galápagos plume, suggesting volcano abundance increases as magma supply decreases.

3.1.3 Southeast Indian Ridge (SEIR)

The SEIR is the longest ISR on Earth, extending between the Indian Ocean (25°S, 70°E) and Macquarie (63°S, 165°E) Triple Junctions and marking the boundary between the Australia and Antarctica plates (Cochran et al., 1997). In our study area, from 77° to 116°E, spreading rates range from 68 mm/yr in the west to 76 mm/yr in the east (Figure 3.4). Axial morphology along this section of the SEIR is made up of 3 axial highs, 9 rifted axial highs, 13 axial valleys and 4 transitional segments (Figure 3.4). Axial segmentation along the SEIR is characterized by 50-500 km long transforms, with sub-segmentation accommodated by overlapping spreading centers when axial morphology is an axial high or rifted axial high, or non-transform offsets when expressed as an axial valley (Royer and Schlich, 1988; Ma and Cochran, 1996; Small et al., 1999). The ASP hotspot is within 40 km of the SEIR (segments I2 and J1, Figure 3.4) (Scheirer et al., 2000; Supak et al. 2007), and basalts collected along segments H-J2 (Figure 3.4) show

elevated 3He/4He ratios consistent with material input from a mantle plume (Graham et al., 1999).

3.2 Data and Methods

3.2.1 Bathymetric Data and Axis Identification

This study utilizes hull-mounted multibeam bathymetry collected along the SEIR (Cochran et al., 1997; Sempéré et al., 1997, Scheirer et al., 1998 and Graham et al., 1999), JdFR (EEZ-SCAN 84 Scientific Staff, 1985, 1986; Hooft and Detrick, 1995; Canales et al., 2005; Carbotte et al., 2008), and GSC (Searle and Hey, 1983; Hey et al., 1986; Kleinrock and Hey,1989a, b; Kleinrock et al., 1989; Hey et al., 1992; Perram and Macdonald, 1994; Canales et al., 1997; Sinton et al., 2003; Christie et al., 2005; White et al., 2008; Holden et al., 2011; Mittelstaedt et al., 2012). The Marine Geoscience Data System (MGDS) compiled data for the SEIR and JdFR gridded at 110 m (Ryan et al., 2009). Data along the GSC were compiled by Dennis et al. (2012) and gridded at 50 m.

The position of the ridge axis along the SEIR and GSC is obtained from Supak et al. (2007); however, the trace of the GSC axis has been updated and expanded to take advantage of newly acquired multi-beam bathymetry (Dennis et al., 2011). The JdFR ridge axis is obtained from Carbotte et al. (2008). In all cases the ridge axis is defined by following the crest of volcanic ridges, volcanic constructs along the axial high or within the rifted axial high floor, or the approximate midpoint between the innermost pair of graben faults (Supak et al. 2007).

3.2.2 Volcano Identification

Volcanoes were identified and isolated using the Modified Basal Outlining Algorithm (MBOA) (Bohnenstiehl et al., 2012). The MBOA identifies volcanic edifices

as quasi-cone-shaped topographic highs. The initial detection utilizes a closed-contouring algorithm operating on the gridded bathymetry (e.g., Behn et al., 2004; Bohnenstiehl et al., 2008). MBOA then adjusts the elevation of the volcanic base downslope until a suite of morphometric parameters is met (Bohnenstiehl et al., 2012). The result is a set of volcanic edifices defined by variable-elevation basal polygons. Howell et al. (2012) evaluated the efficacy of MBOA by applying it to Springerville Volcanic Field, Arizona where MBOA performed well in identifying the cones mapped using traditional ground-based geological methods by Condit (2010), with only a 4% difference in the estimates of height and area and a 14% difference in total volume of cones within the volcanic field.

Using an automated method like MBOA to pick volcanoes limits subjectivity in their selection; however, some parameters controlling volcano selection, such as eccentricity and shape criteria, must be set by the user. In this study, the initial selection of topographic highs identified as volcanoes uses a contour search interval of 10 m, and requires long-to-short axis ratios ≤ 2 and an elliptical misfit parameter ≤ 0.4 (cf. Bohnenstiehl et al., 2012). These values are consistent with criteria from previous studies using automated methods of volcano identification (Behn et al., 2004; Bohnenstiehl et al., 2008; Cochran, 2008; Howell et al., 2012).

MBOA fits a three-dimensional surface to the polygonal base outlining each edifice (Bohnenstiehl et al., 2012). Volcano height is determined as the maximum distance between this basal polygon and the volcano surface. The planimetric area of the base and the volume of the volcano are determined by integrating over the closed polygon base and from the base to the three-dimensional surface of the edifice,

respectively. However, because the basal outline of an edifice is typically irregular, the reported radius is that of an equivalent-area circle. Height, area, volume and plan-view centroid for each volcano are exported by the MBOA. We eliminate volcanoes with heights < 30 m prior to any statistical analysis; features smaller than this are only resolvable in the 50 m GSC multi-beam.

3.2.3 Segment-Scale Seamount Population Statistics

Trends in the size and spatial distribution of volcanoes among and within ISRs are examined. We represent volcano size as the total eruptive volume. The centroid of each edifice is projected along the relative spreading direction back onto the axial trace, and this location is then used to define a volcano's position relative to the segment boundaries.

The spatial distribution of volcanoes is investigated on a segment scale by converting its distance from the western (or northern) segment end into a phase angle by dividing by the total segment length and then multiplying by 360, which represents its non-dimensional position in degrees. For east-west (or north-south) trending ridge segments, a seamount at the western (or northern) tip of a segment is assigned a phase of 0°, one located in the exact center of a segment is assigned a phase of 180°, and one at the eastern (or southern) end of a segment is assigned a phase of 360°. A rose-diagram therefore displays the seamounts located near the segment ends in its northern hemisphere and those near the segment center in its southern hemisphere. Seamount phase angles are then stacked among segments based on axial morphology, the presence or absence of an on-axis melt lens, and whether or not there is geochemical evidence for the input of melt from a hotspot or magmatic anomaly.

We divide each ridge segment into a central and end region for simplicity. We define each segment end as 25% of the total segment length, so that seamounts formed at phase angle of 0-90° and 270-360° are located at segment ends, and those from 90-270° are located within the center. To quantify the abundance of seamounts at the segment ends relative to the segment centers, the percent excess (Nex) is defined as (Cochran et al., 2004; Stroup et al., 2007):

$$N_{ex} = 100 * \frac{k - \frac{n}{2}}{\frac{n}{2}}$$

where k is the number of seamounts with phase angle of 0±90° (segment ends) and n is the total number of seamounts along a segment. If there is a uniform seamount distribution between segment center and end, the percent excess is zero; positive values indicate more seamounts at the segment ends, and negative values indicate more in the segment centers.

To evaluate the significance of the Nex values, a binomial model is used. For n seamounts along a segment, the probability of observing k or more seamounts at the segment ends can be expressed as: $p(\geq k, n) = 1-\beta(k-1, n, 0.5)$, where β represents the binomial cumulative distribution function evaluated for k successes out of n total trials, and 0.5 is the probability of any randomly positioned seamount being located near the segment end (e.g., Trauth, 2010). When $p(\geq k, n)$ is small (e.g., < 0.05), there is significant tendency for seamounts to form near the segment ends. Conversely, if $p(\geq k, n)$ is large (e.g., > 0.95), there is significant tendency for seamounts to form at the segment centers, relative to the ends. We interpret $0.05<p<0.95$ as indicating no significant patterns in seamount formation within a segment.

3.3 Results

Because the ISRs in this study have different spreading rates, a crustal age limit is used to limit our study area to those seamounts we consider to be actively forming. Using the crustal age for the seamount centroid, we find the age versus abundance comparisons for the JdFR and SEIR show no systematic pattern of increasing abundance through time (Figure 3.5). We therefore define the analysis window to consider only seamounts with centroids located on < 0.18 Ma ocean crust, which corresponds to the minimum width of contiguous swath bathymetry available along sections of the GSC—where coverage is the most limited. This width is in approximate agreement with the estimated (<0.2 Ma) temporal window over which small, isolated volcanoes have been observed to form at fast-spreading ridges (White et al., 1998).

3.3.1 JdFR Results

Along the Southern Explorer segment of the Explorer Ridge, seamount abundance and volume are low across the transition from axial high in the north to rifted axial high (49°45'N) but elevated at the transition from rifted axial high to axial valley (49°30'N) (Figure 3.6). Lavas from the rifted axial high are enriched by a long-lived mantle source, thought to generate an increased magma supply (Michael et al., 1989).

Across the Sovanco Fracture Zone to the JdFR, axial morphology is dominated by a rifted axial high, with the exception of axial valley segment West Valley (Figure 3.6). Carbotte et al. (2008) find a melt lens beneath all rifted axial high segments along this portion of the JdFR. Seamount abundance is relatively low along the thickly sediment covered West Valley segment, although where the Heck seamount chain intersects the ridge axis, there is a maximum in volume (Figure 3.6). Seamount abundance and volume

are relatively flat along the overlap of Endeavour with West Valley, although south of the intersection of the Heckle seamount chain with Endeavour segment, seamount abundance and volume increase approaching the southern end of the segment. Seamount abundance and volume remain elevated across the overlapping spreading center to Northern Symmetric segment, along the length of Northern Symmetric and approaching the offset with CoAxial (Figure 3.6). Split or Surveyor Seamount creates the local maximum in total volume at the north end of Northern Symmetric.

Across the overlapping spreading center to CoAxial segment, abundance and volume decrease with a shoaling of seafloor depth and the magma lens approaching Axial Seamount (Carbotte et al., 2008). At the overlap of Axial segment with CoAxial, abundance and volume are low but increase rapidly along the southern half of Axial segment. Axial Seamount was not included in this study because its base is wider than the crustal age window; therefore, the few volcanoes identified on top are parasitic cones and not representative of the total volume of Axial Seamount. The style of segmentation changes from overlapping spreading centers to non-transform offsets at the Axial/Vance offset. Seamount abundance and volume decrease from north-to-south along Vance and are lowest along Cleft (Figure 3.6), where the shallowest (2055±70 mbsf) and most uniform-depth melt lens has been imaged (Carbotte et al., 2008).

Across the Blanco Fracture Zone to the axial valley Gorda Ridge, abundance and volume of near axis seamounts along North Gorda increases (Figure 3.7). Abundance and volume reach a local maximum at the northern end of Jackson Segment but decrease toward the southern segment end. Seamount abundance and volume are relatively uniform across Central Segment, but reach a regional maximum within the Phoenix.

Spreading rate decreases to 22 mm/yr (Chadwick et al., 1998) at Escanaba Segment, where thickening sediment cover likely contributes to the small number of volcanoes reported (Figure 3.7).

Aggregating the data based on axial morphology reveals no significant preference for seamount formation at the ends of rifted axial high segments (Figure 3.8a), all of which are underlain by detectable melt lenses. For axial valley segments, there is a significant clustering of seamounts along the segment centers (Figure 3.8b). Along the lone transitional segment more seamounts are observed near segment center (Figure 3.8c).

Hotspot and melt anomaly influenced segments (Explorer, Endeavour, Axial) along the JdFR are observed to have more seamounts at the segment ends, but the binomial test indicates no significant preference for seamount formation along segment (Figure 3.9a). Non-hotspot influenced segments (West Valley, Northern Symmetric, CoAxial, Vance, Cleft, North Gorda, Jackson, Central, Phoenix, Escanaba), however, show a significant tendency for seamounts to cluster at the centers of these segments (Figure 3.9b).

3.3.2 GSC Results

The western GSC segments W-GSC3 and W-GSC4 (97°45'W to 95°30'W) exhibit axial valley morphology and fairly uniform seamount abundances, although volume distribution is more variable, with a local high within W-GSC4 near 97°20'W and W-GSC3 volume skewed to the west (Figure 3.10). Transitions in axial morphology occur along segments W-GSC2 and W-GSC1, with a change from axial valley to rifted axial high near 94°15'W, and a change from rifted axial high to axial high near 92°42'W.

Transitions in axial morphology are accompanied with a shoaling of axial depth and melt lens (Detrick et al., 2002), and a thickening of the crust (Canales et al., 2002). Both W-GSC2 and W-GSC1 have lavas influenced by the Galápagos hotspot (Detrick et al., 2002). Seamount abundance and volume are elevated over the axial valley section of W-GSC2 (95°30'W to 94°15'W) and decrease along the rifted axial high morphology (94°15'W to 92°42'W) approaching the axial high. Local peaks in abundance and volume occur at 92°15'W, 91°45'W, 91°15'W and 91°W, near the projection of the Wolf-Darwin Lineaments to the ridge axis (Figure 3.10).

Across the Galápagos Transform, axial morphology is an axial high along E-GSC1 with relatively few seamounts of small volumes (Figure 3.11), although the Los Huellos Calderas (90°36'W and 90°32'W) are not included in this study because their bases are larger than the age window (0.18 Myr). Morphology transitions to a rifted axial high along E-GSC2 and the largest abundances and volumes in this region occur along the eastward propagating eastern segment tip (Figure 3.11). Across the overlapping spreading center to the rifted axial high segment E-GSC3, abundance and volume are lower than observations from E-GSC2, but are locally elevated at segment ends. The E-GSC segments have lavas sourced in part from the GSC hotspot (Christie et al., 2005).

Aggregating the seamount distributions on the basis of morphology reveals seamounts formed along axial high (E-GSC1), axial valley (W-GSC4, W-GSC3, E-GSC4) and transitional (W-GSC2, W-GSC1, E-GSC2) segments do not preferentially form at segment end or center (Figure 3.12a, c, d). However, seamounts along rifted axial high segments (E-GSC3) are preferentially clustered at segment ends (Figure 3.12b). For segments underlain by a melt lens (W-GSC1 and W-GSC2), seamounts do

not preferentially form along the segment (Figure 3.13a); however, for segments not underlain by a melt lens (W-GSC3) seamounts are preferentially clustered at segment center (Figure 3.13b). Seamounts show no preferred location to form with respect to segmentation irrespective of hotspot influence (Figure 3.14).

3.2.3 SEIR Results

In the vicinity of the ASP between ~74-86°E, the abundance and volume of seamounts increases along segments G through J1 (Figure 3.15a). Geochemical evidence indicates that lavas erupted at segments H, I1, I2, J1 and J2 were derived partially from the ASP hotspot (Graham et al., 1999), whose present day center is proximal to segment J1 along the shallowest section of the SEIR ridge. Axial depth shoals along this section of the SEIR, and the morphology of the ridge axis changes from an axial valley (G, H, I1) to a rifted axial high (I2, J1). The abundance and volume of seamounts drop abruptly crossing the transform boundary between segment J1 and J2 (Figure 3.15). Along segment J2, the axial bathymetry plunges to the east away from the ASP hotspot, and the rifted axial high with few seamounts found in the west transitions to a relatively seamount-rich axial valley in the east. Seamount abundance and volume reach a local maximum near the center of segment J3 then decrease within rifted axial valley segments J4 and K (Figure 3.15a).

East of the ASP influenced region, axial morphology between ~86-100°E is highly variable. The morphology evolves from a rifted axial high along segment L to an axial high along segments M1a and M1b. Segment M2 is a transitional segment, with an axial high morphology in the west and rifted axial high in the east. A rifted axial high morphology persists along segments M3-O, with the exception of axial valley segment N

(Figure 3.16). Over this region, abundance and volume of seamounts are lower than near the ASP (Figure 3.15). Segment M2 exhibits an asymmetric abundance and volume, with the histogram skewed toward the eastern end of the segment (Figure 3.16).

Continuing to the east between ~100-116°E, axial morphology transitions from an axial high along P1 to rifted an axial high along P2 (Figure 3.17). Segment P3 has a transitional morphology, with an axial high in the west, a rifted axial high in the center, and an axial valley in the east. Axial valley morphology persists along segment P4 through T, with the exception of transitional segment R, which exhibits an axial high in the west and a rifted axial high in the east. Baran et al. (2005) observe a shallow (~1500 mbsf) melt lens beneath axial highs, deeper (~2100 mbsf) melt lenses beneath rifted axial highs, and no melt lens beneath axial valley segments. Seamount abundance and volume along segments P1-P3, R and S4 are asymmetric, with more seamounts with larger volumes forming at the eastern segment ends of P1-P2 and R, and more seamounts with larger volumes at the western segment end of S4 (Figure 3.17). Segments S1 and S3 have larger seamount abundances and volumes at both segment ends, relative to their centers (Figure 3.17).

Aggregating seamount distributions, all segment morphologies show a significantly higher abundance of seamounts at segment ends. This pattern is observed for segments that are not influenced by the ASP and whether or not a crust melt lens exists beneath the segment (Figures 3.18 and 3.19). Segments influenced by the ASP hotspot, however, do not show this pattern (Figure 3.20a).

3.3.4 Relationship between seamounts and axial morphology

Axial high segments form exclusively along hot-spot influenced sections of the GSC (Canales et al., 2002; Detrick et al., 2002; White et al., 2008), and the seamounts along these segments are not preferentially distributed between the segment ends and centers (Table 3.1). Along the SEIR, however, axial high morphologies are found exclusively outside the ASP zone of influence, and seamounts are strongly clustered at the ends of these segments. This may suggest two separate controls on axial morphology and seamount distribution along these ISRs.

Rifted axial highs are considered an ISR specific morphology by Cochran et al. (1997) and Baran et al. (2005) and are observed on all ISRs in this study. Rifted axial highs are associated with regions of thicker crust along the JdFR (Carbotte et al., 2008), hotspot influenced sections of the GSC (also with thicker crust), and may be found throughout the SEIR. Seamounts show no preference to form at either ends or centers of segments along the JdFR, but are strongly clustered at the ends of rifted axial high segments along the GSC and SEIR (Table 3.1).

The axial valley morphology is found away from the influence of melt anomalies and hotspots along the JdFR and GSC, but occurs throughout the SEIR. For axial valley segments, seamounts are strongly clustered at segment center along the JdFR, show no preference to form at either ends or centers of segments on the GSC, and are strongly clustered at the ends of segments along the SEIR (Table 3.1).

Transitional segments are observed along all ISRs and can be found along segments with or without hotspot influence (Figures 3.6, 3.10, 3.11 and 3.15). Seamount abundance and volume are always lower within the portion of the segment exhibiting an axial high morphology and higher along the portion with rifted axial high/axial valley

morphology. This creates an asymmetric distribution with the abundance of seamounts higher near one segment boundary than the other.

Seamounts are consistently more abundant along axial valley and transitional morphology segments than along axial high or rifted axial high segments (Table 2). Although the GSC has the greatest seamount abundance, it has the smallest average volumes of the ISRs, suggesting a pattern of many, small volcanoes. Total volume of seamounts per ridge length is similar for the ISRs and the greatest volumes are found along axial valley segments in the SEIR, transitional morphology in the JdFR and axial highs in the GSC.

3.4 Discussion

Previous studies along the GSC have shown seamount abundance and volume to decrease approaching the Galápagos Hotspot from the west (Behn et al., 2004; White et al., 2008). A decrease in seamounts and increase in fissure-fed volcanism is associated with an increase in volcanic effusion rates associated with a crustal magma lens (Behn et al., 2004). White et al. (2008) also note an increase in height and volume of the seamounts approaching the Galápagos Transform. Similarly, we observe the highest seamount volume per ridge length along axial high and rifted axial high morphologies on GSC (Table 3.2). Our results along the E-GSC (Figure 3.11), however, indicate seamount abundance and volume do not systematically vary to the east with distance from the hotspot. Moreover, along the SEIR and JdFR, seamounts are somewhat more abundant on the ASP along the SEIR and along the CoAxial and Axial Segments of the JdFR. Volume follows the same trend as seamount abundance for hotspot-influenced regions of JdFR and SEIR, indicating no change in the size of seamounts detected in this study (nb.

Axial Seamount is excluded). Why, then, does seamount abundance increase and volume remain constant along hotspot-influenced segments of the JdFR and SEIR? Crustal thickness does not show a large variation from north-to-south in the JdFR, although the melt lens shoals approaching Axial segment (Carbotte et al., 2008). Behn et al. (2004) dismiss depth to magma lens as a cause for decreasing seamount abundance approaching the Galápagos Hotspot because seamounts do not follow the abrupt change in melt lens depth, but gradually decrease in abundance. The opposite trend is found at the JdFR where seamount abundance increases as the melt lens shoals. Although along Cleft, where the magma lens is shallowest and most continuous (Carbotte, et al. 2008), the lowest seamount abundance and volumes are observed (Figure 3.6). We are unable to directly compare seamount abundance to magma lens depth and continuity for the ASP region of the SEIR because multi-channel seismic data do not exist.

White et al. (2002b) observe more volcanoes at the ends of segments along the fast spreading EPR, which they attribute to discontinuities in the crustal melt lens leading to lower effusion rate eruptions. This model predicts that more volcanoes should form where the melt lens is discontinuous. Seamounts along segments along the SEIR underlain with a melt lens follow this expected trend, with more seamounts forming at the end of segments. However, seamounts along segments underlain with a melt lens on the JdFR and GSC do not concentrate at segment ends.

Considering the seamount distributions of these ridges collectively (Table 3.1), there is a lack of clustering at segment ends along the GSC and JdFR regardless of axial morphology, hotspot influence or presence of melt lens. This distribution of seamounts is a characteristic similar to slow-spreading ridges (Smith and Cann 1990, 1992, 1993,

1999; Smith et al., 1995). Furthermore, if we consider CoAxial through Cleft to be influenced by the Cobb hotspot as suggested by Carbotte et al. (2008), the variable axial morphology and melt lenses associated with these ridges are only present when the ridge is influenced by a hotspot or melt anomaly. Away from the influence of the hotspot or melt anomaly, such as the North Gorda segment of the JdFR and west of W-GSC3, the only axial morphology is an axial valley.

Seamounts form in significantly greater abundance at segment ends of the SEIR regardless of axial morphology or melt lens presence, sharing characteristics associated with fast spreading ridges. Furthermore, SEIR axial morphology is variable outside of the influence from ASP or Kerguelen Hotspots at a nearly constant spreading rate. These results suggest that a change in the generation of oceanic crust occurs between 60 mm/yr (GSC) and 68 mm/yr (SEIR), consistent with other studies of gravity and bathymetry observations (Macdonald, 1982; Small and Sandwell, 1989) and numerical modeling (Phipps Morgan and Chen, 1993). Results from these studies indicate a change in axial morphology occurs when magma supply to the ridge becomes steady-state (Macdonald, 1982; Small and Sandwell, 1989; Phipps Morgan and Chen, 1993; Ito and Behn, 2008). Global observations of the bathymetry along MORs at fast, intermediate and slow rates (Carbotte et al., 2004; Supak et al., 2007) demonstrate that differences in axial depth across ridge offsets are correlated with the direction of ridge migration in the fixed hotspot reference frame. Carbotte et al. (2004) show that the shallower segment across an offset is usually the segment leading with respect to the direction of ridge migration (Carbotte et al., 2004; Katz et al., 2004; Supak et al., 2007). To generate a shallower segment across an offset, Katz et al. (2004) had to couple their asymmetric flow patterns

produced by ridge migration with a focusing of melt, suggesting that melt supply is enhanced to the leading segment end.

There are eight transitional segments in this study: the Southern Explorer Ridge in the JdFR (Figure 3.2), W-GSC2, W-GSC1 and E-GSC3 in the GSC (Figure 3), and J2, M2, P3 and R in the SEIR (Figure 3.4). Southern Explorer Ridge and J2 are influenced by a shallow melt anomaly or a hotspot, and have a rifted axial high on the trailing segment end that transitions to an axial valley along the leading segment end. Seamount abundance and volume are elevated along the leading segment end (Figures 3.6 and 3.15). Both segment ends along M2 also are considered leading, although axial morphology is expressed as a rifted axial high in the west and an axial valley in the east, where seamount abundance and volume are elevated (Figure 3.16). The leading segment ends of W-GSC1 and E-GSC2 are axial highs that transition to rifted axial highs along the trailing segment end with seamount-rich regions farther from the Galápagos hotspot (Figure 3.10). The western segment end of P3 is considered to be leading, and axial morphology is manifest as an axial high that transitions to a rifted axial high at segment center, and an axial valley at the eastern segment end. Seamount abundance and volume are elevated along the axial valley region of P3 (Figure 3.17), and Baran et al. (2005) observe a shallow crustal melt lens beneath the axial high that deepens beneath the rifted axial high, and eventually disappears beneath the axial valley. Segment R also is underlain by a melt lens along the axial high leading western segment end that disappears as seamount abundance increases and axial morphology transitions to axial valley (Baran et al., 2005) (Figure 3.17). Within transitional segments, the abundance and volume of seamounts are always lower along the axial highs, which are underlain by shallow melt

lenses (Detrick et al., 2002; Baran et al., 2005), and higher along the axial valley sections of the segment, which lack a crustal scale melt lens (Detrick et al., 2002; Baran et al., 2005). Based on the systematic transition in axial morphology, the observed melt lens beneath the axial high leading segment end, and the clustering of seamounts at the rifted axial high/axial valley segment end, it appears axial morphology along the SEIR is in part driven by ridge migration.

3.5 Conclusions

Among the ISRs, seamount production does not show a consistent pattern in response to the influence of near axis hotspots. Along the GSC, abundance and volume decrease approaching the Galápagos hotspot from the west (Figure 3.10) and do not systematically vary with distance from the hotspot to the east (Figure 3.11). Conversely, seamount abundance and volume increase regionally across the Amsterdam St. Paul plateau on the SEIR (Figure 3.15). They also are elevated along the CoAxial and Axial segments of the JdFR, which lie proximal to the Cobb hotspot (Figure 3.6).

The pattern of seamount formation within a segment and its correlation with axial morphology varies between the ISRs. Independent of axial morphology, seamounts along segments on the SEIR (68-76 mm/yr) cluster at segment ends. This distribution is consistent with that observed at along fast spreading axial high segments (White et al., 1998, 2000, 2002a, 2002b; Bohnenstiehl et al., 2008). The pattern, however, is not observed among segments influenced by the ASP. Although seamounts formed along rifted axial highs on the GSC (52-60 mm/yr) also show a preference for segment ends, seamounts within axial high and shallow axial valley segments are distributed roughly equally between segment end and center. On the JdFR, axial valley segments form

seamounts preferentially at their centers, whereas seamounts along rifted axial high segments show no preference in positioning. Axial valley segments on the JdFR include West Valley (56 mm/yr) and segments on the slow-to-intermediate spreading rate Gorda Ridge (22-56 mm/yr).

The along-axis seamount distribution is variably influenced by the presence or absence of a melt lens at the ISRs. Along the SEIR, the clustering of seamounts at the ends of segments is present regardless of whether or not a crustal melt lens (of sufficient size to be resolved using multi-channel seismic techniques) is present. Along the GSC, however, seamounts along segments with a crustal melt lens do not preferentially form at segment end. For GSC segments lacking a melt lens, seamounts show a significant clustering at segment center. Only the JdFR between the Sovanco and Blanco fracture zones, excluding West Valley, have been imaged seismically. Among these segments seamounts do not cluster at segment end.

Within transitional segments, the abundance and volume of seamounts are always lower along the axial highs, which are underlain by shallow melt lenses (Detrick et al., 2002; Baran et al., 2005), and higher along the axial valley sections of the segment, which lack a crustal scale melt lens (Detrick et al., 2002; Baran et al., 2005). For transitional segments with a hotspot or melt anomaly influence (Southern Explorer, W-GSC2, W-GSC1, E-GSC-2, J2 on the SEIR), these seamount rich valleys are positioned distal to the hotspot. Elsewhere along the SEIR, these seamount-rich valleys form either along the trailing segment end (P3), or if the segment is leading relative to both its neighbors, they are positioned along the end with the shorter offset (R, M2).

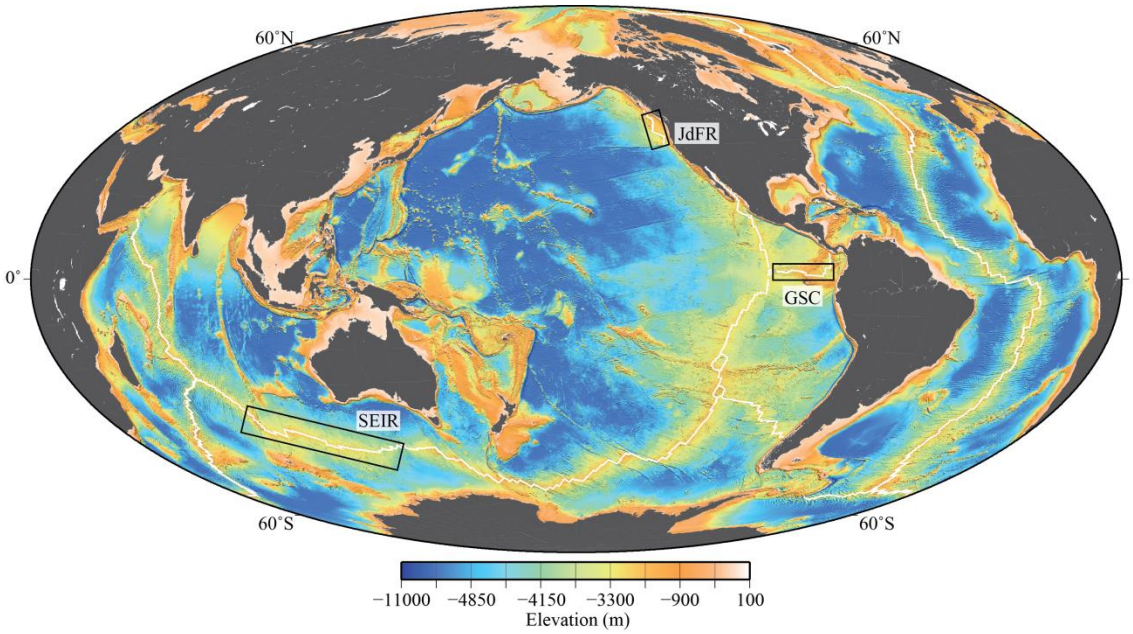

Figure 3.1. Global map of the MOR system (white line). Study areas are outlined with a black box. SEIR, Southeast Indian Ridge; JdFR, Juan de Fuca Ridge; GSC, Galápagos Spreading Centers.

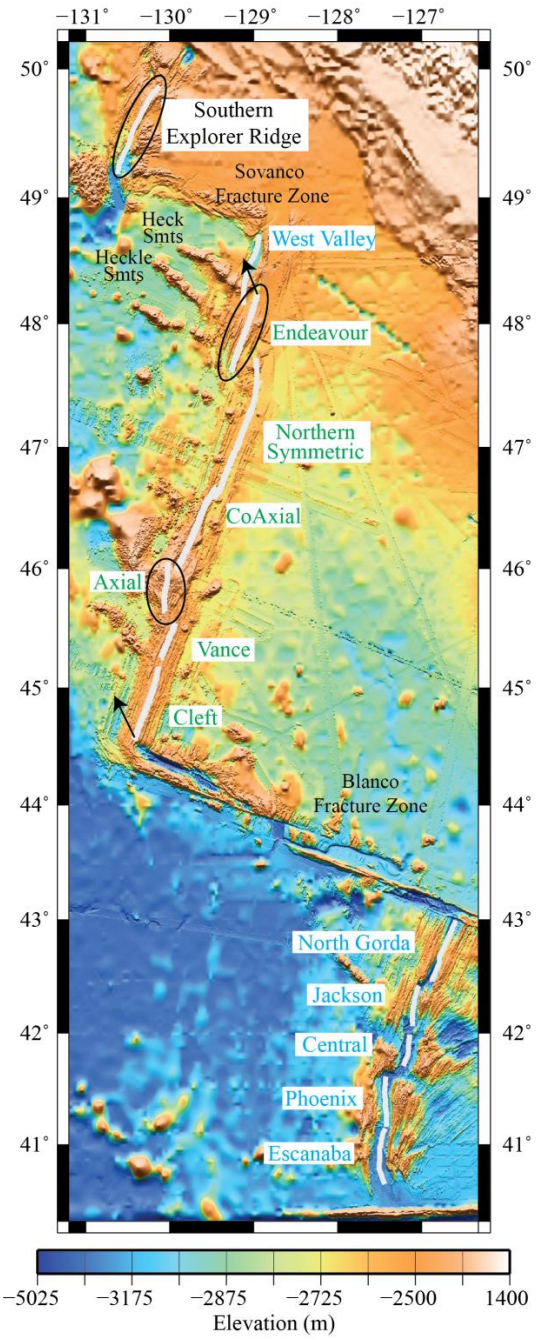

Figure 3.2. Regional bathymetric map of the Juan de Fuca Ridge. White line indicates the spreading axis (Carbotte et al., 2008), black ellipse indicates location and extent of melt anomalies and the Cobb Hotspot, segment labels indicate axial morphology (Rona et al., 1992; Chadwick et al., 1998). Green labels, rifted axial high morphology (Endeavour, Northern Symmetric, CoAxial, Axial, Vance, Cleft); black labels, transitional morphology (Southern Explorer Ridge); cyan labels, axial valley morphology (West Valley, North Gorda, Jackson, Central, Phoenix, Escanaba).

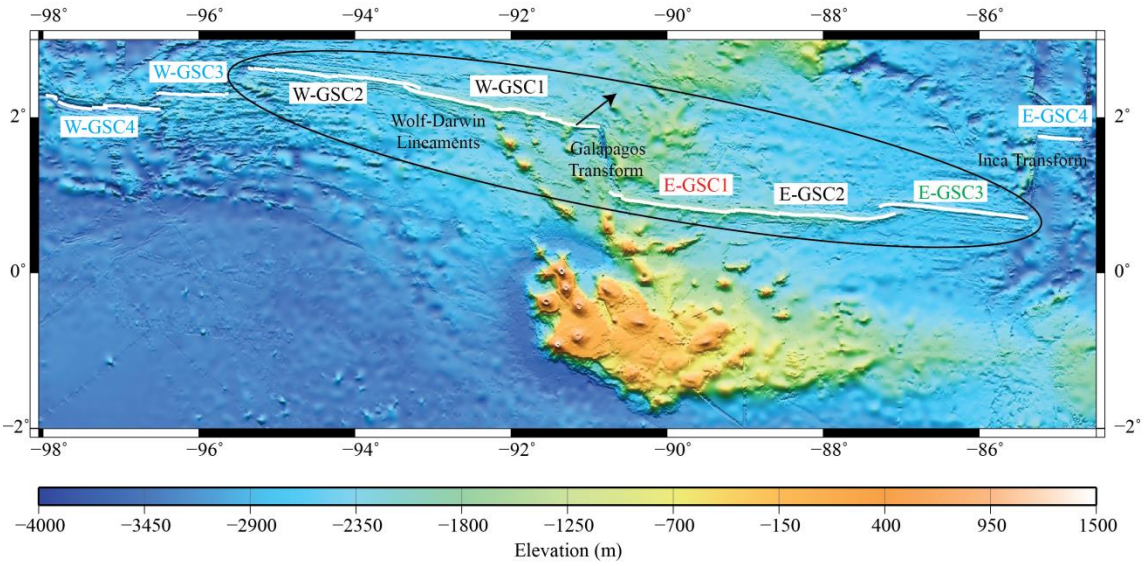

Figure 3.3. Regional bathymetric map of the Galapágos Spreading Centers. White line indicates the spreading axis (Supak et al., 2007), black ellipse indicates location and extent of the Galápagos Hotspot Swell, segment label color corresponds to axial morphology. Red labels, axial high (E-GSC1), green labels, rifted axial highs (E-GSC3); black labels, transitional (W-GSC2, W-GSC1, E-GSC2); cyan labels, axial valleys (W-GSC3, W-GSC4, E-GSC4).

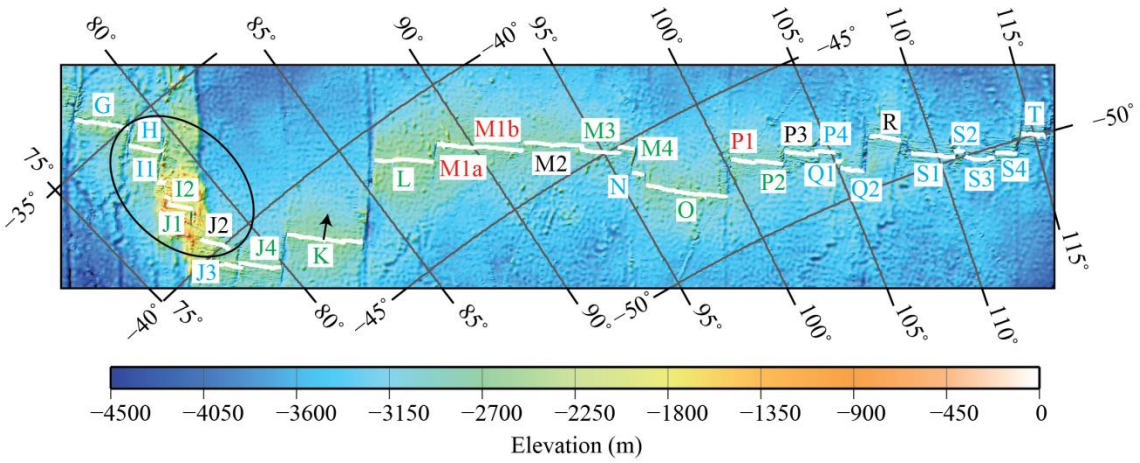

Figure 3.4. Regional bathymetric map of the Southeast Indian Ridge. White line indicates the spreading axis (Supak et al., 2007), black ellipse indicates location and extent of the Amsterdam/ St. Paul hotspot, segment names merge those introduced by Royer and Schlich (1988) and expanded by Cochran et al. (1997) and Graham et al. (1999), segment labels indicate axial morphology. Red labels, axial high morphology (M1a, M1b, P1); green labels, rifted axial high morphology (I2, J1, J4, K, L, M3, M4, P2); black labels, transitional morphology (J2, M2, P3, R); cyan labels, axial valley morphology (G, H, I1, N, P4, Q1, Q2, S1, S2, S3, S4, T).

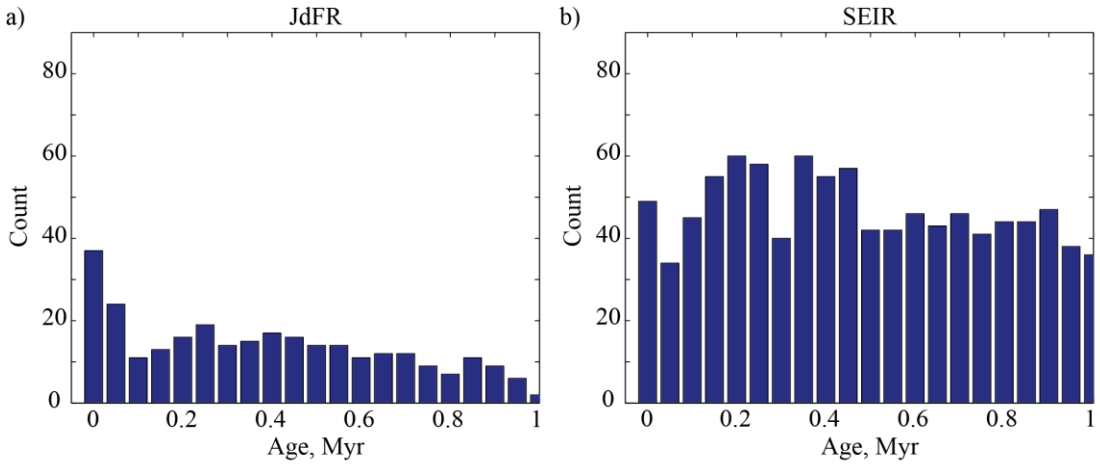

Figure 3.5. Age vs. abundance for a) JdFR and b) SEIR. Seamounts are limited to an age window of 0.18 Myr, the minimum width of available swath bathymetry along the GSC.

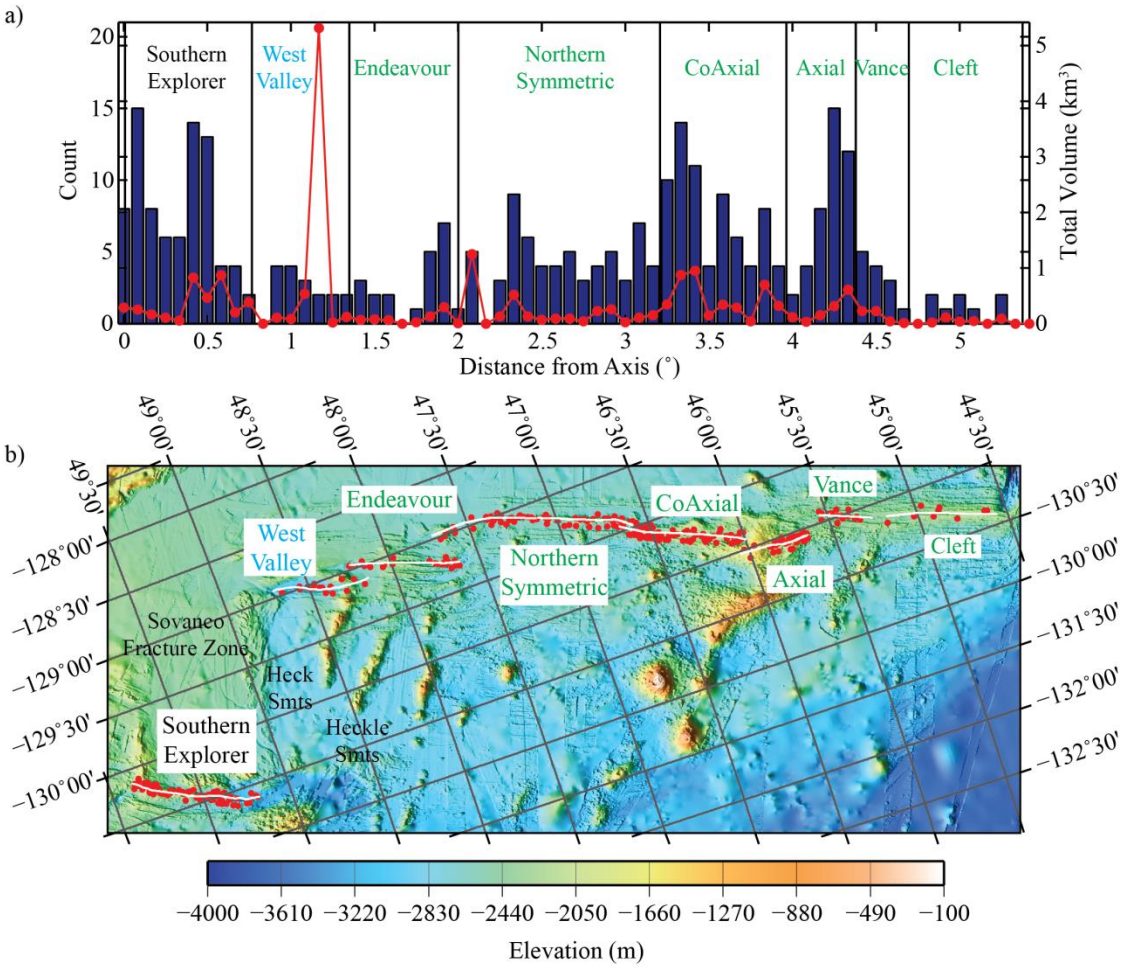

Figure 3.6. a) abundance (bars), volume (red line) and offset in segmentation (black lines) and b) bathymetry and seamount centroids (red dots) for the Southern Explorer and JdFR. Southern Explorer Ridge is influenced by an enriched mantle component (Michael et al., 1989), Endeavour is influenced by a shallow melt anomaly from the Heckle Seamounts (Carbotte et al., 2008), and Axial is influenced by the Cobb Hotspot (Chadwick et al., 2005). Green segment labels indicate rifted axial highs (Endeavour, Northern Symmetric, CoAxial, Axial, Vance, Cleft), cyan segment label indicates axial valley (West Valley) and black segment label indicates transitional (Southern Explorer).

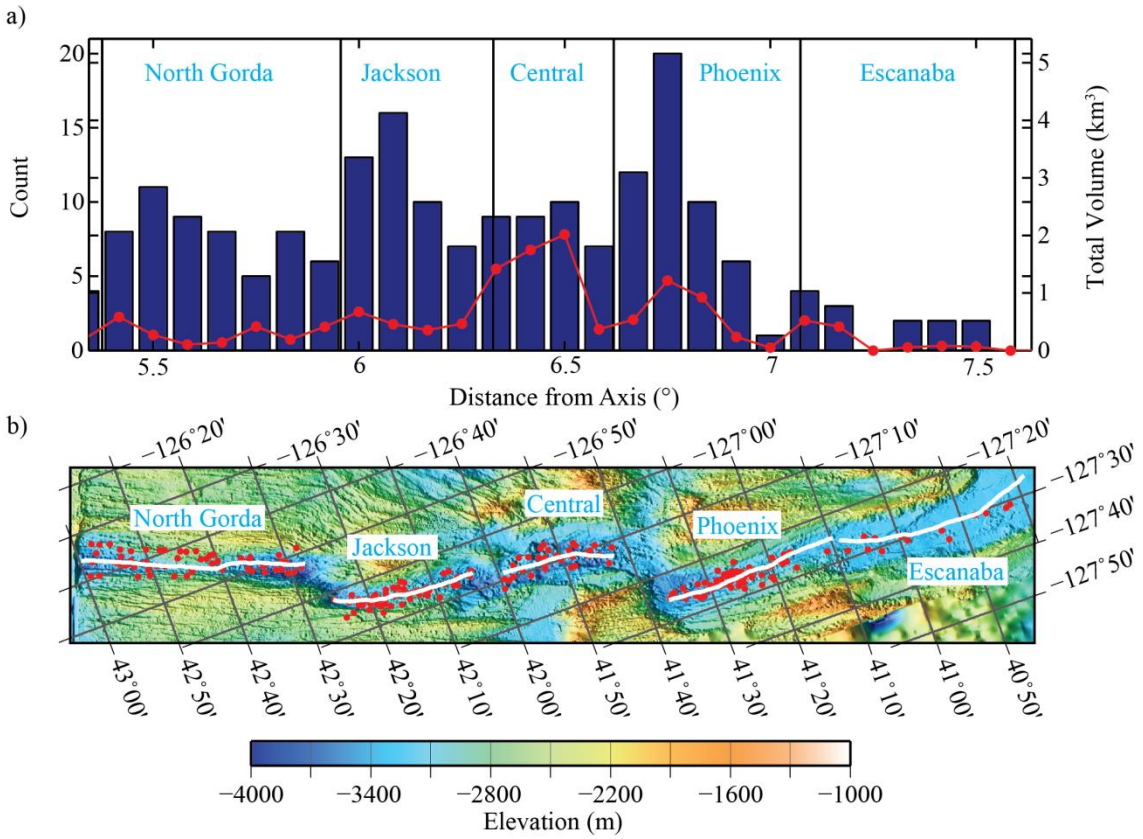

Figure 3.7. a) abundance (bars), volume (red line) and offset in segmentation (black lines) and b) bathymetry and seamount centroids (red dots) for segments along the Gorda Ridge. All segments have an axial valley (cyan segment label).

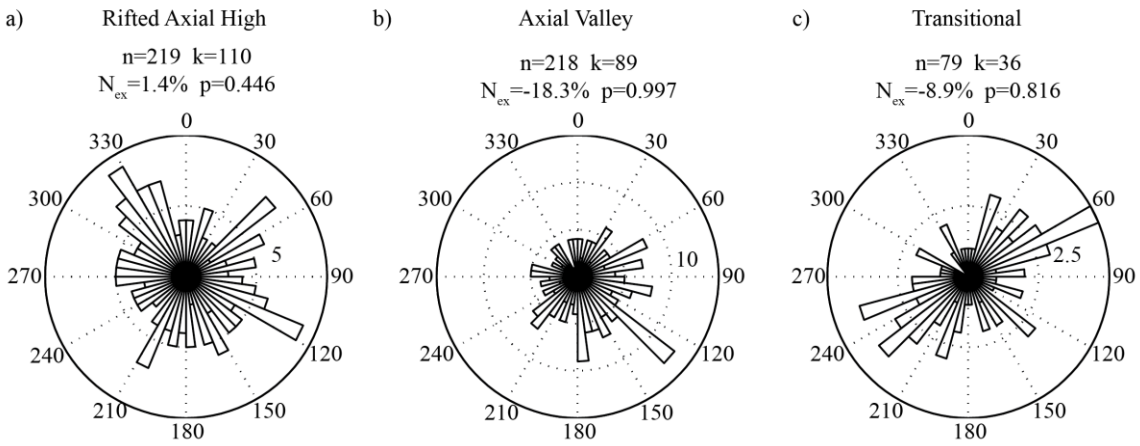

Figure 3.8. Rose diagrams for a) rifted axial highs, b) axial valleys and c) transitional axial morphologies along the JdFR. Axial high morphology is not observed along the JdFR. n indicates the number of seamounts with this morphology, k is the number of seamounts formed at segment end, N_{ex} is the percent excess, and p is the probability that >k seamounts form at segment end by chance.

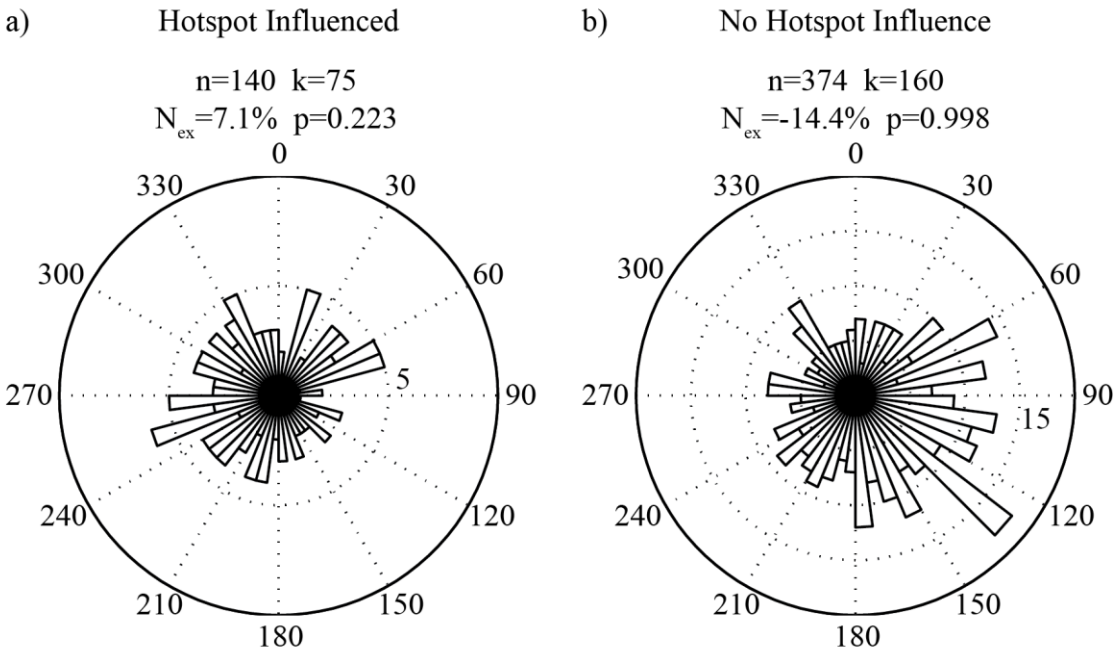

Figure 3.9. Rose diagrams of a) hotspot (Explorer Ridge, Endeavour, Axial) and b) non-hotspot influenced segments (West Valley, Northern Symmetric, CoAxial, Vance, Cleft, North Gorda, Jackson, Central, Phoenix, Escanaba) along the JdFR. See Figure 8 for description of variables.

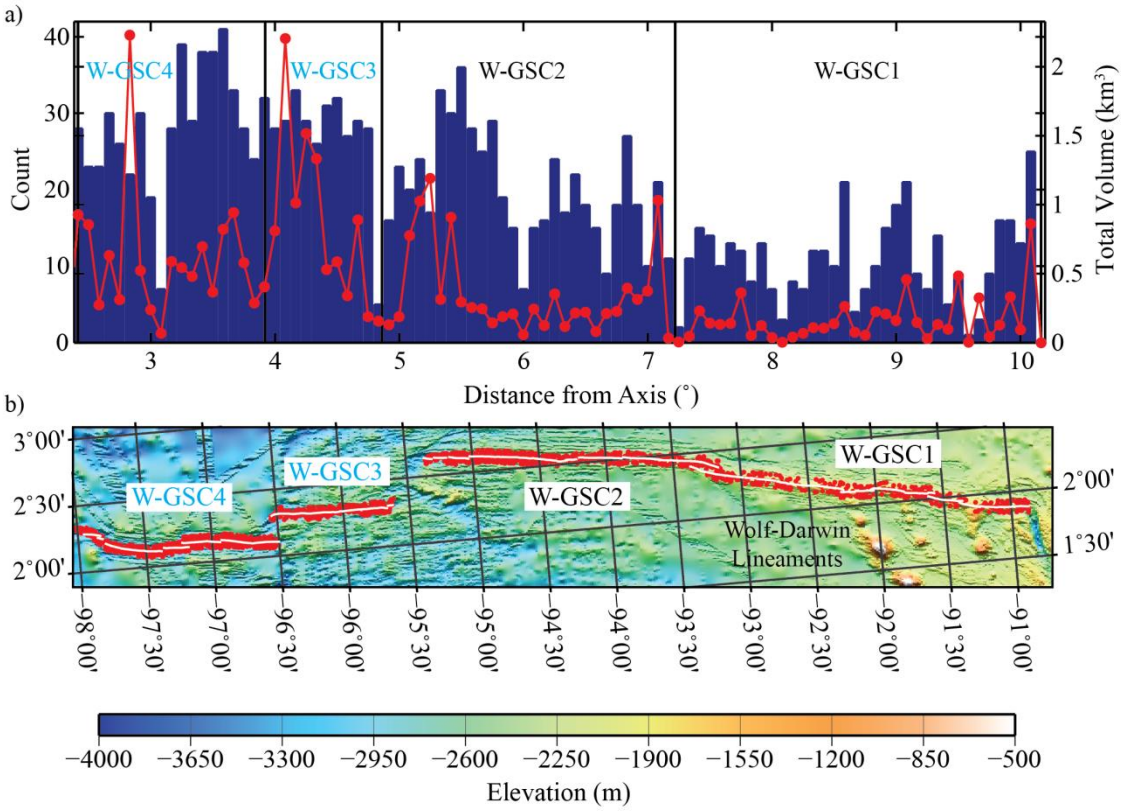

Figure 3.10. a) abundance (bars), volume (red line) and offset in segmentation (black lines) and b) bathymetry and seamount centroids (red dots) for the W-GSC. Cyan segment labels, axial valley (W-GSC3, W-GSC4); black segment labels, transitional (W-GSC1, W-GSC2). W-GSC2 and W-GSC1 are influenced by the Galápagos Hotspot.

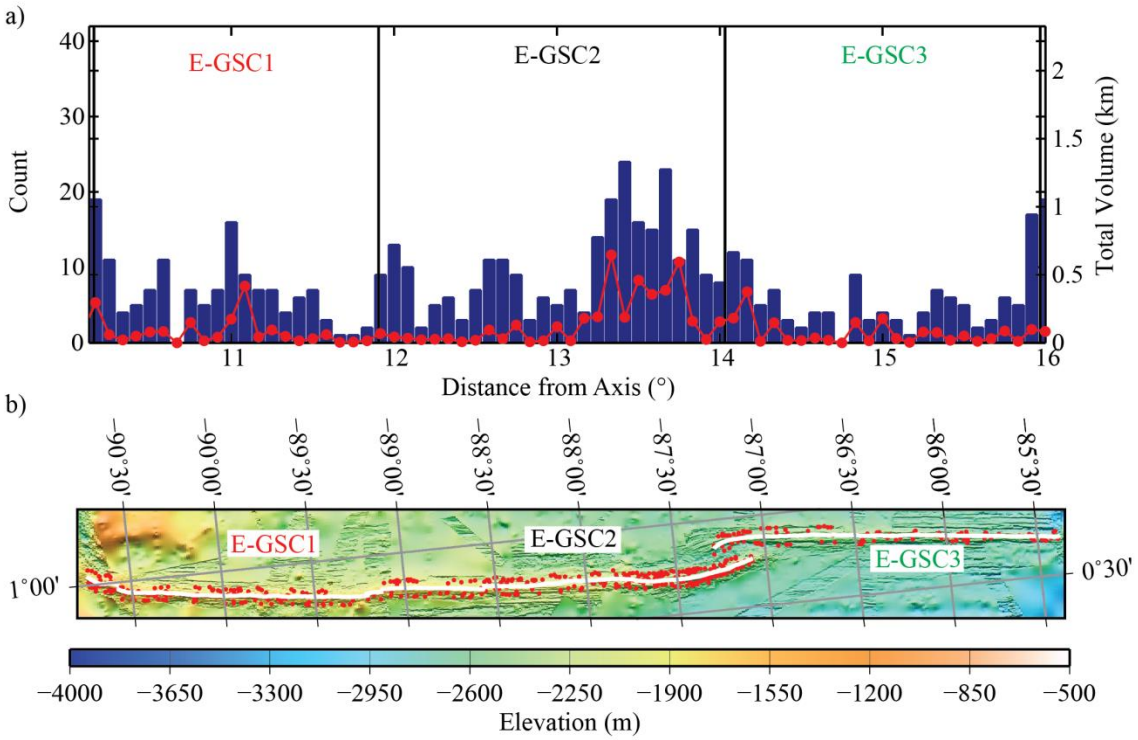

Figure 3.11. a) abundance (bars), volume (red line) and offset in segmentation (black lines) and b) bathymetry and seamount centroids (red dots) for E-GSC. Red segment labels indicate axial high (E-GSC1), green segment labels indicate rifted axial high (E-GSC3) and black segment labels indicate transitional axial morphology (E-GSC2). All segments are influenced by the Galápagos Hotspot Swell.

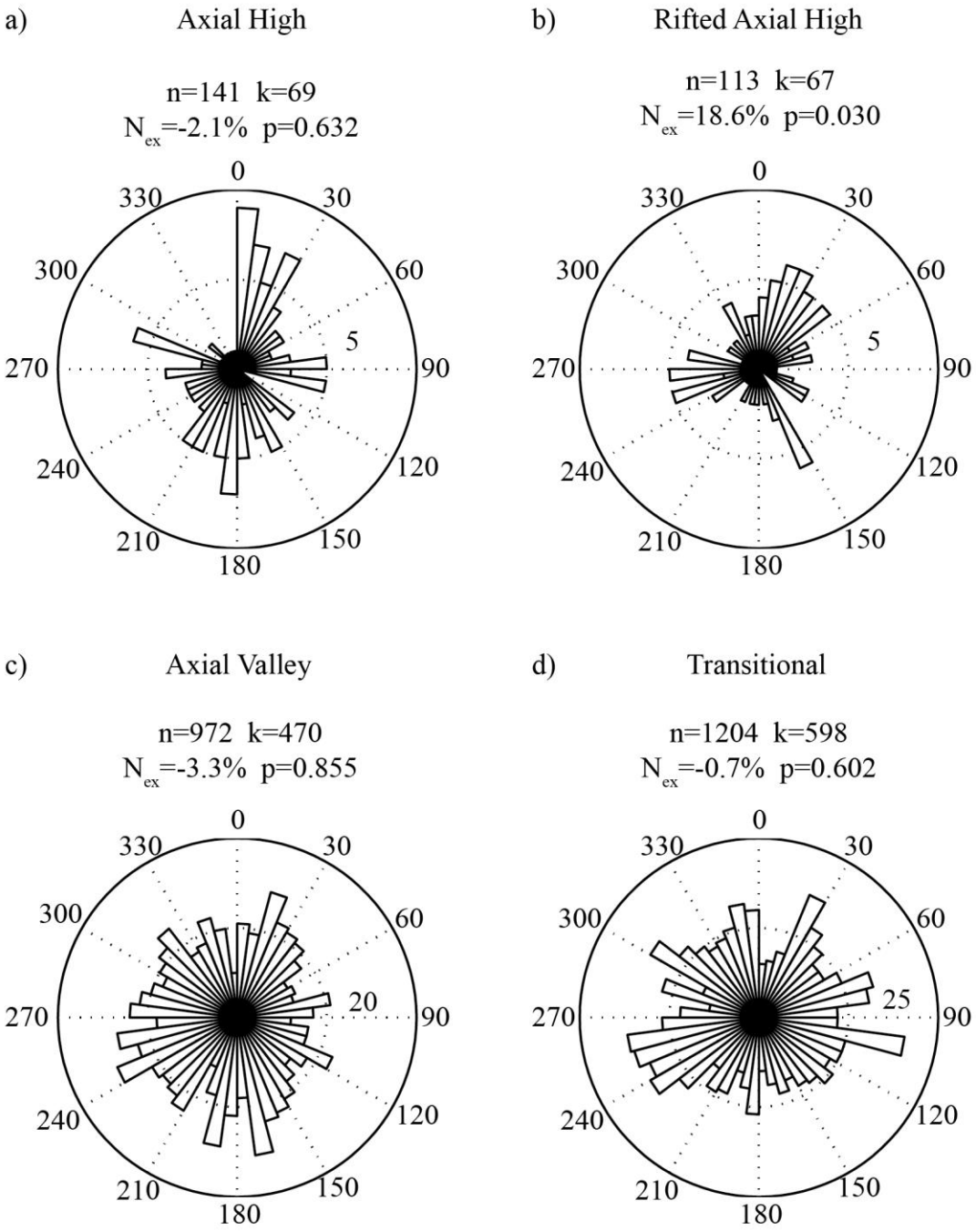

Figure 3.12. Rose diagrams for a) axial high, b) rifted axial highs, c) axial valleys and d) transitional axial morphologies along the GSC. n indicates the number of seamounts with this morphology, k is the number of seamounts formed at segment end, N_{ex} is the percent excess, and p is the probability that >k seamounts form at segment end by chance.

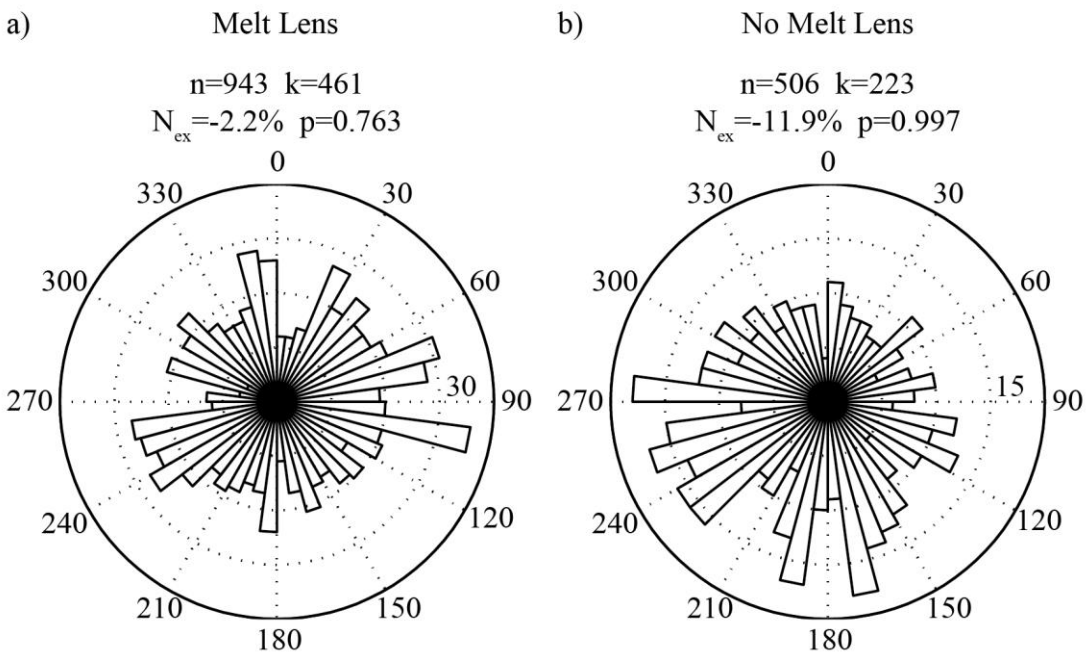

Figure 3.13. Rose diagrams for segments a) with (W-GSC1 and W-GSC2) and b) without (W-GSC3) a melt lens along the GSC. See Figure 12 for description of variables.

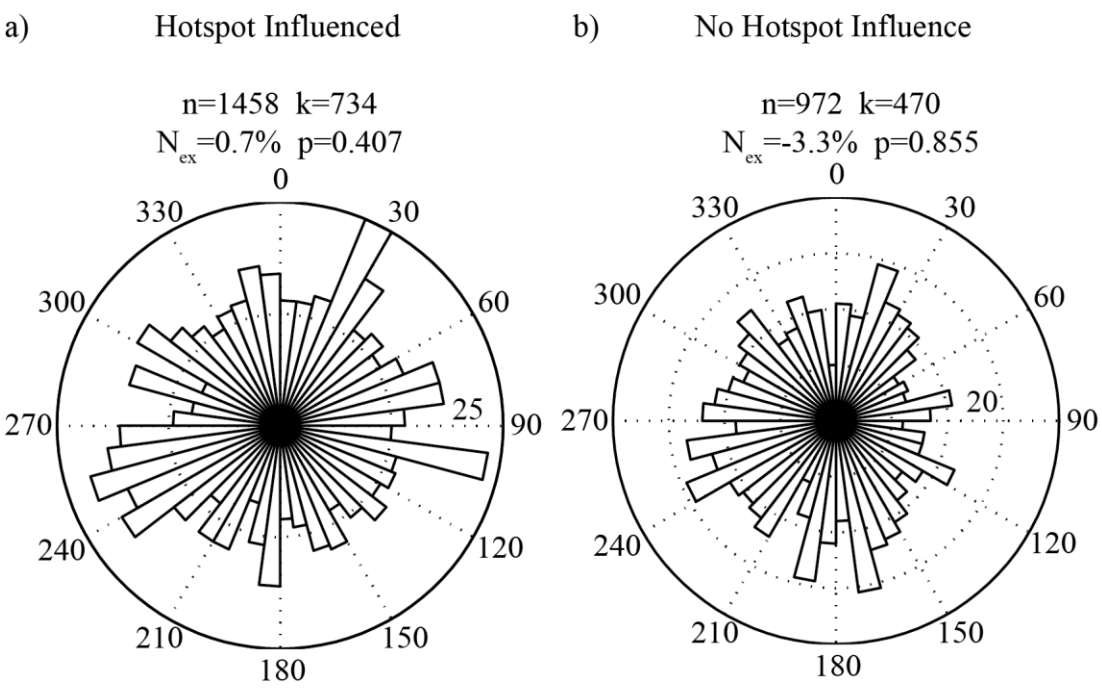

Figure 3.14. Rose diagrams of a) hotspot (W-GSC1, W-GSC2, E-GSC1, E-GSC2, E-GSC3) and b) no hotspot (W-GSC3, W-GSC4, E-GSC4) influence segments along the GSC. See Figure 12 for description of variables.

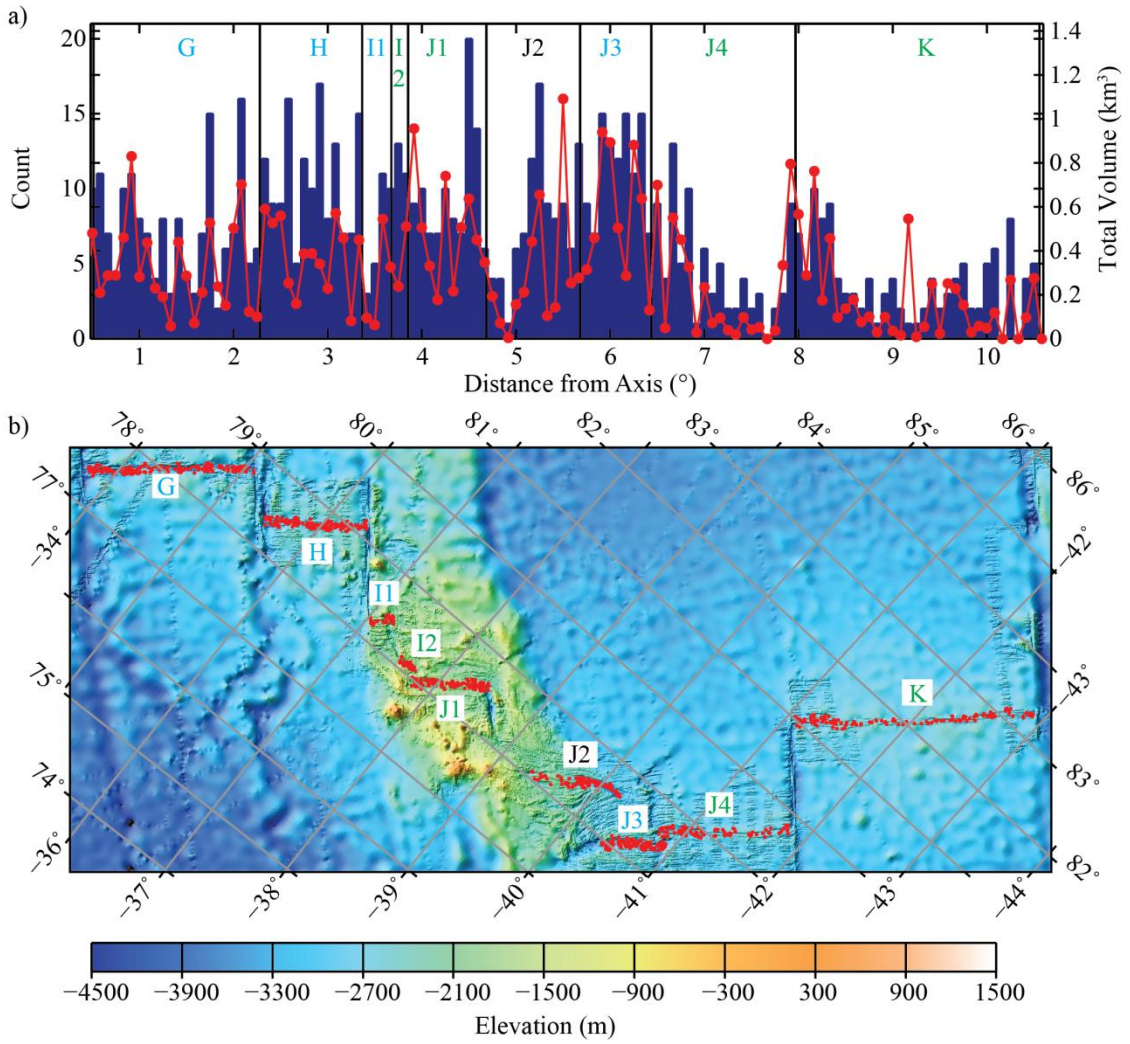

Figure 3.15. a) abundance (bars), volume (red line) and offset in segmentation (black lines) and b) bathymetry and seamount centroids (red dots) for segments G-K along the SEIR. Segments H, I1, I2, J1 and J2 are influenced by the Amsterdam/St. Paul hotspot. Green segment labels indicate rifted axial highs (I2, J1, J4, K), black segment labels indicate transitional axial morphology (J2), cyan segment labels indicate axial valleys (G, H, I1, J3).

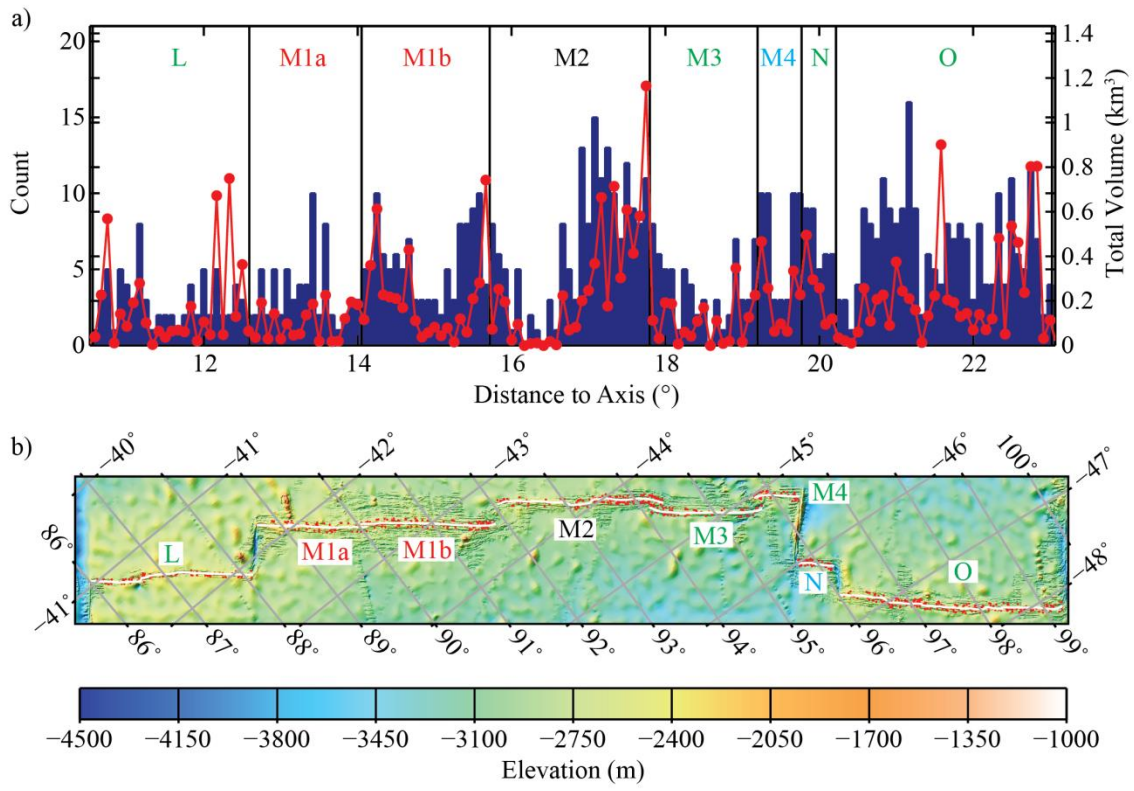

Figure 3.16. a) abundance (bars), volume (red line) and offset in segmentation (black lines) and b) bathymetry and seamount centroids (red dots) for segments L-O along the SEIR. Red segment labels indicate axial high (M1a, M1b), green segment labels indicate rifted axial highs (L, M3, M4, O), black segment labels indicate transitional axial morphology (M2), cyan segment labels indicate axial valleys (N).

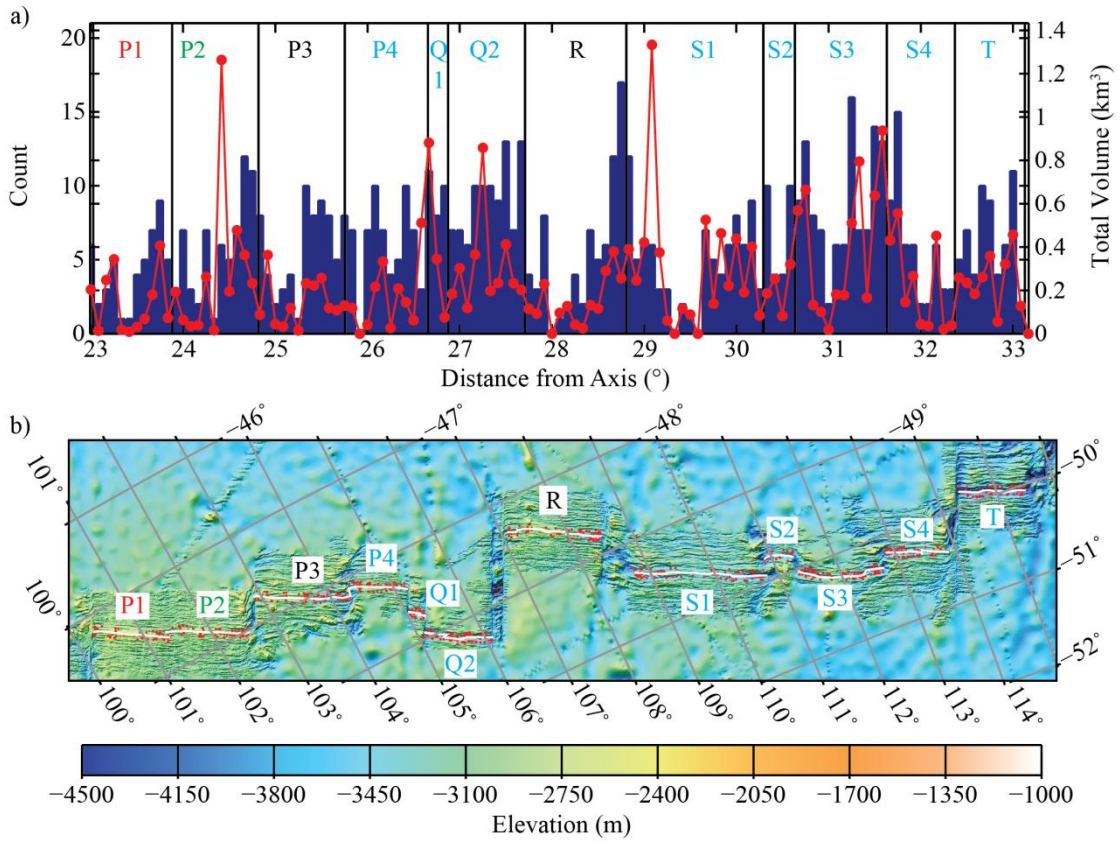

Figure 3.17. a) abundance (bars), volume (red line) and offset in segmentation (black lines) and b) bathymetry and seamount centroids (red dots) for segments P-T along the SEIR. Red segment labels indicate axial high (P1), green segment labels indicate rifted axial highs (P2), black segment labels indicate transitional axial morphology (P3, R), cyan segment labels indicate axial valleys (P4, Q1, Q2, S1, S2, S3, S4, T).

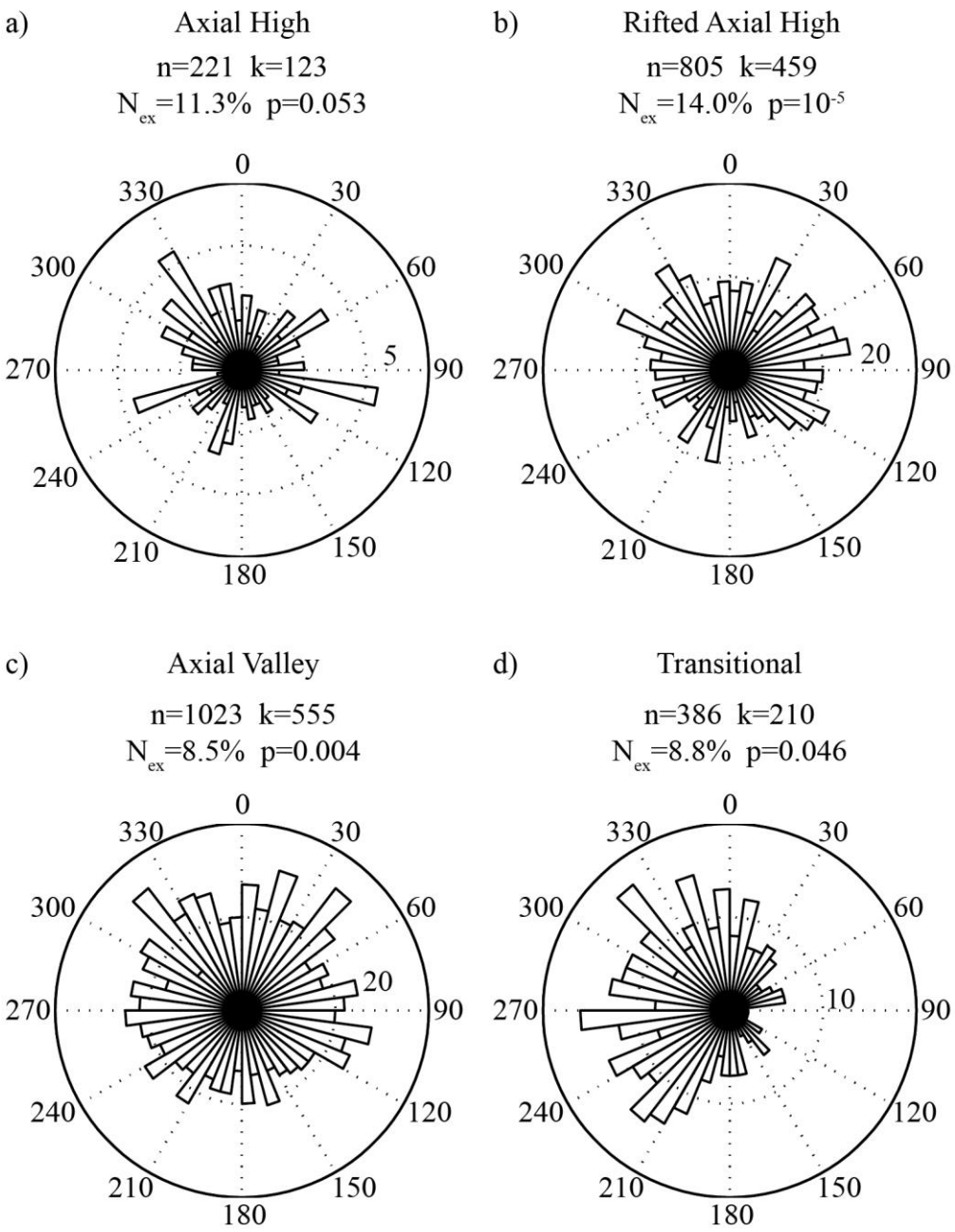

Figure 3.18. Rose diagrams for a) axial highs, b) rifted axial highs, c) axial valleys and d) transitional axial morphologies along the SEIR. n indicates the number of seamounts with this morphology, k is the number of seamounts formed at segment end, N_{ex} is the percent excess, and p is the probability that >k seamounts form at segment end by chance.

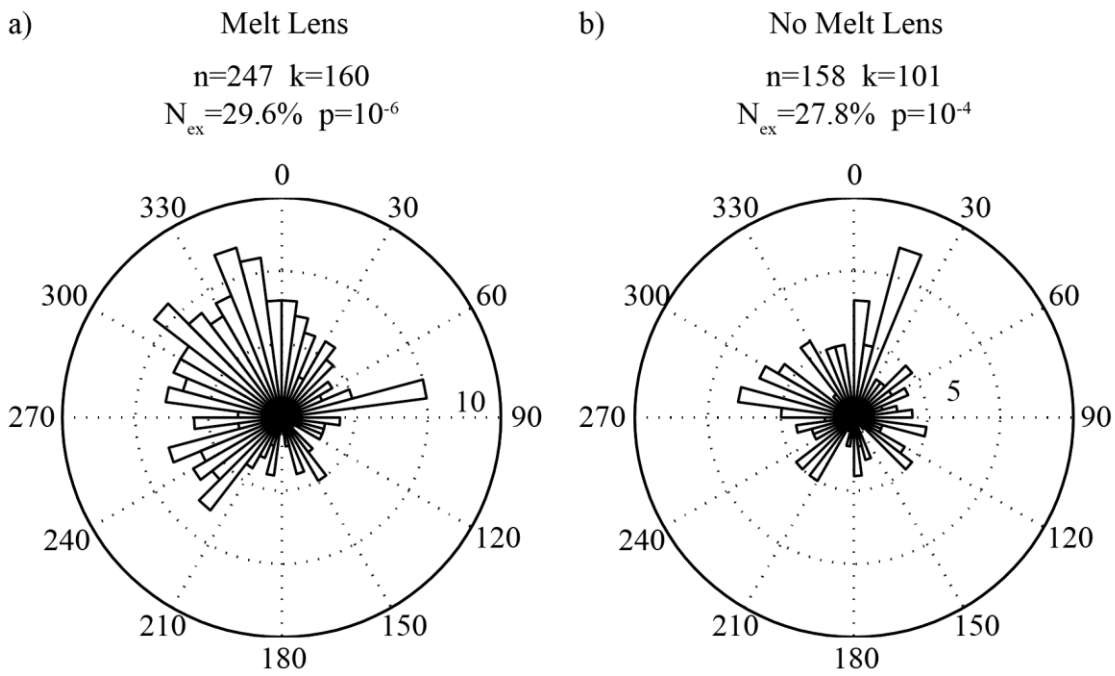

Figure 3.19. Rose diagrams for segments a) with and b) without a melt lens along the SEIR. See Figure 3.18 for description of variables.

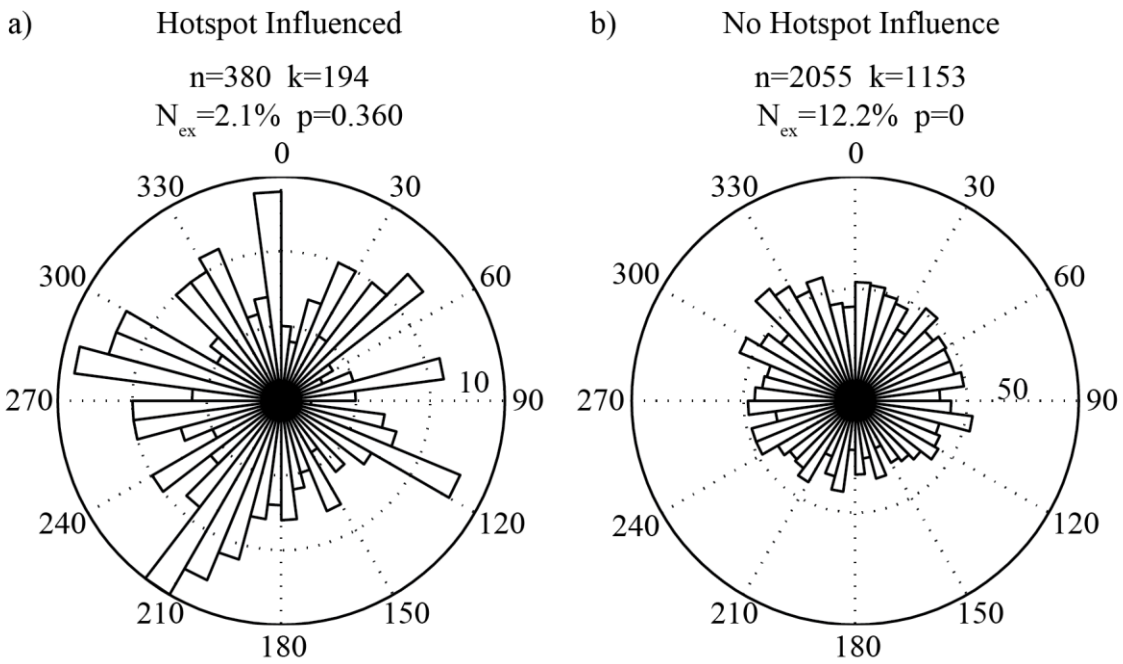

Figure 3.20. Rose diagrams of a) hotspot influenced (G-J2) and b) no hotspot influence (J3-T) segments along the SEIR. See Figure 18 for description of variables.

Table 3.1 Distribution of seamounts along segment

ISR	Axial High	Rifted Axial High	Axial Valley	Transitional	Melt Lens	Hotspot Influenced
JdFR	--	No Preference	Center	No Preference	No Preference	No Preference
GSC	No Preference	Ends	No Preference	No Preference	No Preference	No Preference
SEIR	Ends	Ends	Ends	Ends	Ends	No Preference

Table 3.2 Seamount statistics

JdFR	**Total**	**Axial High**	**Rifted Axial High**	**Axial Valley**	**Trans.**	**Melt Lens**	**Hotspot Influenced**
Abundance[a]	514 (0.61/km)	--	217 (0.49/km)	218 (0.713/km)	79 (0.94/km)	217 (0.4917/km)	140 (0.69/km)
Volume[b]	33.48 km^3 (0.04 km^3/km)		9.89 km^3 (0.08 km^3/km)	20.33 km^3 (0.11 km^3/km)	3.26 km^3 (0.40 km^3/km)	9.89 km^3 (0.08 km^3/km)	5.17 km^3 (0.17 km^3/km)
Average Volume[c]	0.0648 km^3 ±0.0103		0.0454 km^3 ±0.0063	0.0933 km^3 ±0.0238	0.0408 km^3 ±0.0104	0.0458 km^3 ±0.0063	0.0368 km^3 ±0.0061
GSC	**Total**	**Axial High**	**Rifted Axial High**	**Axial Valley**	**Trans.**	**Melt Lens**	**Hotspot Influenced**
Abundance[a]	2430 (1.66/km)	141 (0.77/km)	113 (0.53/km)	1809 (5.89/km)	1204 (1.58/km)	943 (1.7678/km)	1458 (1.26/km)
Volume[b]	45.73 km^3 (0.03 km^3/km)	1.75 km^3 (0.30 km^3/km)	1.56 km^3 (0.26 km^3/km)	32.46 km^3 (0.18 km^3/km)	19.63 km^3 (0.07 km^3/km)	15.69 km^3 (0.10 km^3/km)	22.93 km^3 (0.05 km^3/km)
Average Volume[c]	0.0188 km^3 ±0.0013	0.0124 km^3 ±0.0025	0.0139 km^3 ±0.0029	0.0179 km^3 ±0.0015	0.0163 km^3 ±0.0016	0.0167 km^3 ±0.0019	0.0157 km^3 ±0.0014
SEIR	**Total**	**Axial High**	**Rifted Axial High**	**Axial Valley**	**Trans.**	**Melt Lens**	**Hotspot Influenced**
Abundance[a]	2435 (0.66/km)	221 (0.51/km)	805 (0.58/km)	1023 (0.91/km)	386 (0.70/km)	247 (0.59/km)	580 (1.03/km)
Volume[b]	96.86 km^3 (0.03 km^3/km)	7.55 km^3 (0.02 km^3/km)	33.42 km^3 (0.02 km^3/km)	42.25 km^3 (0.04 km^3/km)	13.64 km^3 (0.02 km^3/km)	8.25 km^3 (0.02 km^3/km)	15.02 km^3 (0.04 km^3/km)
Average Volume[c]	0.0397 km^3 ±0.0014	0.0342 km^3 ±0.0043	0.0415 km^3 ±0.0029	0.0413 km^3 ±0.0022	0.0352 km^3 ±0.0033	0.0333 km^3 ±0.0049	0.0411 km^3 ±0.0028

[a] Abundance and abundance density in parentheses. Density is calculated by dividing the abundance by the segment length.
[b] Total volume and volume density in parentheses. Density is calculated by dividing the volume by the segment length.
[c] The sample mean ± standard error in the mean.

CHAPTER 4: VOLCANO FORMATION ALONG THE EASTERN LAU SPREADING CENTERS

The morphology of mid-ocean ridge (MOR) spreading centers is tied closely to the delivery of melt to the axis, with the processes of melt storage and the dynamics of eruptions manifested in the style of volcanism. Trends in the size and spatial distribution of volcanic constructs, from small (<20 m height) lava domes to large (< 750 m height) seamounts, have been used to infer the magmatic plumbing system required to build these features (e.g., Smith and Cann, 1990; 1992; White et al., 2000; 2002a; Bohnenstiehl et al., 2008). The size and spatial distribution of volcanoes also has been shown to systematically vary with tectonic segmentation (White et al., 2000; 2002a, b), spreading rate (Howell et al., submitted) and crustal thickness (e.g., Behn et al., 2004; White et al., 2008; Howell et al., submitted).

Fast spreading ridges (>90 mm/yr) exhibit spreading axis morphology of broad axial topographic highs segmented by transforms (offsets of 10's to 100's km) and overlapping spreading centers (offsets 1's to 10's km) (e.g., Macdonald et al., 1991). Volcanism is dominated by fissure-fed eruptions at the centers of these segments, with some very small central-vent volcanic edifices forming near the segment ends (White et al., 2000, 2002a, b; Bohnenstiehl et al., 2008). Slow spreading ridges (<40 mm/yr) are characterized by broad axial valleys segmented by transform faults (offsets 10's-100's km) and non-transform offsets (offsets <10 km) (e.g., Macdonald et al., 1991; Smith and Cann, 1993). The centers of slow-spreading ridge segments are typically shallower than

segment ends, with volcanism dominated by axial volcanic ridges and conical seamounts (Smith and Cann, 1990, 1992, 1993, 1999; Smith et al., 1995; Searle et al., 2010). The Eastern Lau Spreading Center (ELSC) in the Lau back-arc basin has characteristics of both fast and slow spreading ridges; however, these characteristics do not fit the expectations from previous studies.

Here, we analyze the size and spatial distribution of volcanoes 30 to 600 m tall along the Eastern Lau Spreading Centers (ELSC), a variable morphology and spreading rate back-arc ridge in the Lau Basin (Figure 4.1). Back arc spreading centers, such as the ELSC, are distinct from MORs in that back arc spreading centers are strongly influenced by a variable mantle temperature and chemical environment because of their proximity to a subduction zone (Dunn et al., 2013). Back arc spreading typically initiates near the arc volcanic front (Taylor and Karner, 1983) where crustal production at the spreading center is strongly influenced by subduction, especially the presence of slab-derived water (Dunn et al., 2013). With continued spreading, the ridge axes separate from the volcanic front, the subduction influence wanes, and crustal production becomes more MOR-like (Hawkins and Melchior, 1985; Pearce et al., 1995; Dunn et al., 2013).

4.1 Geologic Setting

The Eastern Lau Spreading Centers (ELSC) are located within the triangular-shaped Lau back arc basin (Figure 4.1), bordered on the west by the Lau Ridge remnant arc and to the east by the currently active Tofua arc (Karig, 1970; Hawkins, 1995; Dunn and Martinez, 2011; Dunn et al., 2013). The basin opening is thought to be a consequence of trench roll-back that began 6 Ma (Hawkins, 1994; Dunn et al., 2013). Around 4 Ma, the ELSC formed and propagated southward into existing back arc crust

toward the Tofua arc (Parson et al., 1990; Taylor et al., 1996; Dunn et al., 2013). As spreading continued, the volcanic arc front migrated eastward away from the spreading center (Dunn et al., 2013).

Axial morphology and spreading rate are variable within the ELSC. Spreading rate decreases from 96 mm/yr in the north to 39 mm/yr in the south, while axial morphology transitions from a shallow axial valley to a peaked axial high (Figure 4.2e). Using the segmentation classification of Macdonald et al. (1991), the ELSC is considered a single first-order segment consisting of 10 second-order segments (Figure 4.2e). The second-order segments are grouped into three distinct categories on the basis of spreading rate, crustal thickness and axial morphology: the North ELSC (N-ELSC), the Central ELSC (C-ELSC), and the Valu Fa Ridge (VFR).

The two second order segments of the N-ELSC are considered shallow axial valleys following the classification scheme of Baran et al. (2005), which defines a shallow axial valley as being characterized by a 5-15 km wide and 200-800 m deep valley. Spreading rate along the N-ELSC drops from 96 mm/yr in the north to 76 mm/yr approaching the C-ELSC (Martinez et al., 2006). Dunn and Martinez (2011) indicate that as the N-ELSC moved farther away from the Tofua Arc, spreading abruptly transitioned from thick to thin crust in response to decreasing subduction-derived water in the melting beneath the ridge (Dunn and Martinez 2011; Dunn et al. 2013). A single crustal thickness measurement along the extinct N-ELSC segments near 18°33´S indicates the crust is 5.5 km thick (Crawford et al., 2003).

Using a multichannel seismic array, Jacobs et al. (2007) did not image a continuous melt lens beneath the N-ELSC; however, they did image an isolated axial

magma chamber near 20°S. Tomographic studies of the N-ELSC by Dunn et al. (2013) indicate that a wide low velocity volume, which they consider to be indicative of a crustal magmatic system, underlies the N-ELSC. Dunn et al. (2013) suggest the wide crustal magmatic system may have formed in response to either faster spreading, less efficient hydrothermal removal of heat from the sides of the crustal magmatic system, or interplay between short-term melt supply and hydrothermal heat removal.

At the overlapping spreading center between the N-ELSC and C-ELSC, axial morphology is flat, with few faults and volcanoes. Away from the overlapping spreading center along the northernmost C-ELSC segment, the axis is characterized by a shallow rift 100 m deep and 1.6 km wide. The shape of the axis persists as axial depth decreases from -2520 m to -2200 m at the southern tip, characterizing this segment as a "transitional" axial morphology following Baran et al. (2005). Within this segment, magma composition abruptly changes from MORB-like to arc-like, lava vesicularity increases (Pearce et al., 1995), a continuous melt lens appears 2180 meters below seafloor (mbsf) (Jacobs et al., 2007) and the crustal magmatic system narrows (Dunn and Martinez, 2011; Dunn et al., 2013). The rifted axial high persists along the southern C-ELSC segment as spreading rate decreases to 61 mm/yr at the offset to the VFR (Figure 4.2d).

Spreading rate continues to decrease to 39 mm/yr at the southern end of the VFR (Martinez et al., 2006), axial morphology is characterized by a steep axial high, the axial magma chamber deepens to 2820 mbsf (Jacobs et al., 2007) and lava geochemistry transitions to more viscous, volatile-rich composition (Pearce et al., 1995). As the VFR propagates into the Havre Trough, segmentation is characterized by short (< 20 km) en

echelon axial volcanic ridges. Wiedicke and Collier (1993) suggest the "blade-like" cross-sectional shape of the VFR was formed by highly viscous magma solidifying and clogging potential fissures, causing the magma to reach the seafloor at localized points. A single crustal thickness measurement at 22°10´S of 9 km (Turner et al., 1999) indicates the crust in the VFR is considerably thicker than in the N-ELSC.

4.2 Methods

4.2.1 Bathymetric Data and Axis Identification

This study utilizes hull-mounted multibeam bathymetry collected along the ELSC (Wiedicke and Collier, 1993; Martinez and Taylor, 2002; Martinez et al., 2006) and gridded at 100 m. The position of the ridge axis along the ELSC is from Martinez et al. (2006) and follows the crest of volcanic ridges, volcanic constructs along the axial high or within the rifted axial high, or the approximate midpoint between the innermost pair of grabens.

4.2.2 Volcano Identification

We term quasi-circular volcanic features ranging in height from 30 to 600 m as volcanoes and identify these features using the Modified Basal Outlining Algorithm (MBOA) (Bohnenstiehl et al., 2012). The MBOA initially detects quasi-cone-shaped topographic highs by applying a closed-contour picking algorithm (e.g., Behn et al., 2004; Bohnenstiehl et al., 2008). MBOA then adjusts the elevation of the volcano base downslope until the criteria for a suite of morphometric parameters defining a probable volcano outline is met (Bohnenstiehl et al., 2012). The result is a set of perimeters of volcanic edifices defined by variable-elevation polygons. Howell et al. (2012) evaluated the efficacy of MBOA by applying it to Springerville Volcanic Field, Arizona where it

was able to closely match the results from traditional field geologic mapping (Condit ,2010), with only a 4% difference in the estimates of height and area and a 13% difference in total volume of cones within the volcanic field.

Using an automated method like MBOA to pick volcanoes limits subjectivity in their selection; however, choices for user-set parameters can influence volcano identification (Bohnenstiehl et al., 2012). In this study, the initial selection of volcanoes uses a 10 m contour interval, a long-to-short axis ratio of ≤ 2 and an elliptical misfit parameter ≤ 0.4, consistent with previous studies (e.g. Behn et al., 2004; Bohnenstiehl et al., 2008; Cochran, 2008; Howell et al., 2012; Howell et al., submitted).
MBOA fits a three-dimensional surface to the polygonal base outlining each edifice (Bohnenstiehl et al., 2012). Volcano height is determined as the maximum distance between this basal polygon and the volcano surface. The planimetric area of the base and the volume of the volcano are determined by integrating over the closed polygon base and from the base to the three-dimensional surface of the edifice, respectively. However, because the basal outline of an edifice is typically irregular, the reported radius is that of an equivalent-area circle. Height, area, volume and plan-view centroid for each volcano are exported by the MBOA.

4.2.3 Segment-Scale Volcano Population Statistics

Trends in the volume and spatial distribution of volcanoes are examined based on the position of a volcano along the ELSC and within individual ridge segments. The position of a volcano within a segment is determined by projecting the volcano centroid to the axial trace along the relative spreading direction. The distance from the northern

segment end to the volcano's projected position is tabulated and normalized by total segment length.

Following the analysis of lava domes on the East Pacific Rise by White et al. (2000, 2002a) and Bohnenstiehl et al. (2008) where each segment end represents 20% of the total segment length (40% combined), we define each segment end to represent 25% of the total segment length. Normalized volcano distance is multiplied by 360 to enable angle histogram plotting; volcanoes with normalized distance angles between 0-90° and 270-360° form at segment ends and therefore plot in the northern hemisphere of a rose-diagram. Volcanoes with normalized distance angles between 90-270°, representing segment center, plot in the southern hemisphere of the rose-diagram.

To quantify the abundance of volcanoes at the segment ends relative to the segment centers, the percent excess (Nex) is defined as: $N\_ex = ((k-n/2)/(n/2)) \times 100$, where k is the number of volcanoes at 0±90° (segment ends) and n is the total number of volcanoes per segment (Cochran et al., 2004; Stroup et al., 2007). If there is a uniform volcano distribution between segment center and end, the percent excess is zero; positive values indicate more volcanoes at the segment ends, and negative values indicate more in the segment centers.

To evaluate the statistical significance of the Nex values, the binomial model is used. For n volcanoes along a segment, the probability of observing k or more volcanoes at the segment ends can be expressed as: $p(\geq k, n) = 1-\beta(k-1, n, 0.5)$, where β represents the binomial cumulative distribution function evaluated for k successes out of n total trials, and 0.5 is the probability of any randomly positioned volcano being located near the segment end (e.g., Trauth, 2010). When $p(\geq k, n)$ is small (e.g., < 0.05), significantly

more volcanoes are found near the segment ends. Conversely, if $p(\geq k, n)$ is large (e.g., > 0.95), significantly more volcanoes form at the segment centers. We interpret $0.05<p<0.95$ indicating no significant patterns in volcano formation within a segment. Scaling laws for the size-frequency distribution of monogenetic and polygenetic cones have been applied to many volcanic fields, in both subaerial (e.g., Pérez-López et al., 2011; Howell et al., 2012) and submarine (e.g., Jordan and Menard, 1983; Scheirer and Macdonald, 1995; Smith and Cann, 1990, 1992; Smith and Jordan, 1987, 1988; White et al., 1998) environments. Estimating the characteristic height of a volcano population provides information about the magmatic budget required to produce a group of volcanoes. The size-frequency scaling of volcano populations are typically modeled using a self-similar power law for seamounts greater than 2 km in height (e.g., Wessel, 2001; Wessel and Lyons, 1997) or an exponential model (e.g., Smith and Cann, 1992; Smith and Jordan, 1987, 1988) for heights less than 2 km. Because the volcano heights in this study do not exceed 600 m, we estimate the characteristic height (β-1) of the volcano population following the exponential model described in Jordan and Menard (1983): $N(h)=\nu e^{-h\beta}$, where $N(h)$ is the predicted cumulative number of volcanoes of height greater than or equal to h and ν represents the volcano density. The model parameters are determined using a robust (L1-norm) linear regression of log(N) versus h binned at 10 m intervals. For the regression, the parameter estimates obtained from a bootstrap resampling do not exhibit a normal distribution; consequently, the 95% confidence intervals are determined empirically from the {2.5%, 97.5%} quantile intervals.

4.3 Results

As spreading rate decreases, axial morphology transitions to axial high, crustal thickness increases by 4.5 km (Martinez et al., 2006), a melt lens appears (Jacobs et al., 2007) and lava geochemistry becomes more arc-like approaching the Tofua Arc (Pearce et al., 1995). Concurrently, volcano abundance, volume and the mean distance from the volcano to axial trace decrease s (Figure 4.2). A decrease in mean distance is related to a decrease in spreading rate; the mean age of volcanoes does not systematically vary (Figure 4.2c). Maximum and median height are variable but not systematically related to spreading rate (Figure 4.2b). Along the axial valley segment in the N-ELSC where spreading is the fastest (96 mm/yr), more volcanoes occur near the segment ends (19°40'S to 20°10'S), but volume and maximum height are highest near the center of this segment. South of the northern-most segment to the southern end of the C-ELSC, abundance, volume and median height are relatively uniform as axial morphology transitions to a rifted axial high and spreading rate decreases from 76 mm/yr to 61 mm/yr (Figure 4.2). Between 21°15' and 21°40'S, a single volcano is present at the offset between the C-ELSC and VFR, marking the transition from rifted axial high to axial high morphology. Volcano abundance on the VFR is low relative to the N-ELSC and C-ELSC (Figure 4.2) and the depth to the axial magma chamber decreases from 2340 mbsf along the northern VFR to 2820 mbsf at the southern end (Jacobs et al., 2007). Volcano total volume and max height along the VFR are lower than the N-ELSC and C-ELSC; however, two large spikes in total volume and height occur at 22°07' and 22°31'S near segment centers produced by grouping overlapping volcanoes into a single base (Figure 4.2).

Aggregating the volcano-normalized position along segment on the basis of axial morphology reveals that volcanoes are clustered at the center of the single rifted axial high segment, but otherwise we find no relationship between volcanoes and distance from segment ends (Figure 4.3). A tendency for volcanoes to form at the center of the single rifted axial high segment may not be representative of volcano distribution along segments with similar morphologies found along other back-arc spreading ridges. Volcanoes do not tend to cluster along segments underlain with a melt lens (Figure 4.4a, C-ELSC and VFR) or with MORB-like lavas (Figure 4.4b, N-ELSC, northern-most C-ELSC segment), but there is a significant clustering at segment center along segments with high viscosity lavas influenced by the Tofua Arc (Figure 4.4c).

The height-frequency distributions for volcanoes along axial valley or axial high segments in the ELSC are not well described by the negative exponential model of Smith and Jordan (1988) because the relatively few volcanoes with heights > 250 m do not follow an exponential distribution (Figure 4.5). The negative exponential model describes the height-frequency distribution of the volcanoes along rifted axial high and transitional segments well.

The characteristic height of volcanoes formed within the ELSC is statistically similar independent of axial morphology (Figure 4.6), and no systematic relationship exists between characteristic height and spreading rate or crustal thickness.

4.4 Discussion

4.4.1 Decreasing volcanic edifice abundance and volume

Results from this study indicate volcano abundance and volume in the ELSC decrease along with spreading rate and increasing crustal thickness, depth to melt lens

and lava viscosity. Volcano abundance also was observed to decrease with increasing crustal thickness and magma supply approaching the Galápagos Hotspot along the nearly constant intermediate spreading-rate Galápagos Spreading Centers (GSC) (Behn et al., 2004; White et al., 2008; Howell et al., submitted). Along the GSC, Behn et al. (2004) suggest volcano abundance decreases as the style of volcanism changes from point source to fissure fed in response to an increase in the magma supply. Behn et al.'s (2004) results were corroborated by near-bottom mapping showing a decrease in volcano abundance where an increase in high effusion rate lava morphology was found (White et al., 2008). Near-bottom mapping in the ELSC, however, does not show a methodical transition in lava morphology with proximity to the Tofua Arc (e.g., Martinez et al., 2006), indicating a systematic change in effusion rate does not occur along the ELSC.

Wiedicke and Collier (1993) suggest the style of volcanism along the VFR is controlled by lava viscosity, which is thought to solidify and clog potential fissures so magma reaches the seafloor at localized points. Martinez et al. (2006) observe several small volcanic cones with basal diameters less than a few hundred meters interspersed with few lava flows along the VFR, consistent with Wiedicke and Collier's (1993) expected style of volcanism. Wiedicke and Collier (1993) and Martinez et al. (2006) suggest lava viscosity leads to more point source eruptions; yet, the results shown here indicate seamount abundance decreases as lava viscosity increases.

High-resolution surveys of axial volcanic ridges in the MAR appear to be formed almost entirely of small (< 200 m tall) steep volcanic cones or hummocks in volcanic lineaments (e.g. Smith and Cann, 1990; 1992; Searle et al., 2010). A similar morphology is found along the VFR where many volcanic cones overlap to form a single en echelon

segment of the VFR (Wedicke and Collier, 1993; Martinez et al., 2006; Ferrini et al., 2008). When volcanic cones overlap, their bases become ambiguous and their topographic expression is reduced, leading the MBOA to group many overlapping cones into a single feature (Howell et al., 2012). If the overlapping volcanic cones are aligned, their shape resembles an elongated volcano with a long-to-short axis ratio greater than the threshold allowed within the MBOA (e.g., Bohnenstiehl et al., 2012), eliminating these volcanoes from the database. Considering the near-bottom observations within the VFR of many overlapping volcanic cones (Martinez et al., 2006), it appears a decrease in seamount abundance with an increase in crustal thickness is related to a grouping of multiple volcanoes by the MBOA and this is reflected in the volume plots (IS IT? Fig 2 is harder to read now).

Although the MBOA may group many volcanoes into a single feature, the MBOA is extremely effective at estimating volcanic field statistics (Howell et al., 2012). Along the ELSC, the largest large peaks (>1 km3) in total volume and max height that are not associated with an increase in volcano abundance are found along the VFR (Figure 4.2a), where magma supply is expected to be greatest due to increased melting of water rich magma (Dunn et al., 2013). Martinez et al. (2006) observe that many of the small volcanic cones along the VFR contain summit pit craters, and multibeam bathymetry observations from this study indicate the largest volcanoes contain calderas. White et al. (2008) also observed the largest single volcanic cone along the GSC where magma supply was large. Combined with lava morphology observations, volume calculations and magma supply rates of Axial Volcano from the Juan de Fuca Ridge, White et al. (2008) suggested that caldera formation is part of a normal progression as

magma supply rate increases at a constant spreading rate. Results from the ELSC are consistent with White et al.'s (2008) model.

4.4.2 No tendency for volcanoes to form at segment end

Jacobs et al. (2007) image an isolated axial magma chamber near the center of the northernmost N-ELSC segment, and a nearly continuous magma lens beneath the C-ELSC and VFR. Dunn et al. (2013) observe a low velocity zone, which they describe as a crustal magmatic system, underlying the entire ELSC. The crustal magmatic system deepens and widens along the N-ELSC in response to either higher spreading rate, less efficient hydrothermal removal of heat related to a drop in the upper crustal porosity, or the interplay between short-term melt supply and hydrothermal heat removal (Dunn et al., 2013). Multichannel seismic (Collier and Sinha, 1990; Jacobs et al., 2007) and tomographic images (Dunn and Martinez, 2011; Dunn et al., 2013) of the ELSC suggest that a continuous magma-rich zone extends beneath all of the ridge offsets except the 8 km overlapping spreading center at 20°10'S. The continuity of crustal magma may explain why volcanoes are not related to segmentation in the ELSC. Results from the East Pacific Rise indicate overlapping spreading centers coincide with disruptions in the crustal magmatic system, specifically the axial magma chamber associated with a change in the style of volcanism from fissure fed to point source (e.g. White et al., 2002b). Other studies, however, show that low velocity anomalies continue through the overlapping spreading centers (Bazin et al., 2003; Toomey et al., 2007).

Along the ELSC, volcanoes form at the center of the single rifted axial high segment (Figure 4.3c) and along segments influenced by the volcanic arc magmas (Figure 4.4c), but volcano total volume and height are focused at the center of the

northernmost N-ELSC segment. Along the GSC, White et al. (2008) observe that the largest of the volcanoes in the low abundance region proximal to the Galápagos Hotspot occur at the summits of broad rises in the axial depth profile along the ridge. The broad rises typically occur near the centers of segments, indicating large volcanoes in the magma rich portion of the GSC tend to form at the centers of segments. White et al. (2008) suggest each segment on the GSC axial rise acts like a central volcano, with rifts on either side that erupt a considerable fraction of the total volcanic budget as axial volcanic ridges or low-relief flows. As the magma supply rate exceeds the magma supply predicted by spreading rate, the central volcano becomes larger and eventually forms a caldera.

The central volcano model is consistent with volcano volume and height distribution along the northernmost N-ELSC segment. Along the segments influenced by the Tofua Arc, however, seamount abundance is elevated instead of volume. A detailed analysis of seafloor morphology would likely reveal a central volcano at the center of the segments where fissures have coalesced into localized points in response to the magma viscosity; although, a study of that magnitude or scope has not yet been published.

4.5 Conclusions

Volcano abundance and volume in the ELSC decrease along with spreading rate and increasing crustal thickness, depth to axial magma chamber and lava viscosity. These results are similar to observations along the intermediate spreading-rate Galápagos Spreading Centers, although lava viscosity does not vary and the axial magma chamber shallows approaching the Galápagos Hotspot. A decrease in seamount abundance is attributed to overlapping volcanic cones that are not easily isolated, and support use of

total volume in future work. The largest seamounts along the ELSC are found in the Valu Fa Ridge, where lava viscosity and crustal thicknesses are elevated. The characteristic height of volcanoes along the ELSC is not systematically related to crustal thickness or spreading rate.

Volcano distribution does not systematically relate to spreading rate, axial morphology or melt lens. This is likely related to the continuous crustal magma system present beneath all segment offsets except the largest overlapping spreading center. The single rifted axial high segment and segments with arc-like lavas tend to form volcanoes at the center, potentially related to a segment-central vent that has focused into multiple point sources. For MORB-like segments, volcano volume and height are focused at the center of the segment, consistent with a segment behaving as a central volcano with flanking rifts.

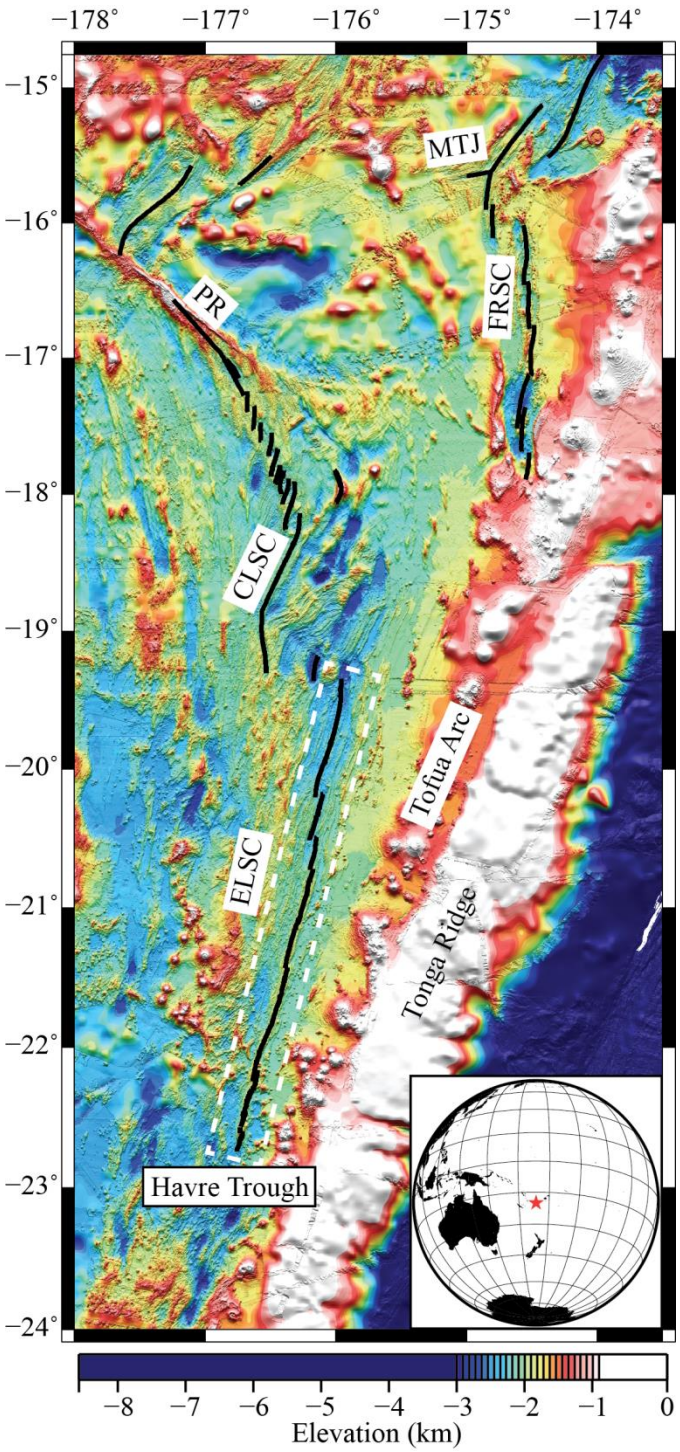

Figure 4.1. Regional bathymetric map of the Lau Basin. Black line indicates the spreading axis (Martinez et al., 2006), white box indicates the region shown in Figure 4.2. PR, Peggy Ridge; CLSC, Central Lau Spreading Centers; ELSC, Eastern Lau Spreading Centers; FRSC, Fonualie Rift and Spreading Center; MTJ, Mangatolu Triple Junction.

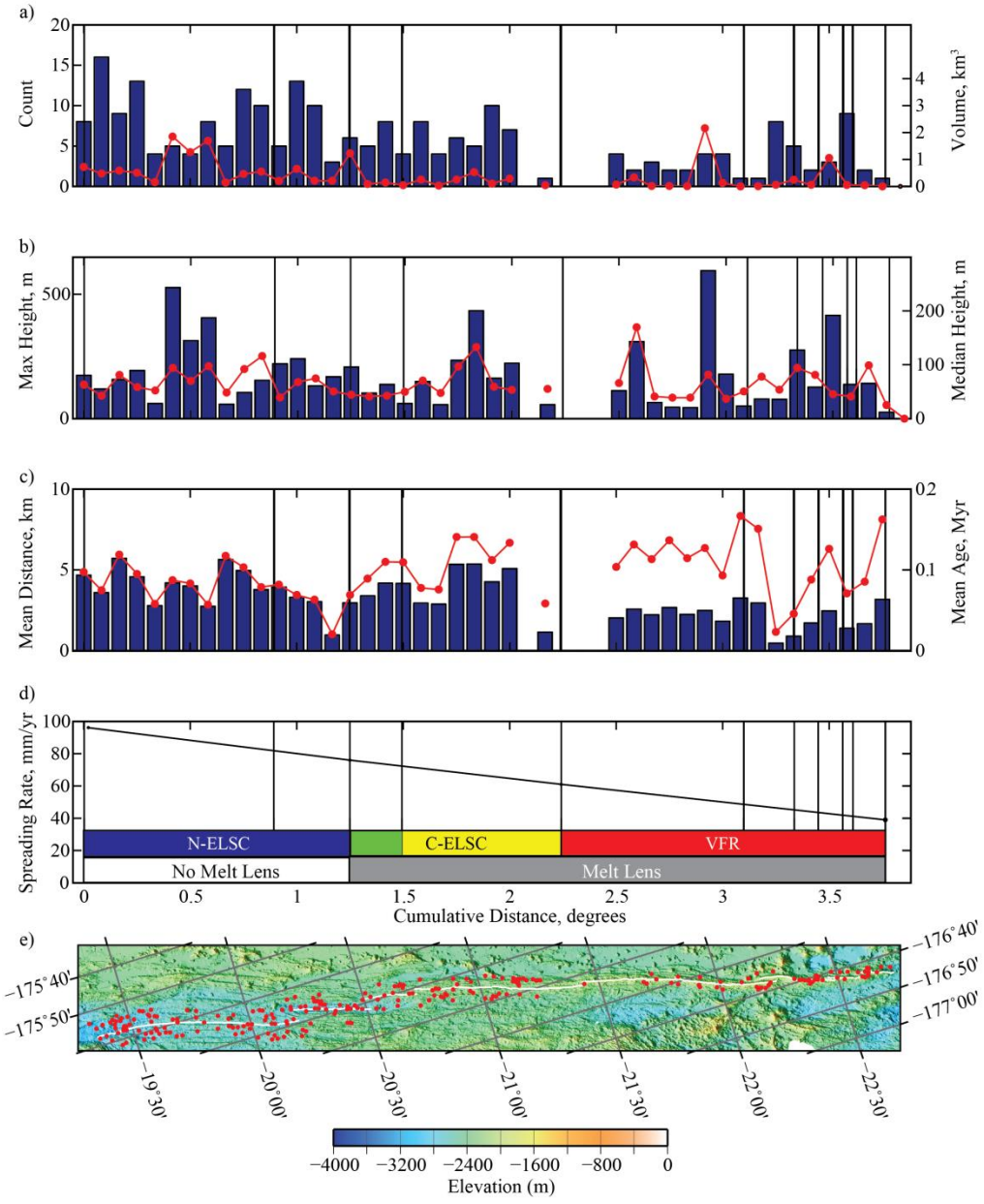

Figure 4.2. a) abundance (blue bars), total volume (red line) and segment offsets (black lines), b) max height (blue bars), median height (red line) and offsets in segmentation; c) mean distance (blue bars), mean age (red line) and offsets in segmentation (black lines), d) spreading rate (black line), axial morphology (blue, shallow axial valley; green, transitional; yellow, rifted axial high; red, axial high), melt lens and segment offsets (black lines), and d) bathymetry of the ELSC with seamount centroids (red dots) and axial trace (white line).

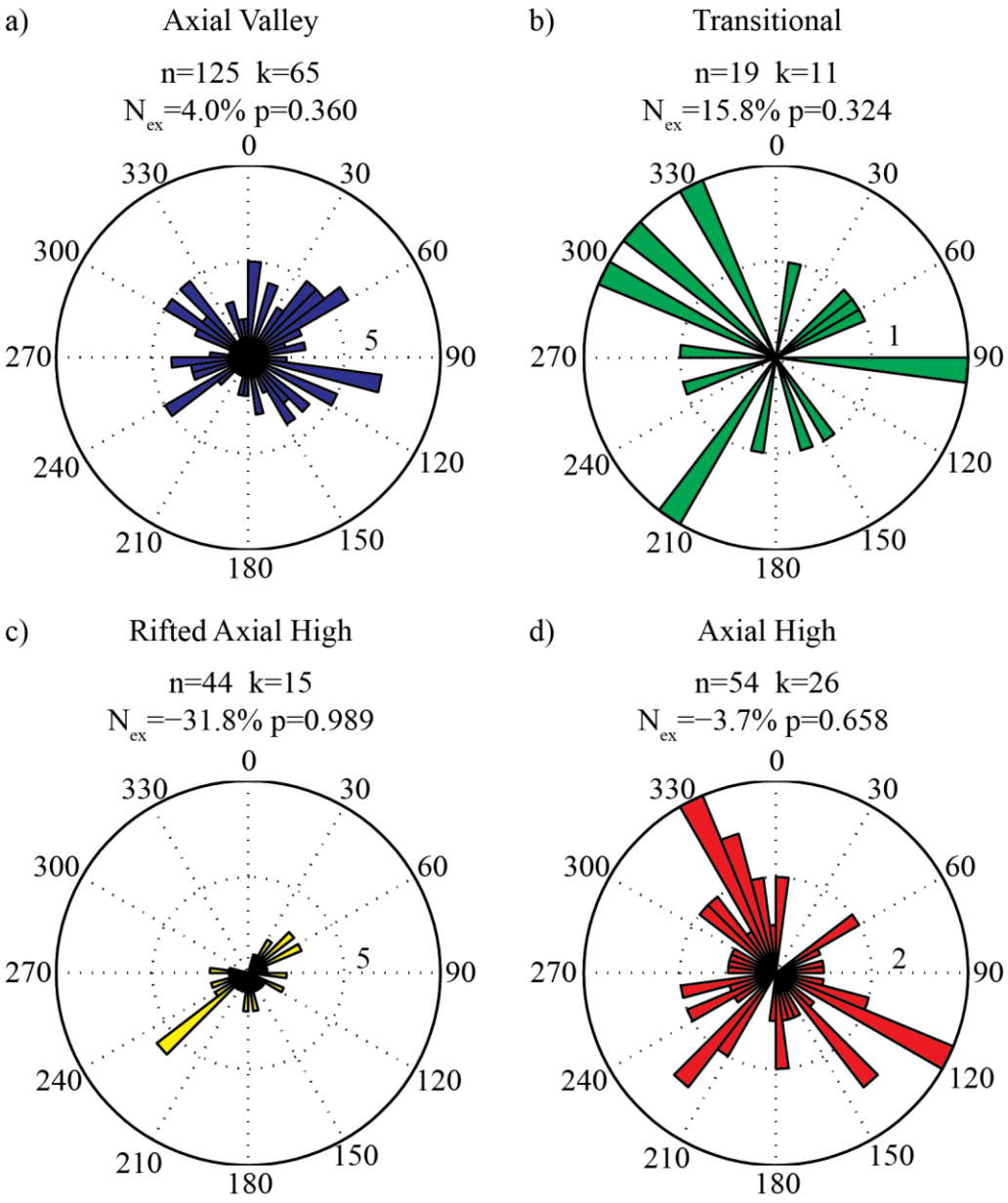

Figure 4.3. Rose diagrams for a) axial valley, b) transitional, c) rifted axial high and d) axial high morphologies along the ELSC. n indicates the number of volcanoes, k is the number of volcanoes formed at segment end, N_{ex} is the percent excess, and p is the probability that >k volcanoes form at segment end by chance. See text for explanation of variables.

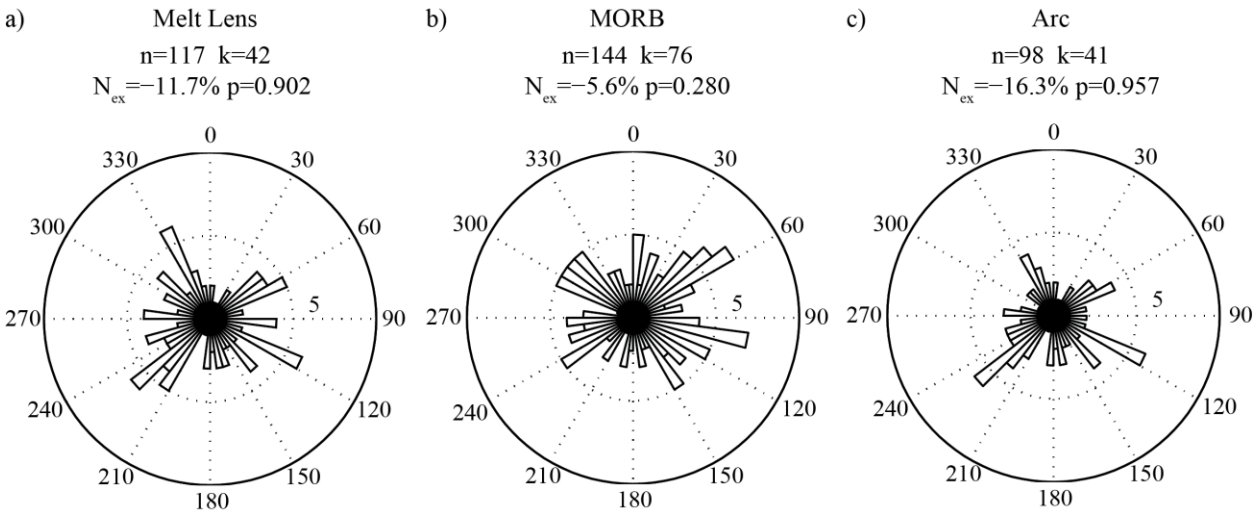

Figure 4.4. Rose diagrams for segments a) underlain by a melt lens, b) with MORB-like lavas (N-ELSC and northernmost C-ELSC segment) and c) with arc-like lavas (southernmost C-ELSC and VFR). See Figure 4.3 for description of variables.

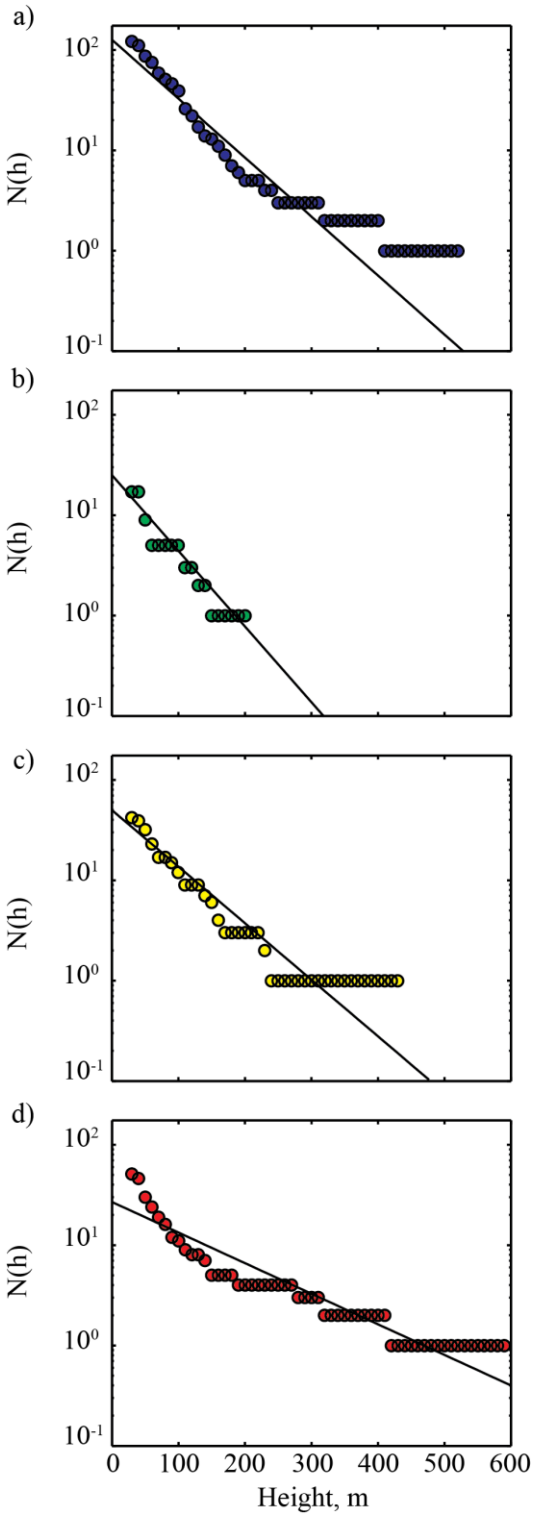

Figure 4.5. The height-frequency distribution of volcanoes in the ELSC. Blue circles, axial valley; green circles, transitional; yellow circles, rifted axial high; red circles, axial high morphology. Solid black line indicates the linear regression.

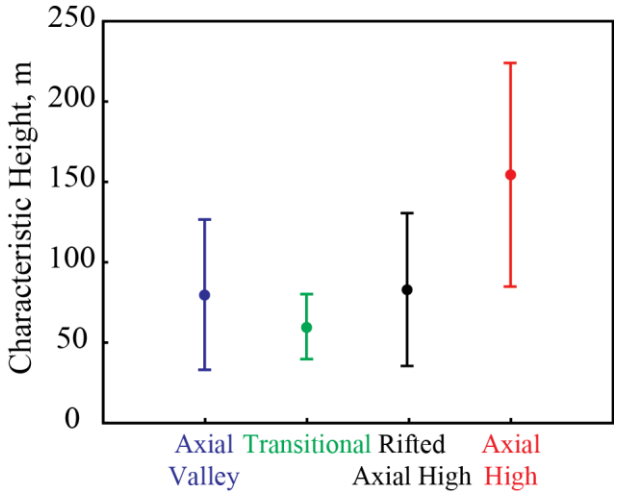

Figure 4.6. The characteristic height with standard error determined empirically from the {2.5%, 97.5%} quantile intervals for each morphology in the ELSC.

CHAPTER 5: 3D GEODYNAMIC MODELS OF THE STRESS FIELD AT OBLIQUE-SPREADING MID-OCEAN RIDGES

The controls on the formation and evolution of faulting patterns at obliquely spreading mid-ocean ridges (MOR) are a function of lithospheric strength and geometry (Van Wijk and Blackman, 2007), spreading rate (Tuckwell et al., 1996), and the amount of obliquity between the stretching direction and a perpendicular to the deformation zone (Dauteuil and Brun; Fournier and Petit, 2007). Oblique extension occurs in both continental and oceanic environments, and along MOR systems with various spreading rates (van Wijk and Blackman, 2007). Earthquake focal mechanisms along ultra-slow to slow spreading ridges describe faults that slip at an angle roughly halfway between the stretching direction and perpendicular to the strike of the deformation zone (Fournier and Petit, 2007), or at an angle parallel to the stretching direction (Dauteuil and Brun, 1993).

Previous studies (e.g. Withjack and Jamison, 1986; Tuckwell et al., 1996; Fournier and Petit, 2007) have demonstrated that three structural directions are linked in the process of oblique rifting: the strike of the deformation zone (α), the stretching direction between the two plates (β), and the trend of the least (or greatest) principal strain (ε_3, Figure 5.1). This study investigates the orientation of the least principal strain and the total strain across an idealized 3-D MOR for obliquities of 15, 30 and 45° and near-axis lithosphere slopes of 30, 40 and 50°, relative to an orthogonal spreading MOR. We attempt to explain the orientation in principal strain observed by Fournier and Petit

(2007) from earthquake focal mechanisms and the direction of fault slip observed by Dauteuil and Brun (1993) along the Mohns Ridge.

5.1 Model Setup

When the stretching direction, β, is perpendicular to the strike of the deformation zone, α, deformation is accommodated by dip-slip normal faults parallel to the deformation zone. When β is oblique to α, deformation is accommodated by a combination of normal faults parallel and oblique to the rift trend (Fournier and Petit, 2007; Dauteuil and Brun, 1993). In an oblique setting, the least compressive principal strain (ε_3) has been observed to trend parallel to the stretching direction (Dauteuil and Brun, 1993) or halfway between the stretching direction and a perpendicular to the deformation zone (Fournier and Petit, 2007).

5.1.1 Model Geometry

To calculate the 3-D strain along an idealized MOR, we use the finite element modeling software COMSOL 4.2a for a linearly elastic rheology most similar to gabbro (Table 5.2). To derive a baseline pattern of strain for an orthogonal spreading geometry, we model deformation within a 100 x 100 x 30 km domain with a lithospheric slope (φ) of 40° (Figure 5.2). In this geometry, we assume a 15-km thick lithosphere at the axis, which thickens to 30 km over a distance of 18 km off-axis, creating a 36 km wide "notch" for a lithosphere slope of 40°. This region of thickening lithosphere simulates the thermal structure of a mid-ocean ridge axis where the isotherms deepen off-axis. Similar lithospheric geometries have been used by Behn and Ito (2008) and Ito and Behn (2008) for 2-D modeling.

Increasing the obliquity (θ) between the strike of the deformation zone (α) and a perpendicular to the stretching direction (β+90°) is achieved by rotating α counterclockwise by the angle θ. In these cases, the model domain changes to 100 x 100/cos(θ) x 30 km, as shown in Figure 5.2. Changing the lithospheric slope to 30° or 50° creates maximum deformation zone widths parallel to the stretching direction of 52 km and 25 km, respectively.

5.1.2 Boundary Conditions

For all model geometries, spreading is simulated in a single step by horizontally stretching the side boundaries by 125 m in opposing X-directions (Figure 5.2, 250 m total displacement). Because the model rheology is homogeneous and purely elastic, the increment of spreading does not affect the principal strain directions, only their magnitudes. Boundaries parallel to β allow material to move in the x and z directions, but not in the y direction (Figure 5.2). The top and base of the model are stress free.

5.1.3 Strain Calculations

Total strain is calculated along a 2-D plane located at z=7 km depth and along a profile perpendicular to the stretching direction and centered at x=50*tan(θ) (the axis), y=0 km and z=7 km, using the following equation:

$$\sqrt{(1/2) \times (\varepsilon_{xx}^2 + \varepsilon_{yy}^2 + \varepsilon_{zz}^2 + \varepsilon_{xy}^2 + \varepsilon_{xz}^2 + \varepsilon_{yz}^2)}$$

where ε is the strain tensor signified by its components. The azimuth of the least compressive principal strain, ε_3, is calculated by obtaining the angle between the principal directions of the least compressive strain in the x and y directions relative to the stretching direction, α.

5.2 Results

Total strain for an orthogonal MOR with φ=40° along a 2-D plane at z=7 km is greatest within the deformation zone (Figure 5.3a). Along the profile shown in Figure 5.3a, the orientation of ε_3 is aligned with the stretching direction and perpendicular to the strike of the deformation zone (Figure 5.3b). Total strain along the profile reaches a maximum 8 km from the axis before dropping to a local minimum on top of the spreading axis (Figure 5.3c).

Similar to the 2-D plane a z=7km for the orthogonal MOR, a 15° oblique MOR has greatest strains inside and parallel to the deformation zone (Figure 5.4a). The concentration of strain at the obtuse corners of Figure 4.4a is an artifact of the model domain. The orientation of ε_3 along a profile perpendicular to α centered at x=13, y=0 and z=7 km is approximately halfway between β and α+90° outside of the deformation zone (Figure 5.4b). Within the deformation zone, ε_3 rotates clockwise toward the stretching direction. Total strain along the profile shows the same pattern as Figure 5.3c, with greatest total strains 6.75 km from the axis before dropping to a local minimum on axis (Figure 5.4c).

Increasing the obliquity to 30° and widening the deformation zone to 52 km by decreasing the lithospheric slope to φ=30° parallel to the stretching direction shows a similar pattern of total strain in the 2-D cut plane at z=7 km (Figure 5.5a). The azimuth of ε_3 outside of the deformation zone along a profile perpendicular to α centered at x=29, y=0 and z=7 km is approximately halfway between β and α+90°. Similar to θ=15° and φ=40°, ε_3 rotates slightly (~5°) toward the stretching direction inside the deformation zone where total strain reaches a local minimum (Figure 5.5b, c). The maximum total strain occurs 6.25 km from the axis, despite a wider deformation zone.

Keeping the obliquity equal to 30° but changing the lithosphere slope to 40° (36 km wide notch parallel to the stretching direction) results in similar trends as Figure 5.5, with greatest total strains occurring inside the deformation zone and an ε_3 orientation halfway between β and α+90° outside the deformation zone (Figure 5.6a, b). The total strain profile reaches a maximum 6.5 km from the spreading axis and a local minimum on axis (Figure 5.6c).

Increasing the lithospheric slope to φ=50° and keeping θ=30° changes the width of the notch to 25 km parallel to the stretching direction and shows greatest total strains inside the deformation zone along a 2-D plane (Figure 5.6a). The orientation of ε_3 is approximately halfway between β and α+90° outside of the deformation zone and approaching β inside the deformation zone (Figure 5.6b). Despite a narrower deformation zone, the maximum total strain also is located 6.5 km from the spreading axis, similar to φ=40°, but the maximum total strain for φ=50° is greater (Figure 5.6c).

Increasing the obliquity to 45° and decreasing the lithospheric slope to 40° shows greatest strains at the obtuse corners of the 2-D plane, which are artifacts of the model geometry (Figure 5.8a). These edge effects are observed the perpendicular profile centered at the axis (x=50 km) where the strain orientation increases at the ends. Similar to previous results, total strain is elevated within and parallel to the deformation zone. The orientation of ε_3 is halfway between β and α+90° outside the deformation zone, and rotates clockwise at the spreading axis approaching β (Figure 5.8b). The range in total strain along the profile is greatest for θ=45° and the maximum in total strain is located 4.5 km off-axis (Figure 5.8c).

5.3 Discussion

Earthquake focal mechanisms along ultra-slow to slow spreading ridges describe primarily normal faults that slip at an angle roughly halfway between the stretching direction and perpendicular to the strike of the deformation zone (Fournier and Petit, 2007), or at an angle parallel to the stretching direction (Dauteuil and Brun, 1993; Dauteuil and Brun, 1996). Results from this study agree with those from Fournier and Petit (2007); the orientation of ε_3 outside of the deformation zone is approximately halfway between the stretching direction and a perpendicular to the strike of the deformation zone. However, inside the deformation zone, the least compressive principal strain (ε_3) is rotated closer to the stretching direction (β), indicating a preference for faults to slip closer to parallel to the stretching direction within the deformation zone.

Figure 4.9a shows the difference in the orientation of ε_3 on-axis and 25% of the profile length away from the axis for all model geometries. The difference between the least principal strain on- and off-axis increases with increasing obliquity and to a lesser degree with lithosphere slope. This implies that variations in lithospheric slope do not significantly influence the orientation of least compressive strain.

The maximum total strain observed along a line perpendicular to the deformation zone and centered at $x=50*\tan(\theta)$, $y=0$ and $z=7$ km occurs within 4.5-8 km from the spreading axis (Figure 5.9b). With increasing degrees of obliquity, distance from the axis to the maximum strain decreases, and the maximum total strain increases. A decrease in distance to the spreading axis with an increase in obliquity is likely a result of a smaller notch width covered by the profile taken perpendicular to the deformation zone. The notch width is constant for each lithosphere slope parallel to the stretching direction, but for profiles perpendicular to the deformation zone, the notch area covered by the profile

decreases with increasing obliquity. While this is a geometric constraint inherent to the model geometry, it might have parallels to oblique spreading MORs, such as: how quickly does the thermal structure of the MOR adapt to a change in stretching direction?

The location of maximum strain is where faults are most likely to develop; at 7 km depth faults should form 4.5-8 km from the axis. At the surface, faults should form an even greater distance from the axis, approaching the width of the notch (either parallel or oblique to the stretching direction) and defining a maximum deformation zone.

However, none of our oblique spreading simulations produce least compressive principal strains that are completely parallel to the stretching direction, as observed by Dauteuil and Brun (1993, 1996). This is likely related to our assumptions of the lithosphere behaving as a purely elastic layer; moving to a depth dependent rheology that allows the lithosphere to reach a yield point and behave plastically could influence the stress, and therefore strain, regime near the axis. These models also fail to account for magma intrusion at the axis, which has been shown by Behn and Ito (2008) to alter the axial lithospheric structure and the local stress field, potentially allowing the least principal strain orientation to align parallel to the stretching direction.

Nevertheless, results from this study indicate that greater degrees of obliquity between the deformation zone and the stretching direction dramatically influence the orientation of new faults within the deformation zone, and the direction of slip along pre-existing faults outside of the deformation zone. Furthermore, while the thermal structure does influence the direction of fault slip and the location of new faults, it is not as influential as the amount of obliquity.

5.4 Conclusions

The results presented here show an agreement with observations of fault slip patterns from earthquake focal mechanisms for the least principal strain outside of the deformation zone. Inside the deformation zone, the orientation of the least principal strain rotates clockwise toward the stretching direction, indicating a preference for faults to slip parallel to the stretching direction when the lithosphere is sufficiently weak, as observed by Dauteuil and Brun (1993, 1996). The distance from the spreading axis to the maximum total strain decreases with increasing obliquity, indicating fault development occurs closer to the spreading axis with increasing degrees of obliquity. Lithosphere slope does influence the orientation of least principal strain and maximum total strain, although at lesser degrees than the amount of obliquity.

Table 5.1. List of symbols used throughout Chapter 5.

α	Strike of the deformation zone
β	Stretching direction
ε_{ij}	Strain tensor
ε_3	Least principal strain
φ	Lithospheric Slope
θ	Obliquity

Table 5.2. Table of constants used to define a gabbroic rheology

.Symbol	Value	Description
ν	0.25	Poisson's Ratio
ρ	2900 kg/m^2	Density
E	30 GPa	Young's Modulus

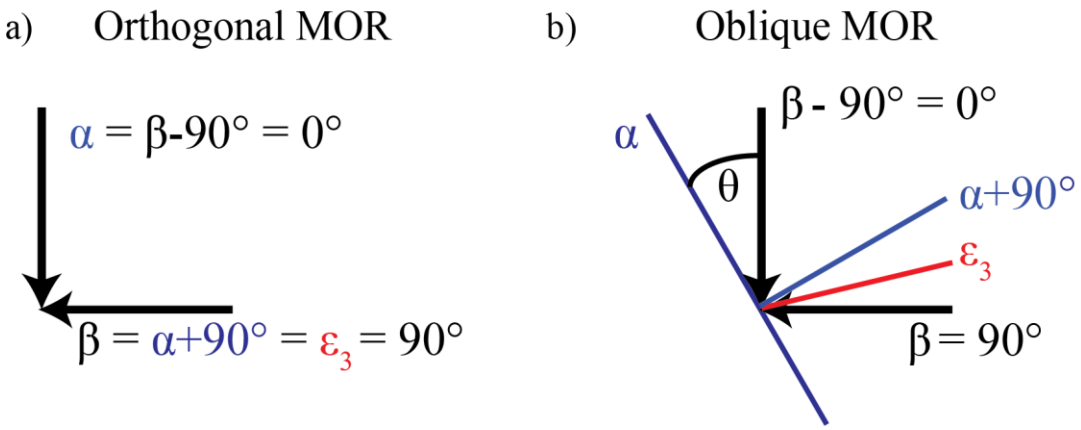

Figure 5.1. Three structural directions associated with a) orthogonal and b) oblique spreading. For an orthogonal MOR, the strike of the deformation zone, α, is perpendicular to the stretching direction, β. The least principal strain, ε_3, is parallel to the stretching direction and perpendicular to the deformation zone. For an oblique MOR, β is oblique to α and ε_3 trends approximately halfway between β and α+90°.

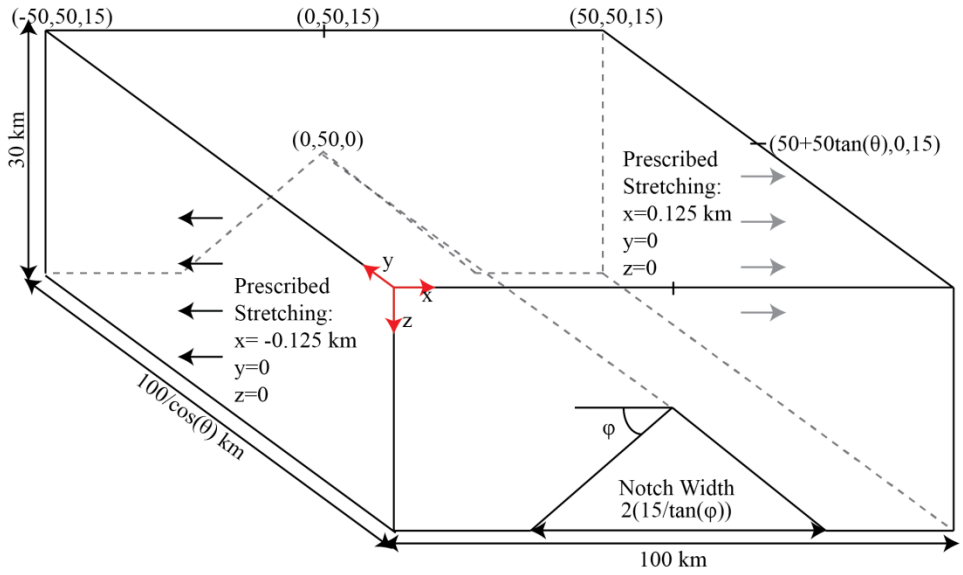

Figure 5.2. Model geometry and boundary conditions used throughout study. A 100 km x 100/cos(θ) km x 30 km rectangular box with a notch of width $2 \times (15/\tan(\varphi))$ for a line perpendicular to the deformation zone is stretched by 125 m on boundaries perpendicular to the stretching direction. Front and back boundaries parallel to the stretching direction allow material to move in the x and z directions, but not in the y. Top and bottom boundaries are free.

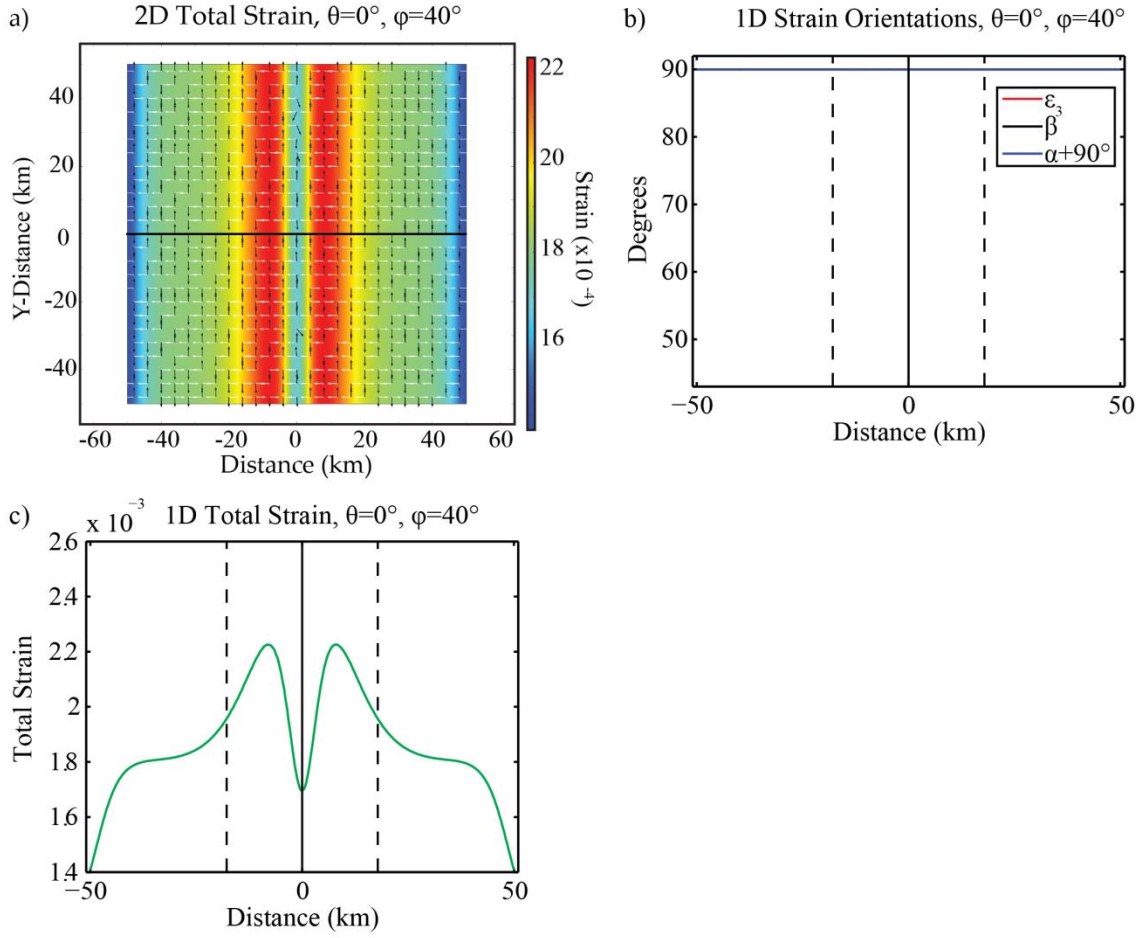

Figure 5.3. Total strain and least principal strain orientation for an orthogonal MOR with a 40° lithosphere. a) Total strain along a plane at z=7 km. Warmer colors indicate areas of greater strain. Black and white arrows denote the direction of most and least principal stresses. Black horizontal line indicates profile shown in b) and c). b) Least principal strain orientation along profile shown in a). Solid black vertical line indicates the location of the spreading axis; dashed black lines indicate the width of the notch. When spreading is orthogonal, the least principal strain (ε_3) is parallel to the stretching direction (β) and perpendicular to the strike of the deformation zone (α). c) Total strain along the profile shown in a). Solid black vertical line indicates the location of the spreading axis; dashed black lines indicate the width of the notch. Total strain is elevated within the deformation zone, but reaches a local minimum at the axis.

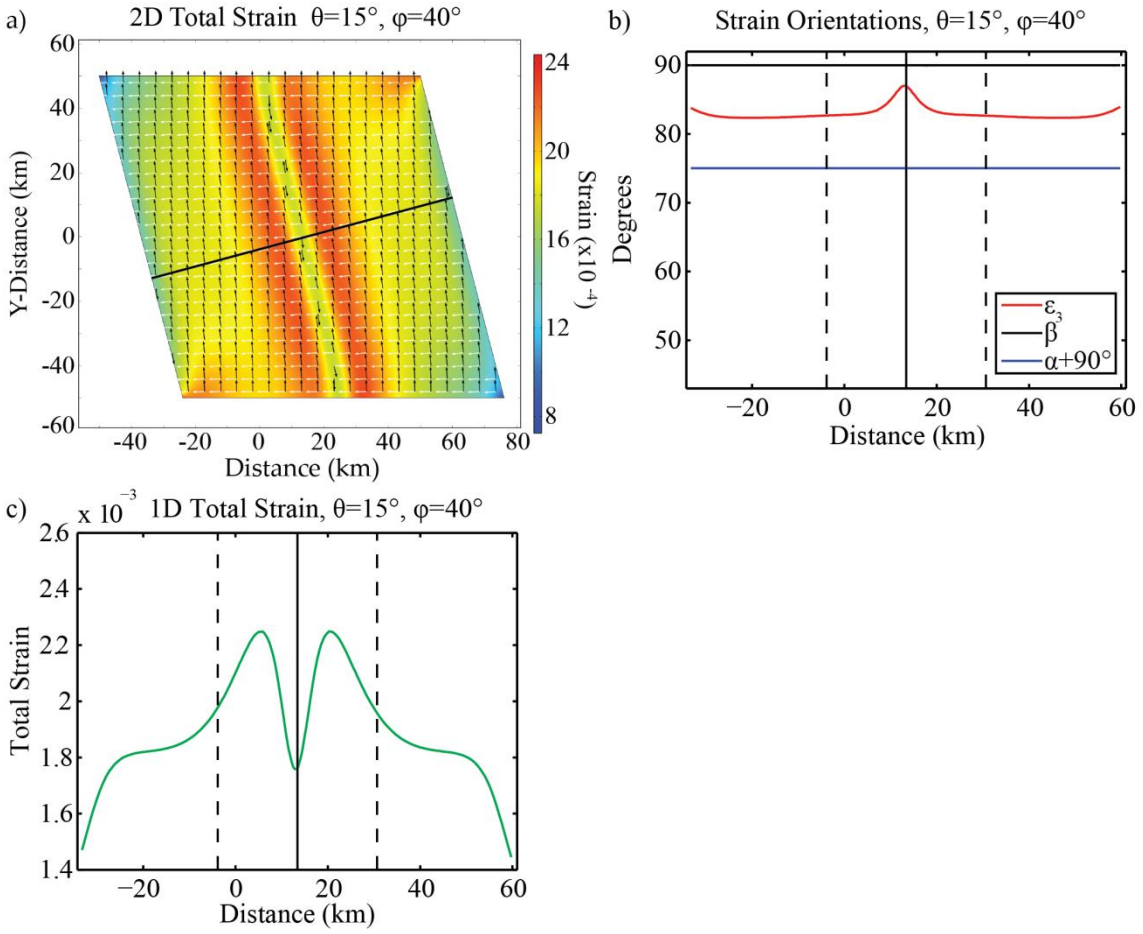

Figure 5.4. Total strain and least principal strain orientation for a 15° oblique MOR with a 40° lithosphere. a) Total strain along a plane at z=7 km. Warmer colors indicate areas of greater strain. Black and white arrows denote the direction of most and least principal stresses. Black horizontal line indicates profile shown in b), and c). b) Least principal strain orientation along profile shown in a). Solid black vertical line indicates the location of the spreading axis; dashed black lines indicate the width of the notch. When spreading is oblique, the least principal strain (ε_3) outside of the deformation zone is approximately halfway between the stretching direction (β) and the perpendicular to the strike of the deformation zone (α). Inside the deformation zone, ε_3 approaches β. c) Total strain along the profile shown in a). Solid black vertical line indicates the location of the spreading axis; dashed black lines indicate the width of the notch. Total strain is elevated within the deformation zone, but reaches a local minimum at the axis.

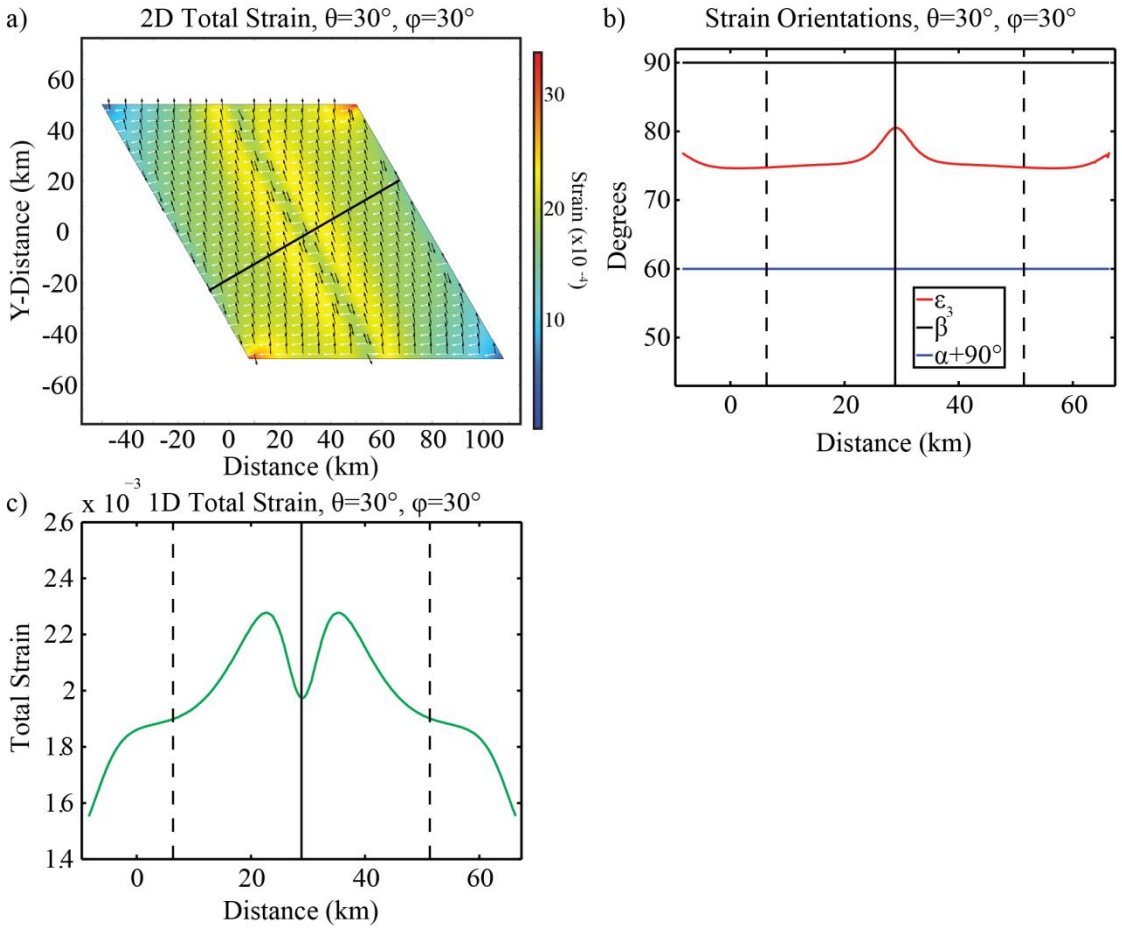

Figure 5.5. Total strain and least principal strain orientation for a 30° oblique MOR with a 30° lithosphere (φ). a) Total strain along a plane at z=7 km. Warmer colors indicate areas of greater strain. Black and white arrows denote the direction of most and least principal stresses. Black horizontal line indicates profile shown in b) and c). b) Least principal strain orientation along profile shown in a). Solid black vertical line indicates the location of the spreading axis; dashed black lines indicate the width of the notch. When spreading is oblique, the least principal strain (ε_3) outside of the deformation zone is approximately halfway between the stretching direction (β) and the perpendicular to the strike of the deformation zone (α). Inside the deformation zone, ε_3 approaches β. c) Total strain along the profile shown in a). Solid black vertical line indicates the location of the spreading axis; dashed black lines indicate the width of the notch. Total strain is elevated within the deformation zone, but reaches a local minimum at the axis.

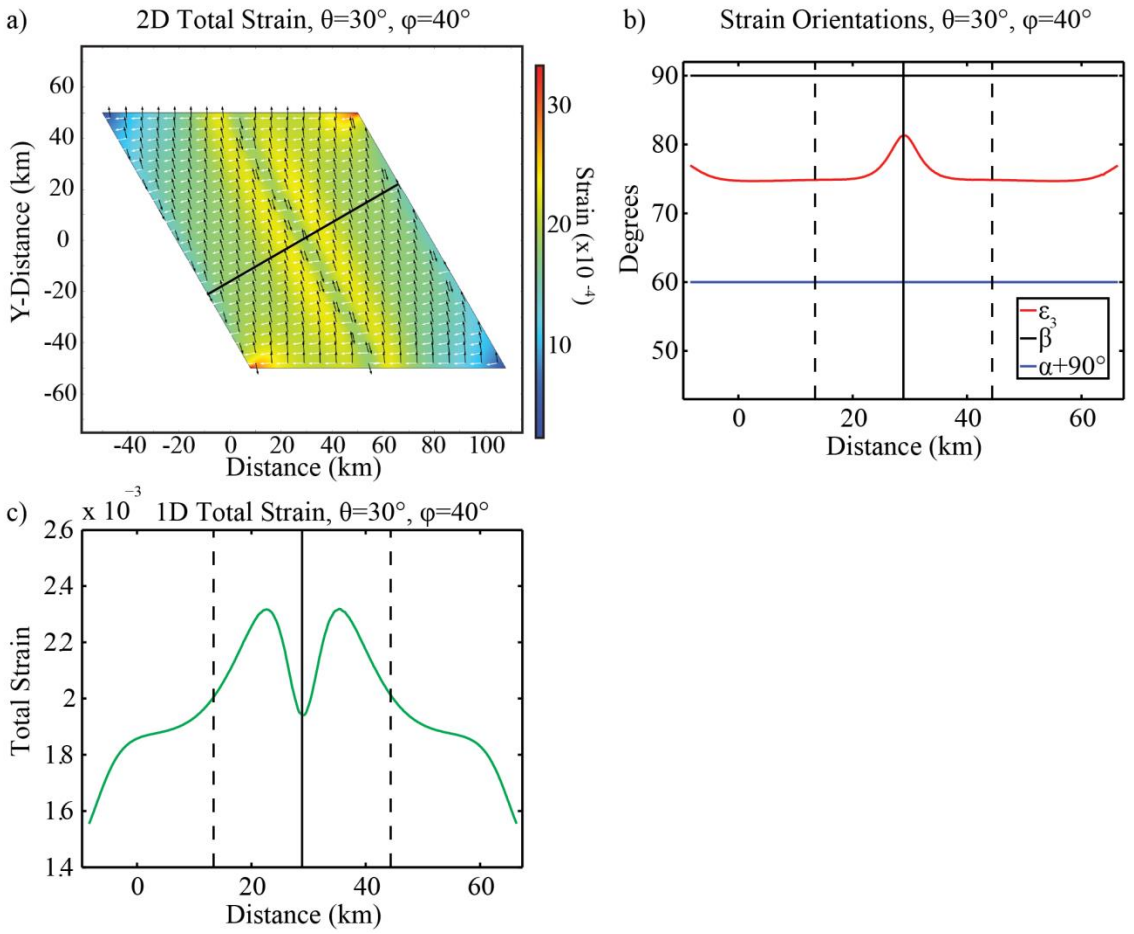

Figure 5.6. Total strain and least principal strain orientation for a 30° oblique MOR with a 40° lithosphere (φ). a) Total strain along a plane at z=7 km. Warmer colors indicate areas of greater strain. Black and white arrows denote the direction of most and least principal stresses. Black horizontal line indicates profile shown in b) and c). b) Least principal strain orientation along profile shown in a). Solid black vertical line indicates the location of the spreading axis; dashed black lines indicate the width of the notch. When spreading is oblique, the least principal strain (ε_3) outside of the deformation zone is approximately halfway between the stretching direction (β) and the perpendicular to the strike of the deformation zone (α). Inside the deformation zone, ε_3 approaches β. c) Total strain along the profile shown in a). Solid black vertical line indicates the location of the spreading axis; dashed black lines indicate the width of the notch. Total strain is elevated within the deformation zone, but reaches a local minimum at the axis.

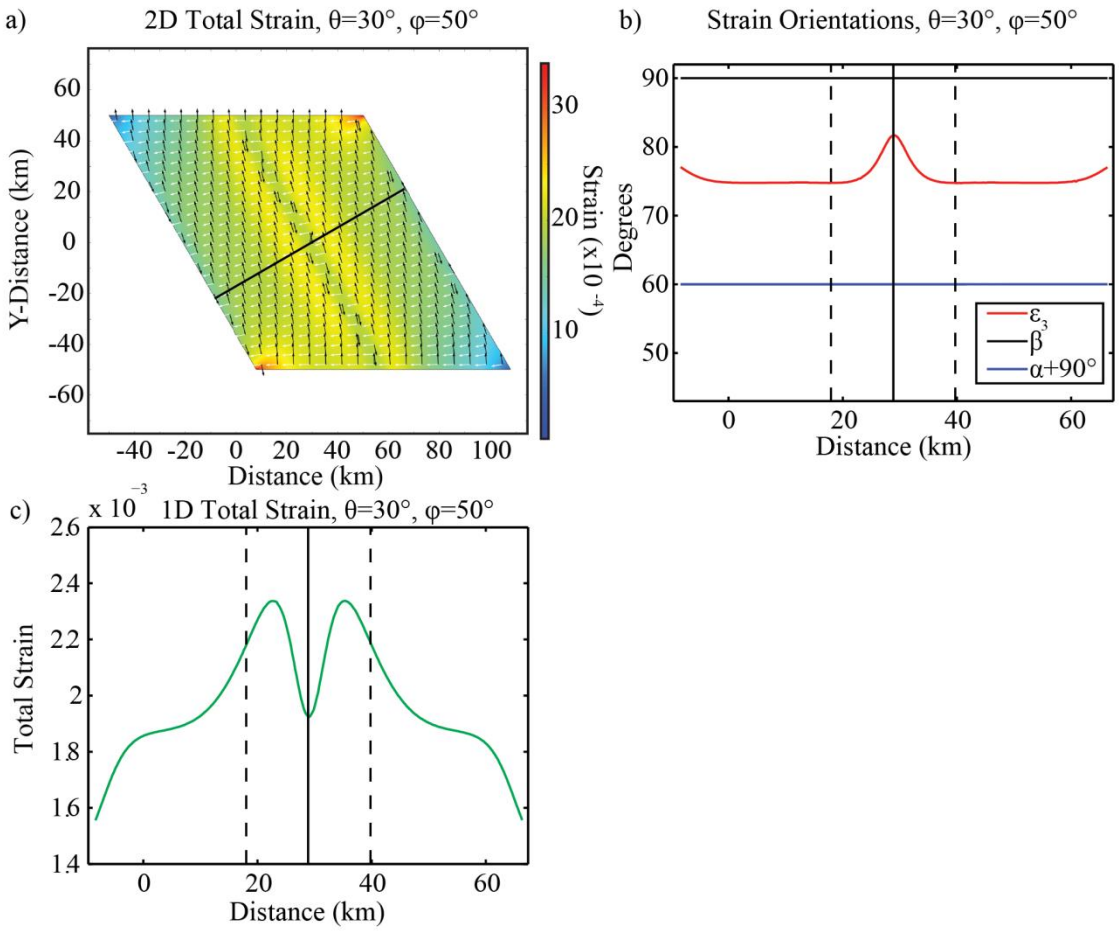

Figure 5.7. Total strain and least principal strain orientation for a 30° oblique MOR with a 50° lithosphere (φ). a) Total strain along a plane at z=7 km. Warmer colors indicate areas of greater strain. Black and white arrows denote the direction of most and least principal stresses. Black horizontal line indicates profile shown in b) and c). b) Least principal strain orientation along profile shown in a). Solid black vertical line indicates the location of the spreading axis; dashed black lines indicate the width of the notch. When spreading is oblique, the least principal strain (ε_3) outside of the deformation zone is approximately halfway between the stretching direction (β) and the perpendicular to the strike of the deformation zone (α). Inside the deformation zone, ε_3 approaches β. c) Total strain along the profile shown in a). Solid black vertical line indicates the location of the spreading axis; dashed black lines indicate the width of the notch. Total strain is elevated within the deformation zone, but reaches a local minimum at the axis.

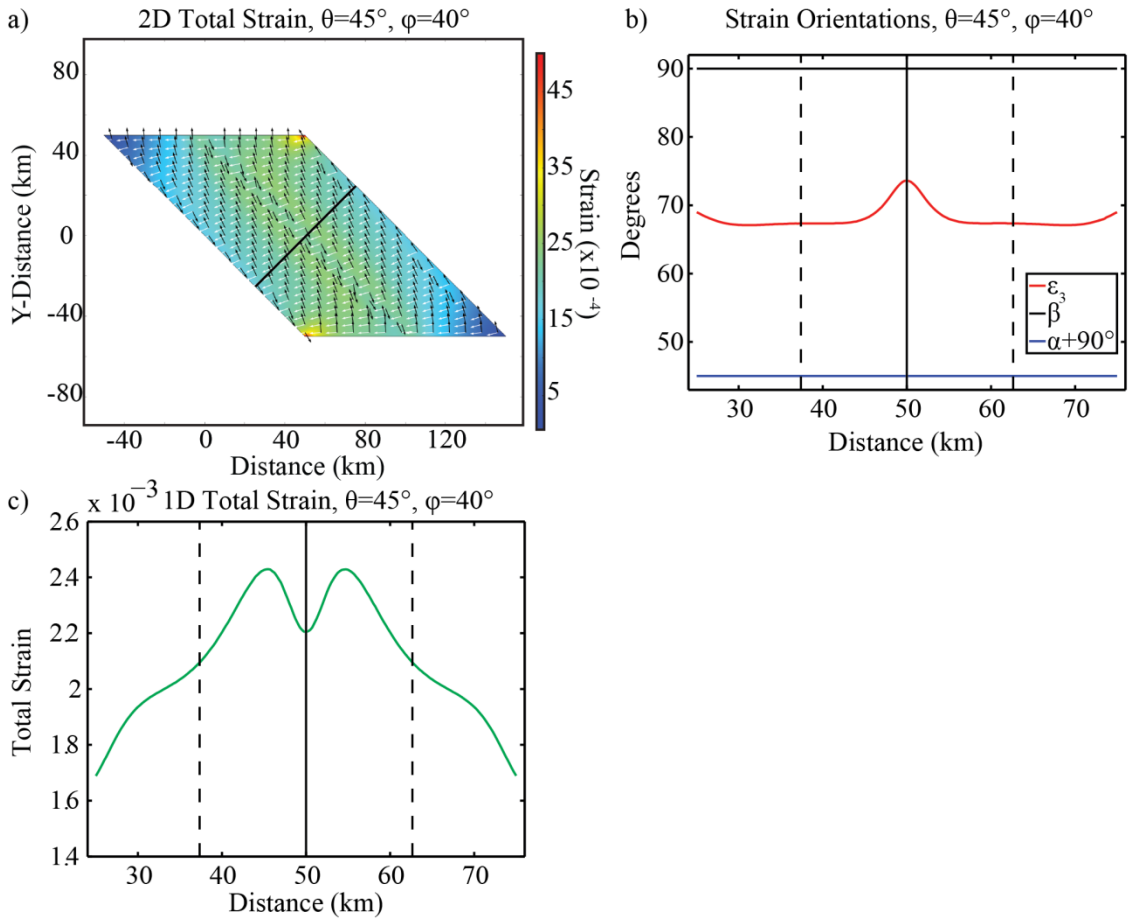

Figure 5.8. Total strain and least principal strain orientation for θ=45° MOR with a 40° lithosphere (φ) . a) Total strain along a plane at z=7 km. Warmer colors indicate areas of greater strain. Black and white arrows denote the direction of most and least principal stresses. Black horizontal line indicates profile shown in b) and c). b) Least principal strain orientation along profile shown in a). Solid black vertical line indicates the location of the spreading axis; dashed black lines indicate the width of the notch. When spreading is oblique, the least principal strain (ε_3) outside of the deformation zone is approximately halfway between the stretching direction (β) and the perpendicular to the strike of the deformation zone (α). Inside the deformation zone, ε_3 approaches β. c) Total strain along the profile shown in a). Solid black vertical line indicates the location of the spreading axis; dashed black lines indicate the width of the notch. Total strain is elevated within the deformation zone, but reaches a local minimum at the axis.

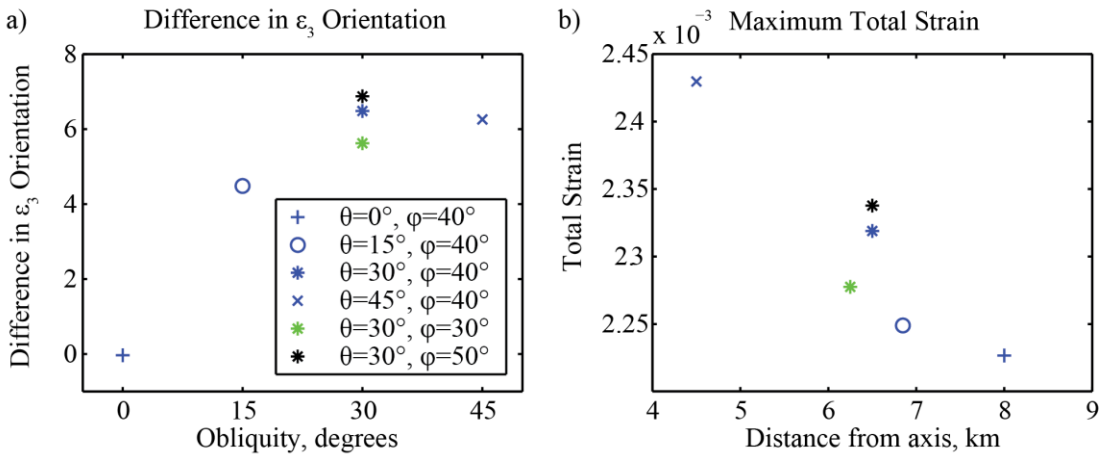

Figure 5.9. a) Difference in the orientation of ε_3 at the spreading axis and 30 km from the spreading axis and b) distance from spreading axis to maximum in total strain. Plusses (+), θ=0°; open circles (o), θ=15°; asterisks (*), θ=30°; exes (x), θ=45°. Green, 30° lithospheric slope; black, 45° lithospheric slope.

CHAPTER 6: CONCLUSIONS

This study attempted to answer three main questions surrounding the generation of oceanic crust at mid-ocean ridges: 1) what is the most efficient and accurate way to identify volcanic edifices from gridded elevation data sets, 2) how does magma supply influence the formation and distribution of seamounts along mid-ocean ridges, and 3) how does the shape of the lithosphere and the amount of obliquity between the spreading and stretching directions along mid-ocean ridges influence the creation of faults within the deformation zone?

1. Chapter 2 describes three separate methods of identifying volcanic edifices: a) manual identification through field geologic mapping, b) identification by using closed-contours, and c) the Modified Basal Outlining Algorithm (MBOA). Chapter 2 shows that the MBOA improves on the accuracy of the closed-contour method by more closely approximating the height, area and volume of volcanoes. Specifically, the MBOA under-predicts height and area by 4% and over-predicts volume by 13%. The closed-contour method, however, under-predicts height, area and volume by 10%, 50% and 45%, respectively. Without petrology, the MBOA will never be as accurate as field geologic mapping; however, it does efficiently delineate volcano outlines and collect morphometric characteristics within a volcanic field.

2. This study established that along intermediate spreading-rate ridges, the abundance and volume of seamounts are related to axial morphology, but their spatial distribution along a segment is not. Axial valley and transitional segments consistently have more volcanoes than axial high or rifted axial high segments, as expected for seamounts that are controlled by magma supply. However, at the Eastern Lau Spreading Centers more volcanoes with larger volumes than elsewhere on the ridge form where magma supply is larger, possibly related to a more andesitic magma in the region of greatest magma supply. Whether seamounts are more abundant at the ends of segments, as expected based on studies at fast-spreading ridges with an axial high morphology, is determined by spreading rate. For ridges spreading faster than 76 mm/yr, such as the Southeast Indian Ridge, seamounts are more abundant at the end of segments independent of axial morphology, melt lens presence, or hotspot influence. For ridges spreading slower than 60 mm/yr, like the Juan de Fuca Ridge and the Galápagos Spreading Centers, seamounts do not prefer to form at segment ends irrespective of axial morphology, melt lens presence or hotspot influence. Along portions of the Juan de Fuca ridge spreading slower than 50 mm/yr, seamounts are more abundant near segment centers.
3. 3-D numerical models of oblique spreading mid-ocean ridges indicate that lithospheric geometry influences the direction of fault slip, but not as much as the amount of obliquity between the stretching direction and perpendicular to the strike of the axis. The thermal structure of the mid-ocean ridge, simulated by the slope of the lithosphere, controls the width of the zone of fault development,

where faults prefer to slip parallel to the stretching direction. Furthermore, fault development occurs closer to the neo-volcanic zone as obliquity increases. Because fault strike and the directions of dike propagation are parallel, these results can be extrapolated to predict the preferential orientation of diking events along oblique mid-ocean ridges.

REFERENCES

Atwater, T. and Mudie, J.D., 1973. Detailed near-bottom geophysical survey of the Gorda Rise. J. Geophys. Res. 78(35), 8,665-8,686, doi:10.1029/JB078i035p08665

Auzende, J.-M., et al., 1990. Active spreading in and hydrothermalism in North Fiji basin (SW Pacific): Results of the Japanese French Cruise Kaiyo 87, Marine Geophysical Researches, 12, 269-283.

Baran, J.M., Cochran, J.R., Carbotte, S.M., Nedimović, M.R., 2005. Variations in upper crustal structure due to variable mantle temperature along the Southeast Indian Ridge. Geochem., Geophys., Geosyst. 6(11), Q11002, doi:10.1029/2005GC000943.

Behn, M.D. and Ito, G., 2008. Magmatic and tectonic extension at mid-ocean ridges: 1. Controls on fault characteristics, Geochemistry, Geophysics, Geosystems, 9(8), Q08O10, doi:10.1029/2008GC001965.

Behn, M., Sinton, J., Detrick, R., 2004. Effect of the Galápagos hotspot on seafloor volcanism along the Galápagos Spreading Center (90.9-97.6° W). Earth and Planetary Science Letters 217(3-4), 331-347. doi:10.1016/S0012-821X(03)00611-3.

Bemis, K., 1995. A morphometric study of volcanoes in Guatemala, Iceland, the Snake River Plain, and the South Pacific. PhD. Thesis, Rutgers University.

Bemis, K., Walker, J., Borgia, A., Turrin, B., Neri, M., Iii, C.S., 2011. The growth and erosion of cinder cones in Guatemala and El Salvador: Models and statistics. Journal of Volcanology and Geothermal Research 201(1-4), 39-52. doi: 10.1016/j.jvolgeores.2010.11.007.

Bishop, M.A., 2007. Point pattern analysis of eruption points for the Mount Gambier volcanic sub-province: a quantitative geographical approach to the understanding of volcano distribution. Area 39(2), 230-241, doi: 10.1111/j.1475-4762.2007.00729.x.

Bohnenstiehl, D., Howell, J., Hey, R., 2008. Distribution of axial lava domes along a superfast overlapping spreading center, 27–32°S on the East Pacific Rise. Geochemistry, Geophsyics, Geosystems 9(12), 1-15. doi: 10.1029/2008GC002158.

Bohnenstiehl, D.R., Howell, J.K., White, S.M., Hey, R.N., 2012. A modified basal outlining algorithm for identifying topographic highs from gridded elevation data, Part 1: Motivation and methods. Computers and Geosciences 49, 308-314. doi:10.1016/j.cageo.2012.04.023.

Botros, M., Johnson, H.P., 1988. Tectonic evolution of the Explorer-Northern Juan de Fuca Region from 8 Ma to the present. J. Geophys. Res. 93(B9), 10,421-10,437, doi: 10.1029/JB093iB09p10421.

Canales, J.P., Dañobeitia, J.J., Detrick, R.S., Hooft, E.E.E., Bartolomé, R., Naar, D.F., 1997. Variations in axial morphology along the Galápagos spreading center and the influence of the Galápagos hotspot. J. Geophys. Res. 102(B12), 27,341-27,354, doi: 10.1029/97JB01633.

Canales, J.P., Ito, G., Detrick, R.S., Sinton, J., 2002. Crustal thickness along the western Galápagos Spreading Center and the compensation of the Galápagos hotspot swell. Earth Planet. Sci. Lett. 203(1), 311-327, doi: 10.1016/S0012-821X(02)00843-9.

Canales, J.P., Detrick, R.S., Carbotte, S.M., Kent, G.M., Diebold, J.B., Harding, A., Babcock, J., Nedimović, van Ark, E., 2005. Upper crustal structure and axial topography at intermediate spreading ridges: Seismic constraints from the southern Juan de Fuca Ridge. J. Geophys. Res. 110 B12104, doi: 10.1029/2005JB003630.

Carbotte, S.M., Small, C., Donnelly, K., 2004. The influence of ridge migration on the magmatic segmentation of mid-ocean ridges. Nature 429, 743-746, doi: 10.1038/nature02652.

Carbotte, S.M., Nedimović, M.R., Canales, J.P., Kent, G.M., Harding, A.J., Marjanović, M., 2008. Variable crustal structure along the Juan de Fuca Ridge: Influence of on-axis hotspots and absolute plate motions. Geochem., Geophys., Geosyst. 9(8), Q08001, doi:10.1029/2007GC001922.

Chadwick, W.W., Embley, R.W., Shank, T.M., 1998. The 1996 Gorda Ridge eruption: geologic mapping, sidescan sonar, and SeaBeam comparison results. Deep Sea Research Part II: Topical Studies in Oceanography 45(12), 2,547-2,569, doi: 10.1016/S0967-0645(98)00083-6.

Chadwick, J., Perfit, M., Ridley, I., Jonasson, I., Kamenov, G., Chadwick, W., Embley, R., le Roux, P., Smith, M., 2005. Magmatic effects of the Cobb hot spot on the Juan de Fuca Ridge. J. Geophys. Res. 110, B03101, doi: 10.1029/2003JB002767.

Christie, D.M., Werner, R., Hauff, F., Hoernle, K., Hanan, B.B., 2005. Morphological and geochemical variations along the eastern Galápagos Spreading Center. Geochem., Geophys., Geosyst. 6, Q01006, doi:10.1029/2004GC000714.

Cochran, E.S., Vidale, J.E., Tanaka, S., 2004. Earth Tides Can Trigger Shallow Thrust Fault Earthquakes. Science 306(5699), 1164-1166, doi: 10.1126/science.1103961.

Cochran, J., 2008. Seamount volcanism along the Gakkel Ridge, Arctic Ocean. Geophysical Journal International 174, 1153-1173. doi: 10.1111/j.1365-246X.2008.03860.x.

Cochran, J.R., Sempéré, J.-C., 1997. The Southeast Indian Ridge between 88°E and 118°E: Gravity anomalies and crustal accretion at intermediate spreading rates. J. Geophys. Res. 102(B7), 15,463-15,487.

Collier, J.S. and Sinha, M.C., 1992. Seismic mapping of a magma chamber beneath the Valu Fa Ridge, Lau Basin. J. Geophys. Res. 97(B10), 14031-14053, doi: 10.1029/91JB02751.

Condit, C.D., 1984. The geology of the western part of the Springerville volcanic field, east-central Arizona. Ph.D. Dissertation. Albuquerque, University of New Mexico, 453.

Condit, C.D., 1991. Lithologic map of the western part of the Springerville volcanic field, east-central Arizona. U.S.G.S. Miscellaneous Investigation Map Series I-1993, p. 2 sheets.

Condit, C., 2010. Dynamic Digital Map of the Springerville Volcanic Field and the DDM-Template: An example of an open-source tool to distribute maps, data, articles, and multi-media materials. Geosphere 6(4), 430-443. doi: 10.1130/GES00531.1.

Condit, C., Connor, C., 1996. Recurrence rates of volcanism in basaltic volcanic fields: An example from the Springerville volcanic field, Arizona. Geological Society of America Bulletin 108(10), 1225.

Condit, C., Crumpler, L., Aubele, J., Elston, W., 1989. Patterns of volcanism along the southern margin of the Colorado Plateau: The Springerville field. Journal of Geophysical Research 94(B6), 7975-7986.

Condit, C.D., Crumpler, L.S., Aubele, J.C., 1999. Lithologic, Age-Group, Magneto-Polarity and Geochemical Maps of the Springerville Volcanic Field, East-Central Arizona. U.S.G.S. Miscellaneous Investigation Map Series, I-2431.

Condit, C.D., Shafiqullah, M., 1985. K-Ar ages of late Cenozoic rocks of the western part of the Springerville volcanic field, east-central Arizona. Isochron/West 44, 3-5.

Connor, C., Condit, C., Crumpler, L., Aubele, J., 1992. Evidence of regional structural controls on vent distribution: Springerville Volcanic Field, Arizona. Journal of Geophysical Research 97(B9), 12349.

Cooper, J.L., Aronson, J.L., Condit, C.D., Hart, W.K., 1990. New K-Ar ages of lavas from the Colorado Plateau-Basin and Range transition zone, east-central Arizona. Isochron/West 55, 28-31.

Crumpler, L.S., Aubele, J.C., Condit, C.D., 1989. Influence of Quaternary tectonic deformation on volcanism in the Springervill volcanic field, Colorado Plateau, USA. New Mexico Bureau of Mines and Mineral Resources Bulletin 131, 64.

Crumpler, L.S., Aubele, J.C., Condit, C.D., 1994. Volcanoes and neotectonic characteristics of the Springerville volcanic field, Arizona. Mogollon slope: Socorro, New Mexico Geological Society Guidebook.

Cushman, B., Sinton, J., Ito, G., Dixon, J.E., 2004. Glass compositions, plume-ridge interaction, and hydrous melting along the Galápagos Spreading Center, 90.5°W to 98°W. Geochem., Geophys., Geosyst. 5(8), Q08E17, doi:10.1029/2004GC000709.

Dauteuil, O. and J.-P. Brun, 1993. Oblique rifting in a slow-spreading ridge, Nature, 361, 145-148.

Dauteuil, O. and J.-P. Brun, 1996. Deformation Partitioning in a slow spreading ridge undergoing oblique extension: Mohns Ridge, Norwegian Sea, Tectonics, 15(4) 870-884.

DeMets, C., Gordon, R.G., Argus, D.F., Stein, S., 1990. Current Plate Motions. Geophysical Journal International 101(2), 425-478.

Dennis, K.J., McClinton, J.T., White, S.M., Hoernle, K., Mittelstaedt, E.L. and Harpp, K., 2012. Bathymetry of the Galápagos Spreading Center from a synthesis of 25 years of ship-based multibeam sonar data, Abstract OS51E-1930 presented at 2012 Fall Meeting, AGU, San Francisco, Calif., 3-7 Dec.

Deschamps, A., Tivey, M., Embley, R.W., Chadwick, W.W., 2007. Quantative study of the deformation at Southern Explorer Ridge using high-resolution bathymetric data. Earth Planet. Sci. Lett. 259(1-2), 1-17, doi: 10.1016/j.epsl.2007.04.007.

Detrick, R.S., Sinton, J.M., Ito, G., Canales, J.P., Behn., M., Blacic, T., Cushman, B., Dixon, J.E., Graham, D.W., Mahoney, J.J., 2002. Correlated geophysical, geochemical, and volcancological manifestations of plume-ridge interaction along the Galápagos Spreading Center. Geochem., Geophys., Geosyst. 3(10), 8501, doi:10.1029/2002GC000350.

Dunn, R.A., Martinez, F., and Conder, J.A., 2013. Crustal construction and magma chamber properties along the Eastern Lau Spreading Center. Earth Planet. Sci. Lett. 371-372, 112-124, doi: 10.1016/j.epsl.2013.04.008.

EEZ-SCAN 84 Scientific Staff, 1985. GLORIA II Sonograph Mosaic of the Western U.S. Exclusive Economic Zone. EOS, Trans. Amer. Geophys. Union 66, 553–555.

EEZ-SCAN 84 Scientific Staff, 1986, Atlas of the Exclusive Economic Zone, Western Conterminous United States, U.S. Geological Survey Misc. Investigations Series I-1792, 152 pp.

Embley, R.W., Chadwick, W.W., Perfit, M.R., Smith, M.C., Delaney, J.R., 2000. Recent eruptions on the CoAxial segment of the Juan de Fuca Ridge: Implications for mid-ocean ridge accretion processes. J. Geophys. Res. 105(B7), 16,501–16,525, doi:10.1029/2000JB900030.

Favalli, M., Karátson, D., Mazzarini, F., Pareschi, M.T., Boschi, E., 2009. Morphometry of scoria cones located on a volcano flank: A case study from Mt. Etna (Italy), based on high-resolution LiDAR data. Journal of Volcanology and Geothermal Research 186(3-4), 320-330. doi: 10.1016/j.jvolgeores.2009.07.011.

Fedotov, S.A., 1981. Magma rates in feeding conduits of different volcanic centers. Journal of Volcanology and Geothermal Research 9, 379-394.

Ferrini, V.L., Tivey, M.K., Carbotte, S.M., Martinez, F., Roman, C., 2008. Variable morphologic expression of volcanic, tectonic, and hydrothermal processes at six hydrothermal vent fields in the Lau back-arc basin. Geochem. Geophys. Geosyst. 9(7), Q07022, doi: 10.1029/2008GC002047.

Fink, J.H. and Griffiths, R.W., 1992. A laboratory analog study of the surface morphology of lava flows extruded from point and line sources. J. of Volcanology and Geothermal Res. 54(1-2), 19-32, doi: 10.1016/0377-0273(92)90112-Q.

Fornaciai, A., Favalli, M., Karátson, D., Tarquini, S., Boschi, E., 2012. Morphometry of scoria cones, and their relation to geodynamic setting: A DEM-based analysis. Journal of Volcanology and Geothermal Research 217-218, p.56-72. doi: 10.1016/j.jvolgeores.2011.12.012.

Frenzel, G., Mühe, R., Stoffers, P. 1990. Petrology of the volcanic rocks from the Lau Basin, southwest Pacific. Geol. Jahrb., D 92, 395-479.

Fournier, Marc, Carole Petit, 2007. Oblique rifting at oceanic ridges: Relationship between spreading and stretching directions from earthquake focal mechanisms. Journal of Structural Geology, 29, 201-208. doi: 10.1016/j.jsg.2006.07.017.

Gesch, D.B., 2007. The National Elevation Dataset, in: Maune, D. (Ed.), Digital Elevation Model Technologies and Applications: The DEM Users Manual, 2nd ed. American Society for Photogrammetry and Remote Sensing, Bethesda, Maryland, pp. 99-118.

Gesch, D.B., Oimoen, M., Greenlee, S., Nelson, C., Steuck, M., Tyler, D., 2002. The National Elevation Dataset. Photogrammetric Engineering and Remote Sensing 68(1), 5-11.

Graham, D.W., Johnson, K.T.M., Douglas Priebe, L., Lupton, J.E., 1999. Hotspot-ridge interaction along the Southeast Indian Ridge near Amsterdam and St. Paul islands: helium isotope evidence. Earth Planet. Sci. Lett. 167(3-4), 297-310.

Gregg, T.K.P. and Fink, J.H., 1995. Quantification of submarine lava-flow morphology through analog experiments. Geology 23(1), 73-76.

Griffiths, R.W. and Fink, J.H., 1992. Solidification and morphology of submarine lavas: A dependence on extrusion rate. J. Geophys. Res. 97(B13), 19729-19737, doi: 10.1029/92JB01594.

Grosse, P., van Wyk de Vries, B., Euillades, P.A., Kervyn, M., Petrinovic, I.A., 2012. Systematic morphometric characterization of volcanic edifices using digital elevation models. Geomorphology 136(1), 114-131. doi: 10.1016/j.geomorph.2011.06.001.

Gudmundsson, A., 1987. Geometry, formation and development of tectonic features on the Reykjanes Peninsula, southwest Iceland, Tectonophysics, 139, 295-308.

Hawkins, J.W., 1995. The Geology of the Lau Basin. In: Taylor, B. (Ed.), Backarc Basins: Tectonics and Magmatism. Plenum Press, New York, pp. 63-138.

Hawkins, J.W. and Melchior, J.T., 1985. Petrology of Mariana Trough and Lau Basin basalts. J. Geophys. Res. 90(B13), 11431-11468, doi:10.1029/JB090iB13p11431.

Hey, R.N., Kleinrock, M.C., Miller, S.P., Atwater, T.M., Searle, R.C., 1986. Sea Beam/Deep-Tow Investigation of an active oceanic propagating rift system, Galapagos 95.5°W. J. Geophys. Res. 91(B3), 3,369-3,393, doi: 10.1029/JB091iB03p03369.

Hey, R.N., Sinton, J.M., Kleinrock, M.C., Yonover, R.N., Macdonald, K.C., Miller, S.P., Searle, R.C., Christie, D.M., Atwater, T.M., Sleep, N.H., Johnson, H.P., Neal, C.A., 1992. ALVIN Investigation of an Active Propagating Rift System, Galapagos 95.5°W. Marine Geophysical Researches 14(3), 207-226.

Hillier, J., 2008. Seamount detection and isolation with a modified wavelet transform. Basin Research 20(4), 555-573. doi: 10.1111/j.1365-2117.2008.00382.x.

Holden, J.F., Baker, E.T., Embley, R.W., Hammond, S.R., Shank, T.M., Walker, S.L., White, S.M., Galrex 2011 Team, 2011. GALREX 2011: Initial Results of the 2011 NOAA Ocean Exploration Cruise to the Galápagos Rift Using Interactive Telepresence Technology, Abstract OS22A-06 presented at 2011 Fall Meeting, AGU, San Francisco, Calif., 5-9 Dec.

Hooft, E.E.E. and Detrick, R.S., 1995. Relationship between axial morphology, crustal thickness, and mantle temperature along the Juan de Fuca and Gorda Ridges. J. Geophys. Res. 100(B11), 22,499-22,508, doi: 10.1029/95JB02502.

Hooft, E.E.E., Detrick, R.S., Kent, G.M., 1997. Seismic structure and indicators of magma budget along the Southern East Pacific Rise. J. Geophys. Res. 102(B12), 27,319-27,340, doi: 1029/97JB02349.

Hooper, Donald M., Sheridan, Michael F., 1998. Computer-simulation models of scoria cone degradation. Journal of Volcanology and Geothermal Research 83, 241-267.

Howell, J.K., White, S.M., Bohnenstiehl, D.R., 2012. A modified basal outlining algorithm for identifying topographic highs from gridded elevation data, Part 2: Application to Springerville Volcanic Field. Computers and Geosciences 49, 315-322. doi:10.1016/j.cageo.2012.04.024.

Howell, J.K., White, S.M., Bohnenstiehl, D.R., Seamount Abundance, volume and spatial distribution along three hotspot-influenced intermediate spreading-rate ridges, submitted to Journal of Volcanology and Geothermal Research April 2013.

Ito, G. and Behn, M.D.. 2008. Magmatic and tectonic extension at mid-ocean ridges: 2. Origin of axial morphology, Geochemistry, Geophysics, Geosystems, 9(9), Q09O12, doi:10.1029/2008GC001970.

Jacobs, A.M., Harding, A.J., Kent, G.M., 2007. Axial crustal structure of the Lau back-arc basin from velocity modeling of multichannel seismic data. Earth Planet. Sci. Lett. 259(3-4), 239-255, doi: 10.1016/j.epsl.2007.04.021.

Jordan, T., Menard, H., 1983. Density and size distribution of seamounts in the eastern Pacific inferred from wide-beam sounding data. Journal of Geophysical Research 88(B12), 10,508-510,518.

Karig, D.E., 1970. Ridges and basins of the Tonga-Kermadec Island Arc System. J. Geophys. Res. 75(2), 239-254, doi:10.1029/JB075i002p00239.

Katz, R.F., Spiegelman, M., Carbotte, S.M., 2004. Ridge migration, asthenospheric flow and the origin of magmatic segmentation in the global mid-ocean ridge system, Geophys Res Lett 31(15), L15605, doi:10.1029/2004GL020388.

Kleinrock, M.C. and Hey, R.N., 1989a. Detailed tectonics near the tip of the Galapagos 95.5°W propagator: How the lithosphere tears and a spreading axis develops. J. Geophys. Res. 94(B10), 13,801-13,838, doi: 10.1029/JB094iB10p13801.

Kleinrock, M.C. and Hey, R.N., 1989b. Migrating transform zone and lithospheric transfer at the Galapagos 95.5°W propagator, J. Geophys. Res. 94(B10), 13,859-13,878, doi: 10.1029/JB094iB10p13859.

Kleinrock, M.C., Searle, R.C., Hey, R.N., 1989. Tectonics of the failing spreading system associated with the 95.5°W Galapagos propagator. J. Geophys. Res. 94(B10), 13,839-13,857, doi: 10.1029/JB094iB10p13839.

Kim, S., Wessel, P., 2008. Directional median filtering for regional-residual separation of bathymetry. Geochemistry Geophysics Geosystems 9(3), Q03005. doi:10.1029/2007GC001850.

Ma, Y. and Cochran, J.R., 1996. Transitions in axial morphology along the Southeast Indian Ridge. J. Geophys. Res. 101(B7), 15,849-15,866.

Macdonald, K.C., 1982. Mid-Ocean Ridges: Fine Scale Tectonic, Volcanic and Hydrothermal Processes Within the Plate Boundary Zone. Annual Review of Earth and Planetary Sciences 10,155-190, doi: 10.1146/annurev.ea.10.050182.001103.

Macdonald, K.C., 1986. The crest of the Mid-Atlantic Ridge: Model for crustal generation processes and tectonics, The Geology of North America, volume M, The Western North Atlantic Region, ed. P.R. Vogt and B.E. Tucholke, 51-68, Geological Society of America, Boulder, CO.

Macdonald, K.C., Scheirer, D.S., Carbotte, S.M., 1991. Mid-Ocean Ridges: Discontinuities, Segments and Giant Cracks. Science 253, 986-994.

Martinez, F., and Taylor, B., 2002. Mantle wedge control on back-arc crustal accretion. Nature 416, 417-420, doi: 10.1038/416417a.

Martinez, F., Taylor, B., Baker, E.T., Resing, J.A., Walker, S.L., 2006. Opposing trends in crustal thickness and spreading rate along the back-arc Eastern Lau Spreading Center: Implications for controls on ridge morphology, faulting, and hydrothermal activity. Earth Planet. Sci. Lett. 245(3-4), 655-672, doi:10.1016/j.epsl.2006.03.049.

Michael, P.J., Chase, R.L., Allan, J.F., 1989. Petrologic and geologic variations along the Southern Explorer Ridge, northeast Pacific Ocean. J. Geophys. Res. 94(B10), 13,895-13,918, doi: 10.1029/JB094iB10p13895.

Mittelstaedt, E. and Ito, G., 2005. Plume-ridge interaction, lithospheric stresses, and the origin of near-ridge volcanic lineaments. Geochem., Geophys.s, Geosyst. 6(6), Q06002, doi:10.1029/2004GC000860.

Mittelstaedt, E., Soule, S., Harrp, K., Fornair, D., McKee, C., Tivey, M., Geist, D., Kurz, M.D., Sinton, C., Mello, C., 2012. Multiple expressions of plume-ridge interaction in the Galápagos: Volcanic lineaments and ridge jumps. Geochem., Geophys., Geosyst. 13(5), Q05018, doi:10.1029/2012GC004093.

Parson, L.M., Pearce, J.A., Murton, B.J., Hodkinson, R.A., 1990. Role of ridge jumps and ridge propagation in the tectonic evolution of the Lau back-arc basin, southwest Pacific. Geology 18(5), 470-473.

Pearce, J.A., Ernewein, M., Bloomer, S.H., Parson, L.M., Murton, B.J. and Johnson, L.E., 1995. Geochemistry of Lau Basin volcanic rocks: influence of ridge segmentation and arc proximity. In: Smellie, J.L. (Ed.), Volcanism Associated With Extension at Consuming Plate Margins. Special Publication, vol. 81. Geological Society, London, pp. 53-75.

Pérez-López, R., Legrand, D., Garduño-Monroy, V.H., Rodríguez-Pascua, M.A., Giner-Robles, J.L., 2011. Scaling laws of the size-distribution of monogenetic volcanoes within the Michoacán-Guanajuato Volcanic Field (Mexico). Journal of Volcanology and Geothermal Research 201(1-4), 65-72. doi: 10.1016/j.jvolgeores.2010.09.006.

Perfit, M.R. and Chadwick, W.W., 1998. Magmatism at mid-ocean ridges: Constraints from volcanological and geochemical investigations. Geophysical Monograph-American Geophysical Union 106, 59-116.

Phipps Morgan, J. and Chen, J., 1993. Dependence of ridge-axis morphology on magma supply and spreading rate. Nature 364, 706-708, doi:10.1038/364706a0.

Phipps Morgan, Jason, E.M. Parmentier, J. Lin, 1987. Mechanisms for the Origin of Mid-Ocean Ridge Axial Topography: Implications for the Thermal and Mechanical Structure of Accreting Plate Boundaries. Journal of Geophysical Research 92(B12), 12,823-12,836.

Riddihough, R., 1984. Recent movements of the Juan de Fuca Plate System. J. Geophys. Res. 89(B8), 6,980-6,994, doi: 10.1029/JB089iB08p06980.

Rodriguez-Gonzalez, A., Fernandez-Turiel, J.L., Perez-Torrado, F.J., Paris, R., Gimeno, D., Carracedo, J.C., Aulinas, M., 2012. Factors controlling the morphology of monogenetic basaltic volcanoes: The Holocene volcanism of Gran Canaria (Canary Islands, Spain). Geomorphology 136(1), 31-44. doi: 10.1016/j.geomorph.2011.08.023.

Rona, P.A., Meis, P.J., Beaverson, C.A., Embley, R.W., Fox, C.G., 1992. Geologic setting of hydrothermal activity at the northern Gorda Ridge. Mar. Geol. 106(3-4), 189-201, doi:10.1016/0025-3227(92)90129-6.

Royer, J.-Y. and Schlich, R., 1988. Southeast Indian Ridge Between the Rodriguez Triple Junction and the Amsterdam Saint-Paul Islands: Detailed Kinematics for the Past 20 m.y. J. Geophys. Res. 93(B11), 13,524-13,550, doi:10.1029/JB093iB11p13524.

Rubin, A., 1993. Tensile fracture of rock at high confining pressure: Implications for dike propagation. J. Geophys. Res. 98(B9), 15919-15935, doi: 10.1029/93JB01391.

Ryan, W.B.F., Carbotte, S.M., Coplan, J.O., O'Hara, S., Melkonian, A., Arko, R., Weissel, R.A., Ferrini, V., Goodwillie, A., Nitsche, F., Bonczkowski, J., Zemsky, R., 2009. Global Multi-Resolution Topography synthesis. Geochem., Geophys., Geosyst. Q03014, doi:10.1029/2008GC002332

Scheirer, D.S. and Macdonald, K.C., 1995. Near-axis seamounts on the flanks of the East Pacific Rise, 8ºN to 17ºN. Journal of Geophysical Research 100(B2), 2239-2259.

Scheirer, D.S., Baker, E.T., Johnson, K.T.M., 1998. Detection of hydrothermal plumes along the Southeast Indian Ridge near the Amsterdam-St. Paul Plateau. Geophys Res Lett 25(1), 97-100, doi:10.1029/97GL03443

Scheirer, D.S., Forsyth, D.W., Conder, J.A., Eberle, M.A., Hung, S.-H., Johnson, K.T.M., Graham, D.W., 2000. Anomalous seafloor spreading of the Southeast Indian Ridge near the Amsterdam-St. Paul Plateau. J. Geophys. Res. 105(B4), 8,243-8,262, doi:10.1029/1999JB900407.

Schilling, J.-G., Fontignie, D., Blichert-Toft, J., Kingsley, R., Tomza, U., 2003. Pb-Hf-Nd-Sr isotope variations along the Galápagos Spreading Center (101°-83°W): Constraints on the dispersal of the Galápagos mantle plume. Geochem., Geophys., Geosyst. 4(10), 8512, doi: 10.1029/2002GC000495.

Searle, R.C. and A.S. Laughton, 1981. Fine-scale sonar study of tectonics and volcanism on the Reykjanes Ridge, Oceanologica Acta, 4, 5-13.

Searle, R.C., Murton, B.J., Achenbach, K., LeBas, T., Tivey, M., Yeo, I., Cormier, M.H., Carlut, J., Ferreira, P., Mallows, C., Morris, K., Schroth, N., van Calsteren, P., Waters, C., 2010. Structure and development of an axial volcanic ridge: Mid-Atlantic Ridge, 45°N. Earth Planet. Sci. Lett. 299(1-2), 228-241, doi: 10.1016/j.epsl.2010.09.003.

Sempéré, J.-C., Cochran, J.R., SEIR Scientific Team, 1997. The Southeast Indian Ridge between 88°E and 118°E: Variations in crustal accretion at constant spreading rate. J. Geophys. Res. 102(B7), 15,489-15,505, doi:10.1029/97JB00171.

Sinton, J., Detrick, R., Canales, J.P., Ito, G., Behn, M., 2003. Morphology and segmentation of the western Galápagos Spreading Center, 90.5°-98°W: Plume-ridge interaction at an intermediate spreading ridge. Geochem., Geophys., Geosyst. 4(12), 8515, doi:10.1029/2003GC000609.

Small, C. and Sandwell, D.T., 1989. An abrupt change in ridge axis gravity with spreading rate. J. Geophys. Res. 94(B12), 17,383-17,392, doi:10.1029/JB094iB12p17383.

Smith, D., Cann, J., 1990. Hundreds of small volcanoes on the median valley floor of the Mid-Atlantic Ridge at 24–30 N. Nature 348, 152-155.

Smith, D., Cann, J., 1992. The role of seamount volcanism in crustal construction at the Mid-Atlantic Ridge (24–30 N). Journal of Geophysical Research 97(B2), 1645-1658.

Smith, D.K. and Cann, J.R., 1993. Building the crust at the Mid-Atlantic Ridge. Nature 365, 707-715.

Smith, D.K. and Cann, J.R., 1999. Constructing the upper crust of the Mid-Atlantic Ridge: A reinterpretation based on the Puna Ridge, Kilauea Volcano. J. Geophys. Res. 104(B11), 25,379–25,399, doi:10.1029/1999JB900177.

Smith, D.K., Cann, J.R., Dougherty, M.E., Lin, J., Spencer, S., MacLeod, C., Keeton, J., McAllister, E., Brooks, B., Pascoe, R., Robertson, W., 1995. Mid-Atlantic Ridge volcanism from deep-towed side-scan sonar images, 25°-29°N. Journal of Volcanology and Geothermal Research 67, 233-262.

Smith, D. and Jordan, T., 1987. The size distribution of Pacific seamounts. Geophysical Research Letters 14(11), 1119-1122.

Smith, D.K. and Jordan, T., 1988. Seamount Statistics in the Pacific Ocean. Journal of Geophysical Research 93(B4), 2899-2918.

Stroup, D.F., Bohnenstiehl, D.R., Tolstoy, M., Waldhauser, F., Weekly, R.T., 2007. Pulse of the seafloor: Tidal triggering of microearthquakes at 9°50'N East Pacific Rise. Geophys Res Lett 34 L15301, doi: 10.1029/2007GL030088.

Sunkel, G., 1990. Petrology and geochemistry of submarine lavas from the Lau Basin (SW Pacific), Mar. Min. 9, 205-234.

Supak, S., Carbotte, S.M., Macdonald, K.C., 2007. Influence of ridge migration and proximity to hotspots on the morphology of slow- and intermediate-spreading centers. Geochem., Geophys., Geosyst. 8(1), Q01010, doi:10.1029/2006GC001387.

Taylor, B. and Karner, G.D., 1983. On the evolution of marginal basins. Rev. of Geophys. 21(8), 1727-1741, doi:10.1029/RG021i008p01727.

Taylor, B., Zellmer, K., Martinez, F., Goodliffe, A., 1996. Sea-floor spreading in the Lau back-arc basin. Earth Planet. Sci. Lett. 144(1-2), 35-40, doi:10.1016/0012-821X(96)00148-3.

Thouret, J.-C., 1999. Volcanic geomorphology—an overview. Earth-Science Reviews 47, 95-131.

Trauth, M. H., Gebbers, R., & Marwan, N. (2010). MATLAB "Recipes for Earth Sciences". Springer.

van Wijk, J.W., D.K. Blackman, 2007. Development of en echelon magmatic segments along oblique spreading ridges. Geology, 35(7), 599-602. doi: 10.1130/G23294A.1

Wessel, P., 1998. An empirical method for optimal robust regional-residual separation of geophysical data. Mathematical Geology 30(4), 391-408.

Wessel, P., 2001. Global distribution of seamounts inferred from gridded Geosat/ERS-1 altimetry. Journal of Geophysical Research 106(B9), 19431-19441.

Wessel, P., Lyons, S., 1997. Distribution of large Pacific seamounts from Geosat/ERS-1: Implications for the history of intraplate volcanism. Journal of Geophysical Research 102(B10), 22459-22475.

White, S.M., Crisp, J.A., Spera, F.J., 2006. Long-term volumetric eruption rates and magma budgets. Geochemistry, Geophysics, Geosystems 7(3), Q03010. doi: 10.1029/2005GC001002.

White, S.M., Macdonald, K.C., Scheirer, D.S., Cormier, M.H., 1998. Distribution of isolated volcanoes on the flanks of the East Pacific Rise, 15.3ºS-20ºS. Journal of Geophysical Research 103(B12), 30371-30384.

White, S.M., Macdonald, K.C., Haymon, R.M., 2000. Basaltic lava domes, lava lakes, and volcanic segmentation on the southern East Pacific Rise. J. Geophys. Res. 105(B10), 23,519-23,516.

White, S.M., Haymon, R.M., Fornari, D.J., Perfit, M.R., Macdonald, K.C., 2002a. Correlation between volcanic and tectonic segmentation of fast-spreading ridges: Evidence from volcanic structures and lava flow morphology on the East Pacific Rise at 9°-10°N. J. Geophys. Res. 107(B8), 2173, doi:10.1029/2001JB000571.

White, S.M., Macdonald, K.C., Sinton, J.M., 2002b. Volcanic mound fields on the East Pacific Rise, 16°-19°S: Low effusion rate eruptions at overlapping spreading centers for the past 1 Myr. J. Geophys. Res. 107(B10), 2240. doi:10.1029/2001JB000483.

White, S.M., Meyer, J.M., Haymon, R.M., Macdonald, K.C., Baker, E.T., Resing, J.A., 2008. High-resolution surveys along the hot spot-affected Galápagos Spreading Center: 2. Influence of magma supply on volcanic morphology. Geochem., Geophys., Geosyst. 9(9), Q09004, doi: 10.1029/2008GC002036.

Wiedicke, M. and Collier, J., 1993. Morphology of the Valu Fa Spreading Ridge in the southern Lau Basin. J. Geophys. Res. 98(B7), 11769-11782, doi:10.1029/93JB00708.

Wilson, D.S., 1993. Confidence Intervals for motion and deformation of the Juan de Fuca Plate. J. Geophys. Res. 98(B9) 16,053-16,071, doi:10.1029/93JB01227.

Withjack, M.O., Jamison, W.R., 1986. Deformation produced by oblique rifting. Tectonophysics, 126, 99-124.

Wood, C., 1980a. Morphometric analysis of cinder cone degradation. Journal of Volcanology and Geothermal Research 8, 137-160.

Wood, C., 1980b. Morphometric evolution of cinder cones. Journal of Volcanology and Geothermal Research 7, 387-413.